A NOVEL THEORETICAL APPROACH TO MODEL ELECTRONIC EXCITATIONS IN MOLECULAR CRYSTALS

by

Feng Xibo

Submitted in partial fulfillment of the requirements
for the degree of Doctor of Philosophy

at

Dalhousie University
Halifax, Nova Scotia
May 2021

"No son molinos, amigo Sancho, que son gigantes."
("They are not windmills, Sancho my friend, they are giants.")
– Don Quixote to his loyal servant, Sancho, before charging into battle against an array of windmills. (Don Quixote, Miguel de Cervantes)

Table of Contents

List of Tables

List of Figures

List of Abbreviations and Symbols Used

Abbreviation	Description
AA	Adiabatic Approximation
ACQ	Aggregation-Caused Quenching
ACFDT	Adiabatic Connection Fluctuation-Dissipation Theorem
AE	All-Electron
AIE	Aggregation-Induced Emission
AMBER	Assisted Model Building with Energy Refinement
APAP	Acetaminophen
BHandHLYP	Becke (1988) exchange Half-and-Half mixing/LYP correlation functional
BLYP	Becke (1988) exchange/LYP correlation functional
BJ	Becke-Johnson
BR	Becke-Roussel
B3LYP	B88 exchange/LYP correlation hybrid functional with 3 parameters
B86a	Becke's 1986 exchange functional - a
B86b	Becke's 1986 exchange functional - b
B86bPBE	B86b exchange/PBE correlation functional
B88	Becke's 1988 exchange functional
CAM-B3LYP	Handy's Coulomb-Attenuated B3LYP exchange-correlation functional
CASTEP	CAmbridge Serial Total Energy Package
CC	Coupled Cluster
CCDC	Cambridge Crystallographic Data Centre
CHARMM	Chemistry at HARvard Macromolecular Mechanics
CI	Configuration Interaction
CIS	Configuration Interaction Singles
CLA	Classical Lewis Adduct
COD	Crystallography Open Database
CSD	Cambridge Structural Database

Abbreviation	Description
CSP	Crystal Structure Prediction
CT	Charge Transfer
DAN	N,N-dimethyl-4-nitroaniline
DFA	Density-Functional Approximation
DFT	Density-Functional Theory
DHNA	1,8-dihydroxy-2-naphthaldehyde
DMABN	4-dimethylamino-benzonitrile
DPDBF	Diphenyldibenzofulvene
D2	Grimme's Disperison correction model 2
D3	Grimme's Dispersion correction model 3
EDG	Electron-Donating Group
ESIDPT	Excited-State Intramolecular Double Proton Transfer
ESIPT	Excited-State Intramolecular Proton Transfer
EWG	Electron-Withdrawing Group
FCC	Face-Centered Cubic
FLP	Frustrated Lewis Pair
GAFF	Generalized AMBER Force Field
GGA	Generalized-Gradient Approximation
GS	Ground State
G09	Gaussian 09 computational package
HF	Hartree-Fock theory
HK	Hohenberg-Kohn
HOMO	Highest Occupied Molecular Orbital
KS	Kohn-Sham
LC-BLYP	Long-range Corrected BLYP hybrid functional
LDA	Local Density Approximation
LR	Linear Response
LUMO	Lowest Unoccupied Molecular Orbital
LYP	Lee-Yang-Parr Correlation functional
MAE	Mean Absolute Error
MBD	Many-Body Dispersion model

Abbreviation	Description
MECI	Minimum-Energy Conical Intersection
MP	Monkhorst-Pack
MP2	Møller-Plesset second-order perturbation theory
ONIOM	Our own N-layered Integrated molecular Orbital molecular Mechanics
OLED	Organic Light-Emitting Diodes
PAH	Polycyclic Aromatic Hydrocarbons
PAW	Projector Augmented Wave
PBE	Perdew-Burke-Ernzerhof exchange-correlation functional
PDA	2,4-Pyridinedicarboxylic Acid
PL	Photoluminescence
PW-PS	Planewave-Pseudopotential
QE	Quantum ESPRESSO package
QM/MM	Quantum Mechanics/Molecular Mechanics
RIM	Restriction of Intramolecular Motions
RIR	Restriction of Intramolecular Rotations
RIV	Restriction of Intramolecular Vibrations
RG	Runge-Gross
RO	Restricted Open-shell
ROY	5-Methyl-2-[(2-nitrophenyl)amino]-3-thiophenecarbonitrile
RPA	Random Phase Approximation
RSH	Range-Separated Hybrid exchange-correlation functional
SA	Salicylidene Aniline
SCF	Self-Consistent Field
TCNE	Tetracyanoethylene
TD	Time-Dependent
TDDFT	Time-Dependent Density-Functional Theory
TS-vdW	Tkatchenko-Scheffler van der Waals method
UFF	Universal Force Field
UHF	Unrestricted Hartree-Fock
UV	Ultraviolet
VMD	Visual Molecular Dynamics

Abbreviation	Description
XDM	Exchange-Hole Dipole Moment dispersion model
ZnBC-BC	Zincbacteriochlorin-Chlorin dimer
2,7-diaryl-TAP	2,7-diaryl-[1,2,4]triazolo[1,5-a]pyrimidine
9-ACA	9-Acetylanthracene

Symbol	Description
$\boldsymbol{a}_i$	Real-space unit-cell vector
a_{X}	Exact-exchange mixing percentage
$\boldsymbol{A}$, $\boldsymbol{B}$	Casida-equation submatrices
a.u.	Atomic unit
$A_{\alpha M}$, $B_{\alpha M}$	Lennard-Jones potential fitting parameters
a_1, a_2	XDM damping parameters
Å	Angstrom
$\boldsymbol{b}_i$	Reciprocal lattice vector
c_i	Linear-combination coefficients
C_n $(n = 6, 8, 10)$	Dispersion coefficients
$\boldsymbol{d}_X$	Exchange-hole dipole moment
E	Energy (see main text for specific definitions)
erf	Error function
eV	Electron volt
e^-	Unit electron charge
E^*	Enol-form excited state
$\boldsymbol{F}$	Eigenvector of the frequency-dependent matrix
f_n $(n = 6, 8, 10)$	Becke-Johnson damping function
f_{xc}	Exchange-correlation kernel
GPa	Gigapascal
$\hat{H}$	Hamiltonian operator
H^{cryst}	Crystalline enthalpy
h_X	Exchange hole
H_{12}	Correlated singlet-triplet energy splitting
i	Imaginary unit
$\boldsymbol{k}$	Wave vector

Symbol	Description
kcal/mol	Kilocalories per mole
K^*	Keto-form excited state
nm	nanometer
$\langle \hat{O} \rangle$	Expectation value of a generic observable
p	Pressure
P_{max}	Maximum applied pressure
q	Double index for Kohn-Sham single excitation
q_M	Effective charge of the Mth MM atom
Q_σ	Curvature
R	Intermolecular distance between the dimer moieties
$\boldsymbol{R}$	Bravais lattice vector
$\boldsymbol{r}$	(Electronic) Position vector
r_{iM}	Distance between the ith QM electron and the Mth MM atom
$R_{\alpha M}$	Distance between the αth QM nucleus and the Mth MM atom
r_{12}	Distance between electron 1 and electron 2
S_0	Singlet ground state
S_1	First singlet excited state
t	Time
T	Kinetic energy
$\mathcal{T}$	Linear transformation operator
T^{corr}	Correlated kinetic energy
T_1	First triplet excited state
$u_n(\boldsymbol{k})$	Periodic wavefunction component at $\boldsymbol{k}$ for the nth electron
V	Potential energy, or volume
V^{corr}	Correlated potential energy
v_{ext}	External potential
V_i	Atomic volume of atom i
v_{KS}	Kohn-Sham potential
v_{xc}	Exchange-correlation potential
x	Magnetization bias magnitude
$\boldsymbol{z}$	Unit vector along the z-direction

Symbol	Description
Z_α	Effective charge of the αth QM nucleus
α_i	Atomic polarizability of atom i
α, β	Up-spin, down-spin
ΔE	Energy gap or difference (see main text for specific definitions)
δ_{ij}	Kronecker delta
$\Delta\Pi$	Electron pair-density difference
ϵ	Kohn-Sham orbital energy
Γ	Momemtum-space Gamma k-point
θ_{thio}	Internal rotation dihedral angle of the ROY molecule
λ	Convergence factor
$\lambda_{\text{max}}^{\text{abs/emi}}$	Maximum absorption/emission wavelength
ρ, $\tilde{\rho}$	Electron density
σ	Spin coordinate
τ	Kinetic-energy density
Φ	Kohn-Sham electronic wavefunction
ϕ	Kohn-Sham orbital, or partial wavefunction
ψ, $\lvert\Psi\rangle$	Electronic wavefunction
$\tilde{\psi}$, $\lvert\tilde{\Psi}\rangle$	Pseudo electronic wavefunction
ψ^*	Complex conjugate of the electronic wavefunction
χ_σ	Reduced spin-density gradient
χ, χ_{KS}	(Kohn-Sham) Linear response function
Ω	Unit-cell volume
ω	Frequency, or long-range HF mixing factor
$\mathbf{\Omega}(\omega)$	Frequency-dependent matrix
$^\circ$	Degree
%	Percentage
∇	Gradient operator
∇^2	Laplace operator

Abstract

Photon-induced electronic excitation of organic chromophores in molecular crystals has received much attention due to potential applications in organic electronics, optics, and biomedicine. Theoretical modeling can aid our understanding of the excitation processes and becomes necessary for high-throughput screening of candidate materials for potential applications. However, predicting photoluminescence (PL) properties in the solid state is complex, as the excitation energies may shift drastically from their gas-phase counterparts. Also, these properties can be significantly influenced by subtle changes in the intermolecular interactions caused by different modes of crystal packing or molecular compositions within the solid-state material.

This thesis aims to develop a novel computational methodology to achieve accurate and cost-efficient prediction of single-electron excitation energies in molecular crystals. Our methodology combines periodic-boundary and single-molecule density-functional theory (DFT) calculations. The periodic-boundary DFT method is paired with the exchange-hole dipole moment (XDM) dispersion model to accurately describe the intermolecular interactions within the crystal lattice. An efficient correction scheme, the virial exciton model, is then employed to obtain the singlet-triplet energy splitting in the first single-electron excited configuration from gas-phase molecular calculations, leading to the prediction of the singlet excitation energies.

Herein, we detail the design, validation, and application of our novel computational methodology. Initial studies probe the effect of electronic excitations on London dispersion, and test the reliability of the virial exciton model for charge-transfer excitations. These studies provide validation for some key assumptions in the devised methodology. Our methodology is then applied to model a variety of solid-state PL properties in diverse sets of luminescent molecular crystals. These investigations encompass topics including piezochromism, polymorphism-dependent PL, and coformer-dependent PL. Our methodology proves highly successful in replicating the experimentally-observed PL behaviors of the investigated molecular crystals, demonstrating excellent reliability and transferability. Valuable insights into the underlying mechanisms of the investigated solid-state PL properties are also obtained through our results.

We hope that the research presented herein could lead to accelerated theory-guided design and screening of industrially valuable solid-state luminescent materials. It may also uniquely contribute to the general understanding of the fundamental nature of electronic excitations in the solid state.

Acknowledgements

I first thank my co-supervisors Prof. Erin Johnson and Prof. Emeritus Axel D. Becke. Their passion and brilliance in scientific research have been a constant inspiration in my young academic career, and their commitment to the development of their graduate students is truly phenomenal. Without their guidance and input, the work herein presented would be all but impossible. I thank Prof. Alexander Speed and Prof. Aaron Kelly for having been on my graduate committee since the start of my MSc program, and Prof. Jesse Maasen and Prof. Josef Zwanziger, who joined my PhD program committee in 2018 and in 2020, respectively. I am also indebted to former and current group members and research associates: Dr. Stephen Dale, Dr. Matthew Christian, Dr. Luc LeBlanc, Alastair Price, Joseph Weatherby, Kyle Bryenton, Tilas Kabengele, Fouad Kaadou, Alex Mayo and Sarah Clarke, for their generous help with academic matters, their comradeship and invaluable advice on assorted daily-life issues; Prof. Alberto Otero de la Roza for his coding ingenuity, which has an important role in the work herein presented.

My special gratitude to my family back in Sichuan, China half a world away: Mom, Dad and Grandma, for their unconditional love and support. I understand that they suffer constantly from the separation from their beloved only child/grandchild, especially during this unprecedented and trying time, and this I will never be able to fully repay. I look forward to reuniting with them in the near future.

Finally, I thank Dalhousie University and the Chemistry Department for providing me the opportunity to pursue my graduate study, the Government of Nova Scotia and the Natural Sciences and Engineering Research Council (NSERC) of Canada for financial support, and Compute Canada for providing the vital computational resources.

Chapter 1

Introduction

1.1 Background

Photon-induced electronic excitations are ubiquitously observed in nature for molecules both in solutions and in solids. In the solid state, a great variety of light-absorbing and -emitting organic molecular crystals display interesting luminescent properties.[1] Such luminescent properties form the basis of important applications in fields such as photovoltaics, optics, and biomedicine. Prominent examples include crystalline dyes,[2,3] fluorescent sensors,[4–6] organic light-emitting diodes (OLEDs),[7–9] lasers,[10] and biomedical imaging.[6,11] Experimental investigation of the factors controlling luminescent properties in molecular crystals, in particular the absorption/emission energies and the corresponding spectra, has attracted much interest. In the field of crystal engineering,[12] many strategies are currently under development to fine-tune[13–15] the absorption/emission spectra to obtain desired luminescent characteristics. Examples of these novel crystal-engineering strategies include co-crystallization,[15–19] exploration of the effects of polymorphism,[18,20–24] and exploitation of aggregation to constrain non-emissive pathways among species featuring Aggregation-Induced Emission (AIE).[2] These synthetic strategies lead to a plethora of novel luminescent properties, such as multi-color absorption or emission,[16,18] thermochromism,[22,25] mechanochromism,[23,26] and piezochromism[27–30] (see Figure 1.1 for an illustrative example).

The variety of both synthetic strategies and the resulting luminescent properties in molecular crystals indicates that many factors can significantly affect their electronic excitations. The absorption/emission energies of species often change

Figure 1.1: Pressure-dependent luminescence (piezochromism) observed for the boron diketonate crystal by Wang *et al.*[29] Top left: photographs of the crystal under a) daylight; b) UV radiation. Top right: molecular structure of boron diketonate. Middle: reversible changes of the emission color during the compression/decompress cycle, along with the fluorescent microscope image of the single crystal. Bottom: experimental emission profile of the boron diketonate crystal under varying pressure. All images were extracted from Ref. 29. Figures reused with permission from Wang *et al.*, Adv. Mater. **27**, 2918-2922 (2015). Copyright 2015 Wiley-VCH.

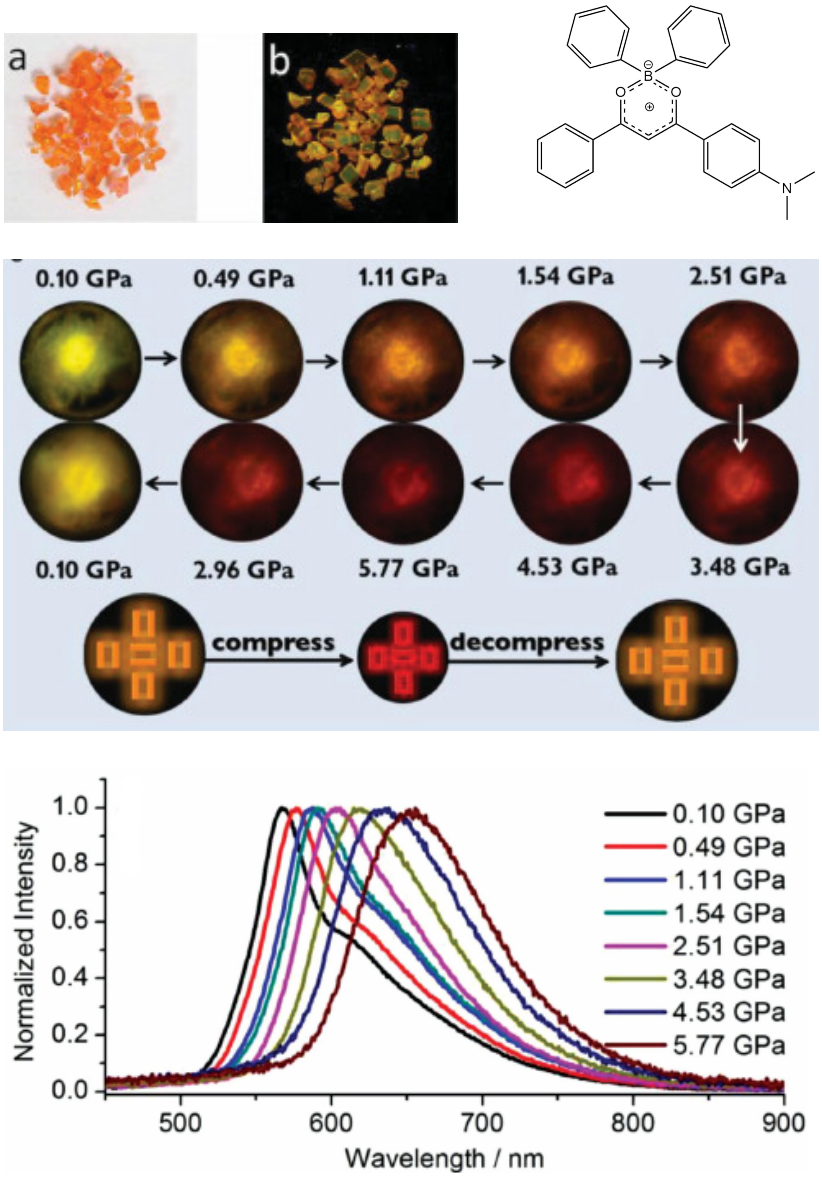

significantly going from the gas or solution phase to the solid phase.[31,32] This suggests that excitation processes in molecular crystals could be noticeably different from their gas-phase counterparts. Within the solid state, different modes of crystal packing may significantly influence both ground and excited states via intermolecular interactions within the crystal structure[12,16,17,33–35] – namely electrostatics, hydrogen- and halogen-bonding, π-stacking, London dispersion, and other van der Waals interactions.

Current works in synthesizing molecular crystals with novel luminescence behaviors could be regarded as efforts in mapping out the excitation-energy landscape in the molecular crystal regime of chemical space,[36] which refers to the ensemble of all possible chemical species. The near-infinite number of possible species calls for the development of viable theoretical approaches to screen the candidate crystalline materials for potential applications utilizing the predicted luminescent properties, before substantial material-resources and human efforts are committed to their syntheses and characterizations. Computations can also offer insights into the fundamental nature of the electronic excitation processes in the solid state and promote our understanding of the effect of various intermolecular interactions on these processes, thereby aiding the explanation of the unconventional luminescent properties in novel molecular crystals as they appear in synthetic laboratories.

1.2 Contemporary Theoretical Works

Computational modeling of excited-state properties in crystalline organic chromophores is still a very young field. Currently, the QM/MM (quantum mechanics/molecular mechanics) embedding approach is the predominant theoretical method employed. The prediction accuracy, while in many cases satisfactory using the QM/MM scheme, can be further improved via applying fully QM-based, *ab initio* electronic structure theories. However, moving to fully *ab initio* treatment of the excitation processes in crystalline organic chromophores faces significant obstacles, one of which is the rapid scaling of the computational cost of conventional excited-state methods, which is only exacerbated by the necessity of invoking periodic-boundary conditions.

1.2.1 The QM/MM Embedding Approach

In short, QM/MM embedding methods[37–39] treat a periodic solid by partitioning the system into the surroundings and embedded-cluster subsystems. The surroundings, which comprise the bulk of the periodic solid, are simulated with low-cost, classical MM methods. The MM methods mostly employ Newtonian force fields with fitted parameters describing the potential-energy surface of the modeled system with respect to bond stretching, bond-angle bending, dihedral torsion, long-range van der Waals interactions (usually approximated by the Lennard-Jones potential), and electrostatic Coulomb interactions. Examples of widely used MM force fields include Assisted Model Building with Energy Refinement (AMBER),[40,41] the Generalized AMBER Force Field (GAFF),[42] the Universal Force Field (UFF),[43] and Chemistry at HARvard Macromolecular Mechanics (CHARMM).[44] The embedded cluster is the region of particular interest, in which the modeled excitation process takes place. The embedded cluster is described by QM methods to a much higher accuracy, with the influence of an interacting potential that represents the surroundings. For modeling excited states, the QM method is most commonly time-dependent density-functional theory, TDDFT.[45,46]

Within the QM/MM framework, the total energy of the entire system is partitioned as:

$$E_{total} = E^{v}_{\mathrm{QM}} + E_{\mathrm{MM}} + E_{\mathrm{QM\text{-}MM}}. \tag{1.1}$$

E^{v}_{QM} is the energy of the embedded QM system subject to the external electrostatic field, v, generated by the MM subsystem; this embedding method is termed "electrostatic embedding".[47] E_{MM} is the MM energy of the surroundings, which sums over all bonded and non-bonded interactions between centers exclusively within the MM surroundings. The final term, $E_{\mathrm{QM\text{-}MM}}$, is the interaction energy between the QM and the MM subsystems. Among these three terms, $E_{\mathrm{QM\text{-}MM}}$ is the most intricate to model as it suffers from the inconsistency between QM and MM methods.

The QM-MM interactions are usually expressed as the sum of the electrostatic and van der Waals interactions between the centers within the QM subsystem and the centers within the MM subsystem. This simplified QM-MM interaction term

can be expressed by the QM-MM Hamiltonian, $\hat{H}_{\text{QM-MM}}$:

$$\hat{H}_{\text{QM-MM}} = -\sum_{iM} \frac{q_M}{r_{iM}} + \sum_{\alpha M} \frac{Z_\alpha q_M}{R_{\alpha M}} + \sum_{\alpha M} \left[\frac{A_{\alpha M}}{R_{\alpha M}^{12}} - \frac{B_{\alpha M}}{R_{\alpha M}^{6}} \right], \tag{1.2}$$

where i and α are the indices of the electrons and the nuclei within the QM subsystem, respectively, and M is the index of the atoms within the MM subsystem. These indices imply that electrons and nuclei are treated as separate entities within the QM subsystem, while the MM subsystem is treated only as a collection of atoms. Furthermore, r_{iM} refers to the electron-atom distance between QM-electron i and MM-atom M, whereas $R_{\alpha M}$ is the nucleus-atom distance between QM-nucleus α and MM-atom M. The first two terms in eq. 1.2 represent the electrostatic interaction between the QM and the MM subsystems, where the atoms and the nuclei in the MM and QM subsystems are assigned effective point charges, q_M and Z_α, respectively. Since the first term involves the interaction between the QM electrons and MM nuclei, it is incorporated into the QM Hamiltonian as the electrostatic embedding. The third term represents the QM-MM van der Waals interaction which is approximated by the "6-12"-type Lennard-Jones potential with fitted parameters, $A_{\alpha M}$ and $B_{\alpha M}$, for each QM-nucleus/MM-atom pair, typically assigned based on force-field atom types.

The definition of the boundary between the QM and the MM subsystems is rather arbitrary and is often chosen via a trail-and-error approach. An issue arises if the same large molecule (such as a protein) is divided by the QM-MM boundary, as this involves cutting covalent bonds. In this case, a common solution is to attach a "link atom",[47] usually an H atom or a pseudo-atom parametrized to mimic the absent linking group,[48,49] to the MM end of the cut bond and incorporate it into the QM treatment. The link atom is set to have no interaction with the MM subsystem.

An alternative formulation of the QM/MM scheme is the "Our own N-layered Integrated molecular Orbital molecular Mechanics" (ONIOM) method developed by Morokuma *et al.* during the mid-1990s.[50,51] The ONIOM method is a subtractive scheme, compared to the additive QM/MM formulation of eq. 1.1. The ONIOM energy is

$$E_{\text{ONIOM(QM:MM)}} = E_{\text{QM}}^{\text{model}} + E_{\text{MM}}^{\text{real}} - E_{\text{MM}}^{\text{model}}, \tag{1.3}$$

where $E_{\mathrm{QM}}^{\mathrm{model}}$ and $E_{\mathrm{MM}}^{\mathrm{model}}$ are respectively the QM and MM energies of the QM ("model") subsystem, and $E_{\mathrm{MM}}^{\mathrm{real}}$ is the MM energy of the full ("real") system. Double-counting of interactions within the QM subsystem is offset by subtracting the energy resulting from an MM calculation on the same subsystem. Note that in the ONIOM scheme, the low-level method is not restricted to MM – a low-level QM method (QM′), such as Hartree-Fock (HF) theory, can be used instead.

An extension of ONIOM divides the system into three subsystems:

$$E_{\mathrm{ONIOM(QM1:QM2:MM)}} = E_{\mathrm{QM1}}^{\mathrm{model}} + E_{\mathrm{QM2}}^{\mathrm{intermediate}} - E_{\mathrm{QM2}}^{\mathrm{model}} + E_{\mathrm{MM}}^{\mathrm{real}} - E_{\mathrm{MM}}^{\mathrm{intermediate}}, \quad (1.4)$$

where "intermediate" denotes an intermediate subsystem that is smaller than the real system and contains the model subsystem. The central model subsystem is treated with a high-level QM method (denoted QM1), the intermediate subsystem with a low-level QM method (QM2), and the real system with MM. The subtractive terms remove the double-counting of both the model and the intermediate subsystems. In principle, the ONIOM method can be extended to an arbitrary N-layer, although it has yet to be widely implemented for N = 4 and beyond.[52]

The QM/MM methodology allows for treatment of systems whose sizes range from over several hundred to several thousand atoms, making it highly popular in the simulation of large-scale biochemical systems, such as complex protein structures.[53,54] It is also the currently predominant method for modeling localized excitations in molecular crystals. However, there exist major shortcomings within the QM/MM methodology. One of them is the absence of Pauli repulsion[55] between QM and MM subsystems, as the non-bonded QM-MM interactions are treated classically using the Lennard-Jones potential. This issue becomes pronounced in regions near the QM-MM boundary, where the lack of Pauli repulsion causes unphysical penetration of the QM-electron density into the MM subsystem, which can lead to significant over-binding between QM and MM atoms.[55] Another problem results when solvated-cluster models with extensive H-bonding networks are broken by the QM/MM partitioning. Exclusion of H-bond donors lying outside the model system from the QM calculation can result in artificial accumulation of electron density at the boundary.[56] In addition, the accuracy of the ONIOM scheme is

highly dependent on error cancellation between the model-system QM and the real-system MM calculations, which typically requires the trial-and-error testing of many combinations of high/low-level methods on a smaller sample system.[52]

1.2.2 Applications of QM/MM to Crystalline-Phase Excitations

A large portion of the contemporary literature applying QM/MM to solid-state electronic excitations focuses on modeling systems that display the Aggregation-Induced Emission (AIE) effect,[2] which was first conceptualized by Tang *et al.* in 2001.[57] A species displays AIE when its emission is enhanced or induced by increasing degrees of aggregation (e.g. going from a dilute solution to solvated clusters, and eventually to a molecular crystal). The AIE effect contradicts the conventional Aggregation-Caused Quenching (ACQ) effect.[58] ACQ is typically observed in systems featuring strong π-π stacking interactions in its aggregated forms,[59] which are prohibited in typical AIE systems by high steric hindrance. The working mechanism of AIE is understood mainly as restrictions on two non-radiative relaxation pathways induced by aggregation: restriction of intramolecular rotations (RIR)[60] and restriction of intramolecular vibrations (RIV),[61] which are collectively termed restriction of intramolecular motions (RIM).

In one of the earliest computational studies of the exited-state properties of organic molecular crystals, Li *et al.*[62] applied the ONIOM(TDDFT:UFF) scheme to model the ground and excited states of the AIE-active diphenyldibenzofulvene (DPDBF) crystal. Later, Shuai *et al.*[63–66] employed the QM/MM (TDDFT/GAFF) methodology to investigate the AIE mechanism in a series of AIE-active crystals. Their results showed good agreement with the experimentally-observed absorption/emission spectra for the investigated systems. By analyzing the calculated shifts in the geometry and energetics of the excited state going from the gas/solution phase to the crystalline phase, they confirmed the role of RIR in affording AIE activity. In a joint experimental/computational study, Bu *et al.*[67] employed an ONIOM(TDDFT:MM) scheme to model the excited-state crystal structure of an unconventional rotor-less coumarin derivative that is AIE-active. Aided by the ONIOM results, they demonstrated that restriction of out-of-plane vibration, rather than RIR, caused the observed AIE activity in their coumarin derivative. Other

works by Wang *et al.*[68] and Peng *et al.*[69] also used a similar ONIOM framework to supplement the RIM understanding of the AIE phenomenon. They revealed that restriction of access to the charge-transfer intermediate state, and to the conical intersection between the potential-energy surfaces of the ground and excited states, could also be part of the AIE mechanism. More recent works on the AIE mechanism employing QM/MM include those of Naito *et al.*[70] and Presti *et al.*[71]

Another crystalline-phase excitation phenomenon that has drawn theoretical attention recently is the excited-state intramolecular proton transfer (ESIPT) process in molecular crystals.[72] ESIPT refers to a photochemical process where the excited molecule undergoes tautomerization via rapid (picosecond timescale) proton transfer(s) between its enol (E^*) and keto (K^*) forms, before decaying back to the ground state via either radiative or non-radiative pathways. ESIPT requires the presence of an intramolecular H-bond between the proton donor and the proton acceptor groups.[73] Chromophores that undergo ESIPT typically feature dual emission (from both E^* and K^*), large Stokes shifts, and high sensitivity to the crystalline environment.[74]

Presti *et al.*[75,76] applied their computational protocol (also used in Ref. 71 for studying the AIE mechanism) to model the ESIPT process in molecular crystals, using salicylidene aniline (SA) as a case study. Their proposed protocol involves three steps: (i) optimization of the crystal structure using a dispersion-corrected DFT method adapted to periodic-system calculations;[77] (ii) identification and isolation of the model cluster within the crystal structure; and (iii) applying the ONIOM(TDDFT:HF) scheme to calculate the vertical excitation energy of the model cluster, where the crystalline environment is represented by point charges in the low-level region.[78] They were able to qualitatively reproduce the absorption and emission spectra of the trans- and cis- forms of the K^* of SA, although quantitatively their results were strongly dependent on the choice of exchange-correlation functional used in the ONIOM scheme.

The same group later modeled the excitation and emission in the 1,8-dihydroxy-2-naphthaldehyde (DHNA) crystal,[79] which has been experimentally shown[80] to undergo excited-state intramolecular double proton transfer (ESIDPT). This is a special case of ESIPT, where two excited-state proton transfers happen in

succession among three adjacent enol/keto positions. The authors combined the ONIOM(TDDFT:HF) scheme with an external point-charge background that was calculated self-consistently with respect to the charge density of the excited molecule. They found that the inclusion of a self-consistent point-charge background significantly improved the prediction of the emission energy shifts of DHNA from the solution phase to the crystalline phase. Their model was able to capture the different levels of destabilization of the two excited-state keto forms exerted by the crystalline environment, which explained the solution-to-crystal shift in the relative intensities of the two emission peaks of DHNA.

Recently, Dommett *et al.*[81] investigated two molecular crystals based on 2′-hydroxychalcone, both featuring ESIPT and having drastically different AIE activities (one is AIE-active, the other is non-emissive in both solution and crystalline phases). The authors modeled the excited states of the two crystals using the ONIOM(TDDFT:AMBER) scheme. They modeled multiple decay pathways of E^* and K^* in both crystals, including access to the minimum-energy conical intersection (MECI)[82] (a common non-radiative pathway) between the excited and ground states of the keto form in the ESIPT process. They concluded that the differing AIE activities of the two crystals result from the interplay between multiple intermolecular and intramolecular factors. These factors include differing levels of stabilization of E^*, K^*, and the keto-form MECI by the electrostatic potential of the crystalline environment, which are crucial in determining the accessibility of the keto-form MECI in both crystals.

1.2.3 TDDFT Applied under Periodic-Boundary Conditions

While still faced with many challenges mainly associated with the exceedingly high computational cost, applying full TDDFT to a periodic solid is not impossible. However, efforts in this direction are still relatively scarce, as the implementation of full TDDFT under periodic-boundary conditions is currently at a largely experimental stage. Among the contemporary literature, we note the recent work by Arhangelskis *et al.*,[83] where they devised a periodic-boundary TDDFT algorithm based on Hutter's[84] re-formulation of linear-response TDDFT (LR-TDDFT, for more details see Sec. 2.2.2). Hutter's formalism essentially adapted the LR-TDDFT

equations to a planewave basis, which allowed for higher computational efficiency in applications to periodic solid systems.[84] The periodic-boundary TDDFT algorithm of Arhangelskis *et al.* extended Hutter's original formulation, which assumed only the special Γ point, to any arbitrary k-point in momentum space[83] and was implemented in the CASTEP[85] planewave-DFT code. Limited by the prohibitive computational cost of sampling more than one k-point during the periodic-boundary TDDFT excited-state calculation, the authors resorted to Baldereschi's[86] idea of a mean-value k-point, where an optimum single k-point is chosen for each crystal lattice to represent an average of the whole Brillouin zone.[87]

Using their planewave TDDFT method, Arhangelskis *et al.* computationally predicted[83] the emission spectra of a set of 4 cocrystals formed between 1,4-bis(2-cyanostyryl)benzene and 4 different halogenated benezenes (see Figure 1.2), previously shown to demonstrate coformer-dependent emission.[16] Their approach

Figure 1.2: Chemical structure of 1,4-bis(2-cyanostyryl)benzene (**A**) and its four coformers (**1** to **4**); images of the corresponding fluorescent cocrystals[16] are shown below. Image extracted from Ref. 83. Figure reused with permission from Arhangelskis *et al.*, J. Phys. Chem. A **122**, 7514-7521 (2018). Copyright 2018 American Institute of Physics.

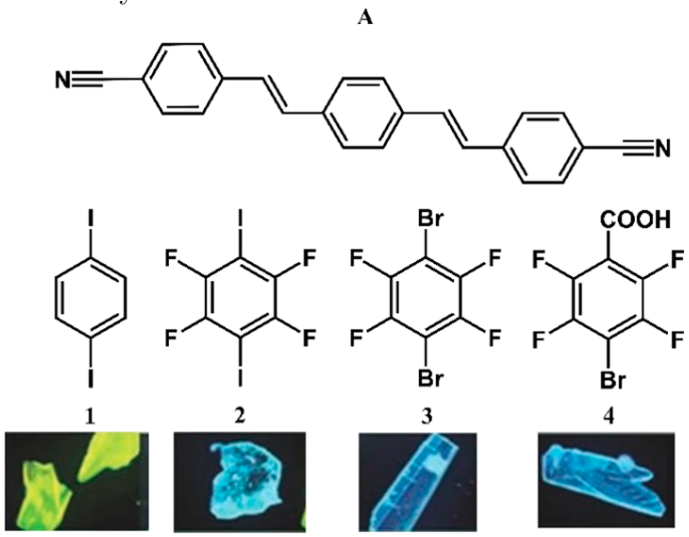

employed a combination of DFT/TDDFT geometry optimizations (using the PBE[88] density functional and Grimme's D2 dispersion correction[89]) and single-point TDDFT excited-state calculations (using the B3LYP[90] density functional). Arhangelskis *et al.* were able to reproduce the experimental emission spectra of

these cocrystals with good accuracy, obtaining a mean absolute error of roughly 0.2 eV in the calculated emission maxima. Furthermore, the authors offered a theoretical rationalization of the red-shift in the emission color of **A1** from the other 3 cocrystals from analysis of the crystal geometries. The authors theorized that species **A1**'s monoclinic lattice allowed for significant $\pi - \pi$ stacking between **A** and coformer **1**, which was absent in the triclinic lattices of cocrystals **A2**, **A3**, and **A4**, leading to **A1**'s emission red-shift.

Ref. 83 is a pioneering effort in the implementation of planewave TDDFT and its application to calculating the excitation energies of periodic solids, although more work is ahead towards truly mature planewave TDDFT for solid-state applications. In Ref. 83, the authors were limited by the insurmountably high cost of using a consistent hybrid density functional for both the TDDFT energy calculations and geometric optimization of the excited states. This is notwithstanding the fact that the computational cost of conducting single-point planewave TDDFT calculations using a hybrid density functional is already too high for many experimentally-oriented researchers to afford. Additionally, Ref. 83's periodic-boundary TDDFT calculations were confined to using a single mean-value k-point, also due to the high cost of including more than one k-point. This mean-value k-point needs to be determined on a case-by-case basis, which could be a quite involved process,[83] thereby potentially hampering the method's general applicability.

Prior to the implementation of their periodic-boundary TDDFT algorithm, Arhangelskis *et al.* studied the colorations of fluorescein crystals using periodic-boundary band-structure calculations (for more details, see Sec. 2.4.6) in a joint experimental-computational study.[91] Although the calculated crystalline band-gap values were significantly underestimated relative to the experimental measurements of the fluorescence energies, good qualitative agreement in the relative rankings of the quinoid, zwitterionic and lactoid forms of the fluorescein crystal (see Figure 1.3) was obtained. Thus, the calculations were able to explain the differences in coloration between these 3 tautomeric crystalline forms. In addition, band-structure calculations were conducted on various cocrystals formed between the lactoid fluorescein and acridine, phenanthridine, and pyrazine.[92] The results of these calculations demonstrated that the presence of a coformer could potentially modify the band

Figure 1.3: The 3 tautomeric forms of fluorescein:[91] quinoid (**flsQ**); zwitterionic (**flsZ**); and lactoid (**flsL**).

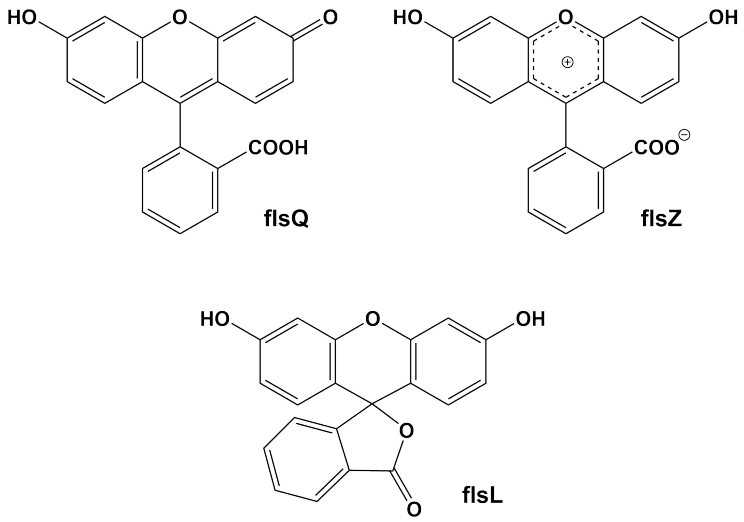

structure of the cocrystal, thus altering its optical and electronic properties.[91] Periodic-boundary band-structure calculations were similarly employed in previous work by Sander *et al.*[93] Combined with analysis of the total density of states,[94] the authors were able to use the calculated band structures to rationalize the red coloration of the cocrystal of acetaminophen (APAP) and 2,4-pyridinedicarboxylic acid (PDA), while the pristine crystals of APAP and PDA are both colorless.

1.3 Thesis Goals

In this work, we devise, validate, and implement a novel approach for fast and accurate modeling of the first singlet excitation energy in crystalline organic chromophores. We intend to achieve high prediction accuracy, improving upon the level of the currently predominant QM/MM embedding scheme, while reliably handling difficult cases such as excitations with significant charge-transfer character. Additionally, we design our scheme to maintain a moderate computational cost and we will rely on well-established computational codes for implementation simplicity. In order to achieve these goals, the following issues must be properly addressed:

- The periodic crystalline environment could cause a significant shift in the nature of both the ground and excited states of the chromophore with respect

to the gas phase. Therefore the crystalline bulk needs to be reliably modeled, and the effect of the crystalline surroundings on the ground and excited states of the chromophore accurately quantified.

- Intermolecular interactions, in particular $\pi - \pi$ interactions, halogen- and hydrogen-bonding, could conceivably have a non-trivial impact on the excited states of the crystalline organic chromophore. They must be properly described.

- One major failure of LR-TDDFT is the modeling of charge-transfer (CT) excitations,[95,96] which are ubiquitous in organic chromophores. Conventional exchange-correlation functionals massively underestimate CT excitation energies. Using range-separated hybrid (RSH) functionals alleviates this problem to some extent,[97,98] but does not offer a cure. In addition, the RSH approach is currently only practical in gas-phase calculations due to the high cost associated with computing the HF exchange energy in an extended periodic system. Going beyond the AA and the LR formalism may further improve the accuracy, although this also comes with a drastic increase in computational cost and is still scantily explored even for gas-phase molecules. It is our intention to depart from the time-dependent theories altogether, using conventional ground-state DFT to afford an efficient, yet still *ab initio*, treatment of the problem.

- Conventional ground-state DFT is known to yield adequate predictions of the ground-state and first triplet-state energies (E_0 and E_T, respectively) and, therefore, of the triplet excitation energy ($E_{0\mathrm{T}} = E_\mathrm{T} - E_0$) in molecules. This is due to the single-determinant nature of these states.[99] However, modeling of singlet excitation energies ($E_{0\mathrm{S}}$), which is of primary interest and importance in the absorption/emission spectra of organic chromophores, is problematic for DFT due to their inherently multi-determinantal nature. While modeling of $E_{0\mathrm{T}}$ is a reliable starting point, the key problem remains in correcting $E_{0\mathrm{T}}$ towards $E_{0\mathrm{S}}$. Becke recently showed that such a correction can be efficiently achieved and provided a working scheme.[99,100]

- Under the assumption that both the triplet and the singlet excited states of the

chromophore are influenced very similarly by the intermolecular interactions in the crystalline surroundings, a direct additive correction from $E_{0\mathrm{T}}$ towards $E_{0\mathrm{S}}$ would seem viable. We are hopeful that Becke's singlet-excitation scheme will also yield accurate results for CT excitations in organic chromophores, although this needs to be tested for a selection of systems known to pose the CT-excitation problem for TDDFT.

- The devised methodology is intended to treat the first singlet transition energies in both the absorption and emission spectra. For absorption, the vertical excitation energy is calculated using the same geometry for both the ground and excited states, as absorption takes place almost instantly as the excited moiety interacts with the incident photon with a matching quantum of energy. For emission, the situation is less straightforward because of the significant elapse of time (compared to absorption), which allows the excited moiety to reorganize and relax to a metastable intermediate state, typically via some non-radiative pathway, before releasing a photon and returning to the ground state. This argument is commonly used as an explanation for the Stokes shift ubiquitously observed in the photoluminescence (PL) spectra of both solutions and solids. The relaxation of the excited-state geometry needs to be taken into account in the modeling of emission energies.

- Comparison with the experimentally observed absorption/emission spectra of the investigated species needs to be made to assess the overall reliability of the proposed approach. Such a comparison should also be instrumental in uncovering any unexpected issues with the proposed modeling methodology. For example, we are neglecting thermal effects in our currently-proposed scheme (all calculations are conducted at 0 K), which might potentially affect our predictions of the first singlet excitation energies. It is our hope that analysis of the discrepancies between our theoretical predictions of transition energies and the experimental data will serve to provide valuable insights into the fundamental nature of the electronic processes in crystalline organic chromophores.

1.4 Layout of the Remaining Chapters

The following chapters are dedicated to our own efforts towards the computational modeling of electronic excitations in the solid state, specifically to the prediction of absorption/emission energies in crystalline organic chromophores. Chapter 2 aims to provide the reader a theoretical preparation for the computational methods involved in this thesis. Theoretical topics including density-functional theory (DFT), time-dependent DFT, the virial exciton model,[99,100] periodic-boundary DFT, practical considerations for solid-state calculations using Quantum ESPRESSO,[101] and the exchange-hole dipole moment (XDM) dispersion model,[102–104] are discussed in necessary detail. In Chapter 3, we present a preliminary study that assesses the effect of electronic excitations on London dispersion in molecular and crystalline systems. In Chapter 4, we benchmark the virial exciton model, which plays an integral role in our proposed computational methodology, for electronic excitations featuring significant charge transfer. Such a benchmark is important as charge-transfer excitations post significant challenges for conventional TDDFT methods. In Chapter 5, we offer a detailed description of the design of our computational methodology, and present the results from exploratory calculations as a proof of concept. Chapters 6 and 7 describe the full application of our methodology to modeling the PL properties of a variety of molecular crystals. We show the success of our approach in efficiently and accurately reproducing diverse novel solid-state PL phenomena observed in experiments, including piezochromism (Chapter 6), polymorph-dependent PL in polymorphic crystals (Chapter 7), and coformer-dependent PL in cocrystals (Chapter 7). Finally, in Chapter 8, we offer an overall conclusion to this work and provide the reader with an outlook towards future research directions.

Chapter 2

Theoretical Preparation

It is important to note that modeling excited-state properties in solid-state organic chromophores is significantly different than in inorganic solid-state systems, such as inorganic semiconductors. This originates from the fact that solid-state organic chromophores owe their luminescent properties to excitations of a much more localized nature (i.e. short-range, within the same molecule or only between adjacent molecules), as opposed to the delocalized excitations (i.e. over large distances within the material) typically observed in inorganic solids. In the former case, accurately modeling the intermolecular interactions, especially in the region where the excitation is localized, becomes very important. Computational modeling of the excited-state properties of inorganic solid-state materials (e.g. the band gap and the dielectric constant) has a rich history in physics and material science, although this discipline is entirely beyond the scope of this present work. Here we concern ourselves exclusively with the computational modeling of the absorption/emission spectra of organic chromophores in the crystalline phase.

2.1 Density-Functional Theory

Density-functional theory (DFT) has enjoyed enormous success in physics and material sciences since Hohenberg and Kohn's proof in 1964,[105] which established its formal foundation, and the formulation of Kohn-Sham theory,[106] which provided it with a practical working mechanism. Between 1980s and 1990s, with the popularization of generalized-gradient approximations (GGAs)[88,107,108] and hybrid density functionals,[90,109] DFT further expanded into chemistry, biochemistry, and

many other fields. DFT has become the modeling method of choice in the aforementioned fields as it frequently combines predictive accuracy and modest computational cost in modeling the ground-state properties of molecular systems.

In an effort to briefly sketch out the basic principles of DFT, we start from the general time-independent Hamiltonian within the Born-Oppenheimer approximation for an N-electron system:

$$\hat{H} = -\frac{1}{2}\sum_{i=1}^{N}\nabla_i^2 + \sum_{i<j}^{N}\frac{1}{|\boldsymbol{r}_i - \boldsymbol{r}_j|} + \sum_i v_{\text{ext}}(\boldsymbol{r}_i). \tag{2.1}$$

Here $-\frac{1}{2}\nabla_i^2$ is the kinetic energy operator for the ith electron, $\boldsymbol{r}_i$ and $\boldsymbol{r}_j$ are the respective position vectors for the ith and the jth electrons, $\frac{1}{|\boldsymbol{r}_i - \boldsymbol{r}_j|}$ is the repulsive electron-electron interaction operator, and $v_{\text{ext}}(\boldsymbol{r}_i)$ is the external potential operator, which includes the Coulomb attraction between the ith electron and all nuclei in the system, as well as any potential caused by an externally applied electric field. By iteratively solving the N-electron Schrödinger equation,

$$\hat{H}\psi(\boldsymbol{r}_1, \boldsymbol{r}_2, ...\boldsymbol{r}_N, \sigma_1, \sigma_2, ...\sigma_N) = E\psi(\boldsymbol{r}_1, \boldsymbol{r}_2, ...\boldsymbol{r}_N, \sigma_1, \sigma_2, ...\sigma_N), \tag{2.2}$$

where $\boldsymbol{r}_i$ and σ_i are respectively the positional and spin coordinates of electron i, we can obtain the N-electron wavefunction $\psi(\boldsymbol{r}_1, \boldsymbol{r}_2, ...\boldsymbol{r}_N, \sigma_1, \sigma_2, ...\sigma_N)$ and the ground-state energy, E. This can be done using a hierarchy of wavefunction-based methods (i.e. Hartree-Fock (HF) theory, Møller-Plesset second-order (MP2) perturbation theory, coupled-cluster (CC) methods and configuration interaction (CI)). Unfortunately, doing so rapidly becomes infeasible beyond the smallest systems due to the increasingly harsh scaling of computational cost (e.g. N^5 to N^7 for CC methods, and $N!$ for full CI, where N is the number of electrons in the system). Instead, ground-state DFT centers itself around the electron density $\rho(\boldsymbol{r})$:

$$\rho(\boldsymbol{r}) = N\int d\boldsymbol{r}_2...d\boldsymbol{r}_N d\sigma_1 d\sigma_2...d\sigma_N |\psi(\boldsymbol{r}_1, \boldsymbol{r}_2, ...\boldsymbol{r}_N, \sigma_1, \sigma_2, ...\sigma_N)|^2, \tag{2.3}$$

which only relies on 3 spatial coordinates, to obtain ground-state energies of the system. In principle, relying only on $\rho(\boldsymbol{r})$ affords DFT a much more tolerable scaling factor on the order of N^3, making systems of chemically relevant sizes (several tens

to hundreds of atoms and beyond) approachable.

The Hohenberg-Kohn (HK) theorem[105] is an existential proof that established a one-to-one mapping between the external potential and the ground-state electron density:

$$v_{\text{ext}}(\boldsymbol{r}) \leftrightarrow \rho(\boldsymbol{r}). \tag{2.4}$$

Since $v_{\text{ext}}(\boldsymbol{r})$ uniquely defines the time-independent Hamiltonian (eq. 2.1), it also uniquely determines the eigenfunctions and eigenvalues of eq. 2.2. This leads to a unique *functional* relationship between $\psi(\boldsymbol{r}_1, \boldsymbol{r}_2, ...\boldsymbol{r}_N, \sigma_1, \sigma_2, ...\sigma_N)$ and $\rho(\boldsymbol{r})$, which implies that the expectation values of all ground-state observables $\langle\hat{O}\rangle$ are *functionals* of $\rho(\boldsymbol{r})$: $\langle\hat{O}\rangle = \langle\hat{O}\rangle[\rho(\boldsymbol{r})]$. In particular, we have the ground-state energy E as $E[\rho(\boldsymbol{r})]$. The HK theorem also states that the true ground-state $\rho(\boldsymbol{r})$ is found when its corresponding energy is variationally minimized.

Following the HK theorem, the Kohn-Sham (KS) theorem outlines a practical scheme for DFT calculations. The KS theorem maps the true, interacting N-electron system to a fictitious, non-interacting system under an effective KS potential $v_{\text{KS}}(\boldsymbol{r})$. The non-interacting KS system is described by a set of N one-electron Schrödinger equations called the KS equations:

$$\left[-\frac{1}{2}\nabla_i^2 + v_{\text{KS}}(\boldsymbol{r})\right]\phi_i(\boldsymbol{r}) = \epsilon_i\phi_i(\boldsymbol{r}), \tag{2.5}$$

where $\phi_i(\boldsymbol{r})$ is a one-particle KS orbital (here always assumed to be real) of the ith electron, and ϵ_i is its corresponding KS-orbital energy. The non-interacting KS system retains, by definition, the identical ground-state $\rho(\boldsymbol{r})$ of the true, interacting system. For a spin-neutral system, we have:

$$\rho(\boldsymbol{r}) = 2\sum_{i=1}^{N/2}|\phi_i(\boldsymbol{r})|^2. \tag{2.6}$$

$v_{\text{KS}}(\boldsymbol{r})$ can be partitioned as follows:

$$v_{\text{KS}}[\rho(\boldsymbol{r})] = v_{\text{ext}}(\boldsymbol{r}) + \int d\boldsymbol{r'}\frac{\rho(\boldsymbol{r'})}{|\boldsymbol{r}-\boldsymbol{r'}|} + v_{\text{XC}}[\rho(\boldsymbol{r})], \tag{2.7}$$

where the second term on the right side is the Hartree potential representing

the classical Coulomb repulsion between electrons. v_{XC} is the so-called exchange-correlation potential whose exact form is not known.

A perhaps better-known partition is that of the total energy (again assuming a spin-neutral system):

$$E = 2\sum_{i}^{N/2}(-\frac{1}{2})\int d\boldsymbol{r}\phi_i(\boldsymbol{r})\nabla_i^2\phi_i(\boldsymbol{r}) + \int d\boldsymbol{r}v_{\mathrm{ext}}\rho(\boldsymbol{r}) + \frac{1}{2}\iint d\boldsymbol{r}d\boldsymbol{r'}\frac{\rho(\boldsymbol{r})\rho(\boldsymbol{r'})}{|\boldsymbol{r}-\boldsymbol{r'}|} + E_{\mathrm{XC}}[\rho(\boldsymbol{r})], \tag{2.8}$$

with the first to the third terms on the left being the KS kinetic, external, and electron-electron Coulomb interaction energies, respectively. The final term is the exchange-correlation energy. It includes all real-system quantum-mechanical contributions to the electron-electron interactions that are not contained in the first three terms on the left side of eq. 2.8. $v_{\mathrm{XC}}[\rho(\boldsymbol{r})]$ is the functional derivative of $E_{\mathrm{XC}}[\rho(\boldsymbol{r})]$:

$$v_{\mathrm{XC}}[\rho(\boldsymbol{r})] = \frac{\delta E_{\mathrm{XC}}[\rho(\boldsymbol{r})]}{\delta\rho(\boldsymbol{r})}. \tag{2.9}$$

Consequently, the exact form of E_{XC} is also not known. In practice, approximations are made directly to E_{XC} rather than v_{XC}.

With some approximation to $E_{\mathrm{XC}}[\rho(\boldsymbol{r})]$, an operating mechanism emerges for a KS-DFT calculation. One starts with a set of basis functions to constitute an initial guess (*ansatz*) for the KS spin-orbitals. For finite molecular systems, the ansatz is most often constructed as linear combinations of Gaussian-type orbitals such as the "split-valence" basis sets by Pople *et al.* and the "correlation-consistent" basis sets by Dunning *et al.*[110,111] For infinitely-extended systems such as periodic solids, planewave basis sets are used instead, and this will be discussed in greater detail in Section 2.5. From the initial KS spin-orbitals, one can also construct an initial spin-density, and consequentially the initial KS potential, via eqs. 2.6 and 2.7. Solving eq. 2.5 yields improved KS spin-orbitals and an improved spin-density, which is put back into eq. 2.7 to complete the self-consistent field (SCF) loop. Such an SCF loop is repeated until the resulting total energy (from eq. 2.8) variationally converges under a preset threshold.

The development of DFT methods has been centered around obtaining increasingly better approximations to $E_{\mathrm{XC}}[\rho(\boldsymbol{r})]$. Many flavors[112] of density-functional

approximations (DFAs) to $E_{\mathrm{XC}}[\rho(\boldsymbol{r})]$ have been developed since the original local-density approximation (LDA) proposed by Kohn and Sham based on the uniform electron gas.[106] Of great importance in the modern applications of DFT are the so-called generalized gradient approximations (GGAs)[88,107,108] and hybrid functionals.[90,109]

In GGAs, E_{XC} is dependent on both the local electron density $\rho(\boldsymbol{r})$ and its gradient $\nabla\rho(\boldsymbol{r})$:

$$E_{\mathrm{XC}}^{\mathrm{GGA}} = E_{\mathrm{XC}}[\rho(\boldsymbol{r}), \nabla\rho(\boldsymbol{r})]. \tag{2.10}$$

The $\nabla\rho(\boldsymbol{r})$ dependence incorporates density information in the immediately adjacent areas of any reference point $\boldsymbol{r}$. The "semi-local" GGA functionals improve significantly upon LDA, ushering in a new era of greatly expanded applicability of DFT. The most well-known GGA exchange-correlation functional is the PBE functional devised by Perdew, Burke and Ernzerhof in 1996,[88] which has found widespread use, especially in the solid-state physics and material sciences communities (although Becke arrived at the B86a functional[113] a decade earlier with essentially the same mathematical form). The B86b[107] functional, which is employed in this work, is a modification of the B86a[113] (PBE) functional form. It has a large-gradient limit ("large" in the sense of Eq. 2.12 below) that is optimum for weakly bound van der Waals systems. The exchange part (which dominates E_{XC}) of the B86b functional is written as:

$$E_{\mathrm{X}}^{\mathrm{B86b}} = -\sum_{\sigma}\int d\boldsymbol{r}\, c_{\mathrm{X}}\rho_{\sigma}^{4/3}\left[1+\frac{\beta}{c_{\mathrm{X}}}\frac{\chi_{\sigma}^{2}}{(1+\gamma\chi_{\sigma}^{2})^{4/5}}\right], \tag{2.11}$$

where χ_σ is the reduced spin-density gradient:

$$\chi_{\sigma} = \frac{|\nabla\rho_{\sigma}|}{\rho_{\sigma}^{4/3}}, \tag{2.12}$$

and $c_{\mathrm{X}} = \frac{3}{2}(\frac{3}{4\pi})^{1/3}$. The two parameters β and γ are fit to atomic data, and have the respective values of 0.00375 and 0.007.

To further improve the accuracy of DFT, one must go beyond the GGA framework. In pure GGAs, the exchange energy (which is an inherently non-local effect originating from the antisymmetry of the electronic wavefunction) is formally

*in*exact. Meanwhile, the exchange energy is treated in its exact form in HF theory:

$$E_{\mathrm{X}}^{\mathrm{exact}} = -\frac{1}{2}\sum_{\sigma}\sum_{ij}\iint d\boldsymbol{r}_1 d\boldsymbol{r}_2 \frac{\phi_{i\sigma}(\boldsymbol{r}_1)\phi_{j\sigma}(\boldsymbol{r}_1)\phi_{i\sigma}(\boldsymbol{r}_2)\phi_{j\sigma}(\boldsymbol{r}_2)}{|\boldsymbol{r}_1 - \boldsymbol{r}_2|}, \tag{2.13}$$

where the orbitals have been supplemented with the spin indices σ, signifying that the exchange effect only exists between same-spin electrons. Hybrid functionals improve their description of the exchange energy by incorporating a certain portion of exact (HF) exchange:

$$E_{\mathrm{XC}}^{\mathrm{hybrid}} = a_{\mathrm{X}} E_{\mathrm{X}}^{\mathrm{exact}} + (1 - a_{\mathrm{X}}) E_{\mathrm{X}}^{\mathrm{GGA}} + E_{\mathrm{C}}^{\mathrm{GGA}}, \tag{2.14}$$

where a_{X} is an exact-exchange mixing percentage which ranges from 0 to 100% (typically a_{X} lies between 20% and 50%); $E_{\mathrm{X}}^{\mathrm{GGA}}$ and $E_{\mathrm{C}}^{\mathrm{GGA}}$ are the exchange and correlation parts from the E_{XC} of the base GGA functional, respectively. The hybrid functionals improve significantly upon GGAs especially in modeling the thermochemistry of molecular systems, leading to a literal explosion of applications of computational chemistry since Becke's seminal work in 1993.[90] The most famed of all hybrid functionals, B3LYP, features 20% of HF exchange mixed with B88 exchange[108] and Lee-Yang-Parr (LYP) correlation,[114] with three semi-empirical parameters from Ref. 90.

2.2 Time-Dependent Density-Functional Theory

The time-dependent (TD) variant of DFT, namely TDDFT, was invented two decades after the groundbreaking works of Hohenberg, Kohn, and Sham for ground-state systems for treating processes involving electronic excitations. TDDFT has since become the most popular theoretical tool for modeling excited-state properties in systems of chemical interest.

2.2.1 The Runge-Gross Theorem and Kohn-Sham TDDFT

The formal foundation of TDDFT is the Runge-Gross (RG) theorem.[45] It states that, for a system evolving from a fixed initial state, ψ_0, under a TD external potential, $v_{\mathrm{ext}}(\boldsymbol{r}, t)$, there exists a unique, one-to-one mapping between $v_{\mathrm{ext}}(\boldsymbol{r}, t)$

and the TD electron density $\rho(\boldsymbol{r}, t)$:

$$\psi_0 : v_{\text{ext}}(\boldsymbol{r}, t) \leftrightarrow \rho(\boldsymbol{r}, t). \tag{2.15}$$

In the same spirit as the time-independent case, $v_{\text{ext}}(\boldsymbol{r}, t)$ uniquely defines the TD Hamiltonian for an N-electron system, which determines the solutions of the TD Schrödinger equation. The RG theorem can be regarded as the TD analogy of the ground-state Hohenberg-Kohn (HK) theorem.

In the same RG paper, the TD-KS formalism is also prescribed. It maps the true, interacting N-electron system to a fictitious, non-interacting system under the TD-KS potential $v_{\text{KS}}(\boldsymbol{r}, t)$, which yields the same TD electron density as the interacting system. The non-interacting system is described by a set of one-particle TD-KS equations:

$$\left[-\frac{1}{2}\nabla_i^2 + v_{\text{KS}}(\boldsymbol{r}, t)\right] \phi_i(\boldsymbol{r}, t) = i\frac{\partial \phi_i(\boldsymbol{r}, t)}{\partial t}, \tag{2.16}$$

where $\phi_i(\boldsymbol{r}, t)$ are the set of one-particle TD-KS orbitals of the non-interacting system that recover the TD electron density of the interacting system:

$$\rho(\boldsymbol{r}, t) = \sum_{i=1}^{N} |\phi_i(\boldsymbol{r}, t)|^2. \tag{2.17}$$

The RG theorem equally applies to the non-interacting KS system, by which we can state that the non-interacting TD-KS potential is a unique functional of both the initial state and the electron density. It can be written as $v_{KS}[\rho, \Phi_0](\boldsymbol{r}, t)$, which can be partitioned as:

$$v_{\text{KS}}[\rho, \Phi_0](\boldsymbol{r}, t) = v_{\text{ext}}(\boldsymbol{r}, t) + \int d\boldsymbol{r'} \frac{\rho(\boldsymbol{r'}, t)}{|\boldsymbol{r} - \boldsymbol{r'}|} + v_{\text{XC}}[\rho, \Phi_0, \psi_0](\boldsymbol{r}, t). \tag{2.18}$$

The second term on the right is the classical Hartree potential. The final term, $v_{\text{XC}}[\rho, \Phi_0, \psi_0](\boldsymbol{r}, t)$, is the exchange-correlation potential, where Φ_0 and ψ_0 are respectively the initial KS and real states. In its original formulation, v_{XC} is dependent on the entire history of the density and the initial states of both the KS and the interacting systems. The TD version of v_{XC} is much more complex than its ground-state counterpart. Thus, in practice, $v_{\text{XC}}(\boldsymbol{r}, t)$ is the subject of significant

simplification and approximation.

2.2.2 Linear-Response TDDFT

At present, the vast majority of TDDFT implementations are in the form of linear-response TDDFT (LR-TDDFT). This approach is used to extract the excitation frequencies and the oscillator strengths (whose magnitudes are proportional to the intensity of their corresponding excitations) in the optical absorption spectra. The use of LR-TDDFT is so predominant that for many it has become synonymous with TDDFT. LR-TDDFT treats the time evolution of the system as a small perturbation to the ground-state: $\delta v_{ext}(\boldsymbol{r}, t)$. The density response to $\delta v_{\text{ext}}(\boldsymbol{r}, t)$ can then be expressed in a power series:

$$\rho(\boldsymbol{r}, t) = \rho_0(\boldsymbol{r}) + \delta\rho(\boldsymbol{r}, t) + ..., \quad t > t_0, \tag{2.19}$$

where $\rho_0(\boldsymbol{r})$ is the initial ground-state density. LR-TDDFT truncates eq. 2.19 to the first-order (linear) term, i.e. $\rho(\boldsymbol{r}, t) = \rho_0(\boldsymbol{r}) + \delta\rho(\boldsymbol{r}, t)$ for $t > t_0$ (t_0 being the initial time of the TD perturbation).

In line with the more general linear response theory of the ground state to a weak external optical field (say an incoming long-wavelength photon along the z-direction), $\delta v_{ext} = -Ae^{i\omega t}\boldsymbol{z}$, we have the linear density response:

$$\delta\rho(\boldsymbol{r}, t) = \iint dt' d\boldsymbol{r'} \chi(\boldsymbol{r}, \boldsymbol{r'}; t - t') \delta v_{\text{ext}}(\boldsymbol{r'}, t'). \tag{2.20}$$

Similarly, for the non-interacting KS system:

$$\delta\rho(\boldsymbol{r}, t) = \iint dt' d\boldsymbol{r'} \chi_{KS}(\boldsymbol{r}, \boldsymbol{r'}; t - t') \delta v_{\text{KS}}(\boldsymbol{r'}, t'), \tag{2.21}$$

where $\chi(\boldsymbol{r}, \boldsymbol{r'}; t - t')$ and $\chi_{\text{KS}}(\boldsymbol{r}, \boldsymbol{r'}; t - t')$ are the response functions for the true and KS systems, respectively.

Starting from the first-order TD perturbation theory, one arrives at an expression for the Fourier transform of χ_{KS} in the frequency domain:[115]

$$\chi_{\text{KS}}(\boldsymbol{r}, \boldsymbol{r'}; \omega) = \lim_{\lambda \to +0} \sum_{k=1}^{N} \sum_{j=N+1}^{\infty} \left[\frac{\phi_j(\boldsymbol{r})\phi_k(\boldsymbol{r})\phi_j(\boldsymbol{r'})\phi_k(\boldsymbol{r'})}{\omega - (\omega_j - \omega_k) + i\lambda} - \frac{\phi_k(\boldsymbol{r})\phi_j(\boldsymbol{r})\phi_k(\boldsymbol{r'})\phi_j(\boldsymbol{r'})}{\omega + (\omega_j - \omega_k) + i\lambda} \right], \tag{2.22}$$

where ϕ_k and ϕ_j are the occupied KS orbital k and the unoccupied KS orbital j, respectively, and $\omega_j - \omega_k$ is the transition frequency between ϕ_k and ϕ_j. In eq. 2.22, λ is a convergence factor which approaches 0 from the positive side, and ω is the frequency variable. Note that all KS orbitals involved come from the self-consistent ground-state DFT calculation. It is thus obvious that the KS linear response function is essentially a sum over single excitations. The KS linear response function is connected to its fully-interacting counterpart via:[46]

$$\begin{aligned}\chi(\boldsymbol{r},\boldsymbol{r'};\omega) = \chi_{\mathrm{KS}}(\boldsymbol{r},\boldsymbol{r'};\omega) + \iint d\boldsymbol{r}_1 d\boldsymbol{r}_2 \chi_{\mathrm{KS}}(\boldsymbol{r},\boldsymbol{r}_1;\omega) \\ \times \left[\frac{1}{|\boldsymbol{r}_1 - \boldsymbol{r}_2|} + f_{\mathrm{XC}}[\rho_0](\boldsymbol{r}_1,\boldsymbol{r}_2,\omega)\right] \chi(\boldsymbol{r}_2,\boldsymbol{r'};\omega),\end{aligned} \tag{2.23}$$

where the f_{XC} term is the Fourier transform of the TD exchange-correlation kernel. This is defined as the functional derivative of the TD exchange-correlation potential, which is in turn the functional derivative of the TD exchange-correlation energy, evaluated at the initial ground-state density:

$$f_{\mathrm{XC}}[\rho_0](\boldsymbol{r},\boldsymbol{r'};t-t') = \frac{\delta v_{\mathrm{XC}}[\rho](\boldsymbol{r},t)}{\delta\rho(\boldsymbol{r'},t')}\Big|_{\rho(\boldsymbol{r'},t')=\rho_0} = \frac{\delta^2 E_{\mathrm{XC}}[\rho](\boldsymbol{r},t)}{\delta\rho(\boldsymbol{r},t)\delta\rho(\boldsymbol{r'},t')}\Big|_{\rho(\boldsymbol{r'},t')=\rho_0}. \tag{2.24}$$

The exchange-correlation kernel is central to LR-TDDFT: its approximation needs to capture the dynamic, many-electron effects ignored in the KS system. It acts to mix the bare KS single excitations, whose frequencies are at the poles of eq. 2.22, to recover the true excitation frequencies of the interacting system.[116]

The simplest option for an approximation to f_{XC} is to directly use a ground-state exchange-correlation functional. This is called the adiabatic approximation (AA):

$$v_{\mathrm{XC}}^{\mathrm{AA}}[\rho](\boldsymbol{r},t) = v_{\mathrm{XC}}^{\mathrm{GS}}[\rho(t)](\boldsymbol{r}), \tag{2.25}$$

where the instantaneous electron density at t is plugged in the ground-state DFT exchange-correlation functional. Note that $f_{\mathrm{XC}}^{\mathrm{AA}}$ only relies on the instantaneous time-dependent density $\rho(t)$, which causes χ^{AA} (the response function under the AA) to have neither frequency nor initial-state dependence. The AA is by far the most predominant approximation to f_{XC} in LR-TDDFT.

In most LR-TDDFT implementations, the extraction of excitation energies and

oscillator strengths is done through casting eq. 2.23 into a set of non-Hermitian matrix equations, called the Casida equations.[117] This set of equations can be expressed in the form of a (pseudo) eigenvalue problem:

$$\boldsymbol{\Omega}(\omega)\boldsymbol{F} = \omega^2\boldsymbol{F}, \tag{2.26}$$

where $\boldsymbol{F}$ is the eigenvector of the frequency-dependent matrix $\boldsymbol{\Omega}(\omega)$. The elements of the $\boldsymbol{\Omega}(\omega)$ matrix are:

$$\Omega_{qq'}(\omega) = \delta_{qq'}\omega_q^2 + 4\sqrt{\omega_q\omega_{q'}} \iint d\boldsymbol{r}d\boldsymbol{r'}\phi_i(\boldsymbol{r})\phi_a(\boldsymbol{r}) \left[\frac{1}{|\boldsymbol{r}-\boldsymbol{r'}|} + f_{\mathrm{XC}}(\boldsymbol{r},\boldsymbol{r'},\omega)\right] \phi_j(\boldsymbol{r'})\phi_b(\boldsymbol{r'}) \tag{2.27}$$

where $\delta_{qq'}$ is the Kronecker delta. Here we have introduced the double index $q = (i,a)$, or $q' = (j,b)$, which indicates a single excitation from the occupied KS orbitals, ϕ_i or ϕ_j, to the unoccupied (virtual) orbitals, ϕ_a or ϕ_b. ω_q is the corresponding KS transition frequency.

Solving eq. 2.26, the resulting eigenvalues ω are the true transition frequencies of the interacting system. The oscillator strengths of these transitions are obtained by a subsequent matrix operation on their corresponding eigenvectors $\boldsymbol{F}$.[117] Eq. 2.26 is often reformulated as[118]

$$\begin{bmatrix} \boldsymbol{A} & \boldsymbol{B} \\ \boldsymbol{B} & \boldsymbol{A} \end{bmatrix} \begin{bmatrix} \boldsymbol{X} \\ \boldsymbol{Y} \end{bmatrix} = \omega \begin{bmatrix} -1 & 0 \\ 0 & 1 \end{bmatrix} \begin{bmatrix} \boldsymbol{X} \\ \boldsymbol{Y} \end{bmatrix}, \tag{2.28}$$

where the respective elements of $\boldsymbol{A}$ and $\boldsymbol{B}$ are

$$A_{qq'} = \delta_{ij}\delta_{ab}\omega_q + 2\iint d\boldsymbol{r}d\boldsymbol{r'}\phi_i(\boldsymbol{r})\phi_a(\boldsymbol{r}) \left[\frac{1}{|\boldsymbol{r}-\boldsymbol{r'}|} + f_{\mathrm{XC}}(\boldsymbol{r},\boldsymbol{r'},\omega)\right] \phi_j(\boldsymbol{r'})\phi_b(\boldsymbol{r'}), \tag{2.29}$$

$$B_{qq'} = 2\iint d\boldsymbol{r}d\boldsymbol{r'}\phi_i(\boldsymbol{r})\phi_a(\boldsymbol{r}) \left[\frac{1}{|\boldsymbol{r}-\boldsymbol{r'}|} + f_{\mathrm{XC}}(\boldsymbol{r},\boldsymbol{r'},\omega)\right] \phi_b(\boldsymbol{r'})\phi_j(\boldsymbol{r'}). \tag{2.30}$$

The elements $X_q(\omega)$ and $Y_q(\omega)$ of the resulting eigenvector $[\boldsymbol{X}\ \boldsymbol{Y}]^T$ are used to construct the linear electron-density response:[118]

$$\delta\rho(\boldsymbol{r},\omega) = \sum_q \left[X_q(\omega)\phi_a(\boldsymbol{r})\phi_i(\boldsymbol{r}) + Y_q(\omega)\phi_b(\boldsymbol{r})\phi_j(\boldsymbol{r})\right]. \tag{2.31}$$

To summarize, when applying the LR-TDDFT scheme, one starts by running a self-consistent ground-state DFT calculation to obtain the ground-state KS orbitals (with some usual approximation to the exchange-correlation potential), including the virtual orbitals. These ground-state KS orbitals are then used to construct the density response by solving the Casida equations, where bare KS single excitations are mixed by the exchange-correlation kernel approximated by the AA to produce the "true" excitation energies and oscillator strengths. It is thus evident that LR-TDDFT, in its most popularly implemented form, is solely dependent on the KS orbitals calculated for the ground state. Indeed such a formalism is only "pseudo-time-dependent", albeit the time dependence is necessary for the derivations leading towards its working equations.

Although LR-TDDFT often provides impressively accurate estimations to the excitation energies and excited-state densities, its limitations are equally notable. Via the AA, LR-TDDFT inherits any potential errors from the ground-state exchange-correlation functionals, such as the significant underestimation of charge-transfer (CT) excitation energies and the incorrect asymptotic behavior thereof, i.e. the CT excitation energies erroneously converge to some underestimated values when the CT distance is infinitely stretched. The CT problem of LR-TDDFT is especially frustrating since CT excitations are among the most common types of electronic processes in organic chromophores, and their relative energy orderings with respect to other localized valence excitations greatly influence the interpretation of the electronic processes in those systems.

Between 2003 and 2004, Head-Gordon *et al.*[95,119] explicitly demonstrated the problem in CT systems ranging from the simple C_2H_4-C_2F_4 dimer to photosynthetic porphyrin complexes. They concluded[119] that the underestimation of the CT-excitation energy is due to the localized nature of the approximate exchange-correlation potential used in TDDFT. In CT excitations, the non-local exchange contributions to the excitation energy (the f_{XC} terms in eqs. 2.29 and 2.30) become important as the overlap between the faraway electron-donating and electron-accepting orbitals vanishes. The DFT exchange potential behaves incorrectly at large CT distances, falling off too rapidly and causing the non-local contribution to the CT excitation energy to vanish (recall eqs. 2.24, 2.29 and 2.30). This reduces

the TDDFT estimation of the CT excitation energy to the energy difference between the bare KS orbitals, which is much too low (frequently by 1 to 2 eV) and levels off at some fixed value as the separation between the electron-donating and electron-accepting orbitals tends to infinity.

Tozer *et al.*[97] later established that range-separated hybrid (RSH) functionals (such as CAM-B3LYP[120]) with varying degrees of Hartree-Fock exchange-mixing at short and long ranges significantly alleviate the CT excitation problem of TDDFT. They also proposed a diagnostic Λ-index to quantify the CT character of excitations, which can be used as an indicator of the reliability of TDDFT results.

2.3 Becke's Virial Exciton Model

From 2016 to 2018, Becke introduced a novel scheme,[99,100] named the Virial Exciton Model, to calculate the first singlet excitation energy (E_{0S}) in molecular systems using ground-state KS-DFT. This simple approach has been shown to yield values of E_{0S} on par with, or more accurate than, the popular LR-TDDFT method when compared to theoretical benchmark or experimental data. E_{0S} is of primary interest in the luminescence spectra of organic chromophores, yet reliable calculation of E_{0S} is difficult to achieve via ground-state methods due to the multi-determinant nature of the singlet excited state. Before going into the details of the virial exciton model, the multi-determinant problem of singlet excitations is presented.

A single-electron excitation from the initial closed-shell ground-state orbital ψ_i to the excited-state orbital ψ_f can be categorized into one of two situations according to the total spin of the resultant excited states: a singlet excited state ($S = 0$), or a triplet excited state ($S = 1$). The orbital configuration for the singlet excited state can be expressed as

$$\Psi_{\mathrm{S}} = \frac{1}{\sqrt{2}}\{|\alpha\beta\rangle - |\beta\alpha\rangle\}, \tag{2.32}$$

where α and β denote up spin and down spin, respectively. For the triplet excitation, there are three degenerate configurations:

$$\Psi_{\mathrm{T}}^{m=+1} = |\alpha\alpha\rangle, \tag{2.33a}$$

$$\Psi_{\mathrm{T}}^{m=0} = \frac{1}{\sqrt{2}}\{|\alpha\beta\rangle + |\beta\alpha\rangle\}, \tag{2.33b}$$

$$\Psi_{\mathrm{T}}^{m=-1} = |\beta\beta\rangle, \tag{2.33c}$$

where m is the total spin angular momentum.

Conventional KS-DFT is, by design, a strictly single-determinant method. While not suitable to describe the general case of electronic excitations that involve multi-determinantal states, conventional KS-DFT is capable of calculating the energies of excited states where a single determinant suffices. For the triplet state, one can calculate its energy, E_{T}, from either one of the two single-determinants, $|\alpha\alpha\rangle$ or $|\beta\beta\rangle$, since

$$E_{\mathrm{T}} = E_{\mathrm{T}}^{\alpha\alpha} = E_{\mathrm{T}}^{\beta\beta} = E_{\mathrm{T}}^{\alpha\beta+\beta\alpha}. \tag{2.34}$$

It is evident, however, that direct calculation of the singlet-excited-state energy E_{S} is problematic since one cannot circumvent the double-determinant state. If we ignore the Coulombic correlation between the electrons (i.e. if we reduce the system to its non-interacting KS picture), we can conceive an *un*correlated, double-determinant approximation to E_{S}. This approximation arises from the non-interacting limit of the so-called "adiabatic connection"[121–123] concept, which is fundamental to KS-DFT. In the non-interacting (KS) limit, the gap between E_{S} and E_{T} is simply the difference in the exchange energy between the singlet and triplet excited states (assuming that their spatial orbitals are the same), which can be expressed in terms of the pair-density difference,[99,100] $\Delta\Pi_{\mathrm{KS}}(\boldsymbol{r}_1, \boldsymbol{r}_2)$, between said states:

$$E_{\mathrm{S}} - E_{\mathrm{T}} = \frac{1}{2}\int\int d^3r_1 d^3r_2 \frac{\Delta\Pi_{\mathrm{KS}}(\boldsymbol{r}_1, \boldsymbol{r}_2)}{r_{12}}, \tag{2.35}$$

with

$$\Delta\Pi_{\mathrm{KS}}(\boldsymbol{r}_1, \boldsymbol{r}_2) = 4\phi_i(\boldsymbol{r}_1)\phi_f(\boldsymbol{r}_1)\phi_i(\boldsymbol{r}_2)\phi_f(\boldsymbol{r}_2), \tag{2.36}$$

where ϕ_i and ϕ_f are the initial and final orbitals involved in the transition. Substituting eq. 2.36 into eq. 2.35, we obtain

$$E_{\mathrm{S}} - E_{\mathrm{T}} = 2\iint d\boldsymbol{r}_1 d\boldsymbol{r}_2 \frac{\phi_i(\boldsymbol{r}_1)\phi_f(\boldsymbol{r}_1)\phi_i(\boldsymbol{r}_2)\phi_f(\boldsymbol{r}_2)}{r_{12}}. \tag{2.37}$$

Now, we define the two-electron integral, H_{12}:

$$H_{12} = \iint d\boldsymbol{r}_1 d\boldsymbol{r}_2 \frac{\phi_i(\boldsymbol{r}_1)\phi_f(\boldsymbol{r}_1)\phi_i(\boldsymbol{r}_2)\phi_f(\boldsymbol{r}_2)}{r_{12}}, \tag{2.38}$$

such that

$$E_{\mathrm{S}} - E_{\mathrm{T}} = 2H_{12}. \tag{2.39}$$

The quantity $2H_{12}$ is the uncorrelated first singlet-triplet energy splitting.[99] We reiterate that it is the exchange-energy difference between the singlet and triplet excited states, and thus it is the exact singlet-triplet energy splitting in the KS limit.

However, eq. 2.39 is a poor approximation to the actual correlated singlet-triplet energy splitting, massively overestimating E_{S} by more than 1 eV on average[99] compared to correlated-wavefunction benchmark data for excitations of 28 gas-phase organic molecules compiled by Thiel *et al.*[124] In order to obtain a better approximation, we must add a correction term, E^{corr}, to $2H_{12}$ to include the correlation-energy contribution to the singlet-triplet splitting, which is ignored in the KS limit:

$$E_{\mathrm{S}} - E_{\mathrm{T}} = 2H_{12} + E^{\mathrm{corr}}. \tag{2.40}$$

In Ref. 100, Becke approached the E^{corr} term via the virial theorem,[125] which states that, for an exact stationary state of a molecular system at equilibrium geometry, its kinetic (T) and potential (V) energies have the following simple relation:

$$2T = -V. \tag{2.41}$$

The virial theorem is valid for both ground and excited states, and equally applies to both the correlated and uncorrelated (KS) systems. Therefore, we can trivially derive the relation between the kinetic and potential parts of E^{corr}:[100]

$$2T^{\mathrm{corr}} = -V^{\mathrm{corr}}. \tag{2.42}$$

From this, we can express E^{corr} solely in terms of the potential-energy correction for correlation:

$$E^{\mathrm{corr}} = T^{\mathrm{corr}} + V^{\mathrm{corr}} = \frac{1}{2}V^{\mathrm{corr}}. \tag{2.43}$$

Based on physical intuition, Becke argued that the potential caused by electron-electron correlation would significantly lower $2H_{12}$ by "smoothing out"[100] the singlet-triplet pair-density difference (eq. 2.36). The simplest approximation is to reduce it to 0 everywhere.[100] The potential-energy correction would then completely cancel out $2H_{12}$:

$$V^{\text{corr}} = -2H_{12}. \tag{2.44}$$

Applying the virial-theorem result of eq. 2.43 with the potential-energy correction of eq. 2.44, the total correlation-energy correction is obtained:

$$E^{\text{corr}} = \frac{1}{2}V^{\text{corr}} = -H_{12}, \tag{2.45}$$

which leads to Becke's correlation-corrected singlet-triplet energy splitting:

$$E_{\text{S}} - E_{\text{T}} = H_{12}, \tag{2.46}$$

with H_{12} defined by eq. 2.38.

Becke's virial-theorem correction scheme was tested against the aforementioned 28-molecule theoretical benchmark set,[124] as well as experimental data for linear acenes and non-linear polycyclic aromatic hydrocarbons (PAHs), while comparisons were made with the TDDFT results. Becke's model achieves remarkable accuracy for Thiel's 28-molecule set, with the mean absolute error (MAE) of 0.26 eV being on par with the TD-B3LYP MAE of 0.24 eV. Additionally, Becke's model significantly out-performs TD-B3LYP for the singlet excitation energies of the linear acenes and nonlinear PAHs, achieving MAEs of 0.10 eV and 0.14 eV, respectively, compared to MAEs of 0.43 eV and 0.27 eV obtained with TD-B3LYP.

2.4 Periodic-Boundary DFT

2.4.1 The Planewave Basis

Theoretical modeling of solid-state materials is in many ways distinct from that of gas-phase molecules. Currently, the hierarchy of post-Hartree-Fock wavefunction-based methods (MP2, coupled-cluster methods, configuration interaction, etc.) cannot be applied practically to periodic systems using planewave basis sets, while

(ground-state) DFT can be routinely employed in solid-state calculations. In particular, the use of the planewave-pseudopotential (PW-PS) formalism of periodic-boundary DFT has become a standard practice for theoretical calculations in solid-state physics and material sciences.

The exploitation of periodicity is crucial in the application of electronic-structure methods to solid-state calculations. An ideal crystalline solid consists of identical structural units, called unit cells, which are (nearly) infinitely repeated throughout the material. The periodicity is very convenient because it allows one to have knowledge of the entire (infinitely extending) crystal structure by merely studying the properties of a finite unit cell. In the language of quantum mechanics, if one knows the wavefunction (or the electron density) of a unit cell, it can be replicated via the translational symmetry along every dimension of the unit cell. The Bravais lattice vector is the unit of spacial periodicity:

$$\boldsymbol{R} = \sum_{i=1}^{3} n_i \boldsymbol{a}_i, \tag{2.47}$$

where $\boldsymbol{a}_i$ are the set of three real-space vectors representing the dimensions of the unit cell and n_i can take any integer values. Translation along $\boldsymbol{R}$ from any point $\boldsymbol{r}$ within the unit cell results in an identical potential:

$$V(\boldsymbol{r} + \boldsymbol{R}) = V(\boldsymbol{r}). \tag{2.48}$$

The periodicity of V gives rise to Bloch's theorem.[126] Under the enforcement of the periodic-boundary condition that $\psi(\boldsymbol{r}) = \psi(\boldsymbol{r} + N\boldsymbol{R})$ for some very large integer N (on the level of the Avogadro's number), Bloch's theorem stipulates a planewave form of the electronic wavefunction under a periodic potential:

$$\psi_{\boldsymbol{k}n}(\boldsymbol{r}) = \frac{1}{\sqrt{\Omega}} u_{\boldsymbol{k}n}(\boldsymbol{r}) e^{i\boldsymbol{k}\cdot\boldsymbol{r}}, \tag{2.49}$$

where Ω is the volume of the unit cell: $\Omega = \boldsymbol{a_1} \cdot (\boldsymbol{a_2} \times \boldsymbol{a_3})$. $u_{\boldsymbol{k}n}(\boldsymbol{r})$ is a spatially-dependent component of the wavefunction for the nth energy band, which has the

same periodicity as the real-space lattice:

$$u_{\boldsymbol{k}n}(\boldsymbol{r}+\boldsymbol{R}) = u_{\boldsymbol{k}n}(\boldsymbol{r}). \tag{2.50}$$

We have also introduced the wave vector $\boldsymbol{k}$:

$$\boldsymbol{k} = \sum_{i=1}^{3} k_i \boldsymbol{b}_i, \tag{2.51}$$

where the reciprocal lattice vectors $\boldsymbol{b}_i$ are defined by their reciprocal relationship with the real-space lattice vectors $\boldsymbol{a}_j$:

$$\boldsymbol{a}_j \cdot \boldsymbol{b}_i = 2\pi\delta_{ij}. \tag{2.52}$$

Further, $u_{\boldsymbol{k}n}$ can itself be expanded in planewaves:

$$u_{\boldsymbol{k}n} = \sum_{\boldsymbol{G}} c_{\boldsymbol{k}n}(\boldsymbol{G}) e^{i\boldsymbol{G}\cdot\boldsymbol{r}}, \tag{2.53}$$

in which $c_{\boldsymbol{k}n}(\boldsymbol{G})$ are the planewave expansion coefficients, and

$$\boldsymbol{G} = \sum_{i=1}^{3} g_i \boldsymbol{b}_i, \tag{2.54}$$

where g_i must take on integer values due to the periodicity of $u_{\boldsymbol{k}n}$ (eq. 2.50). In comparison, in the expansion of $\boldsymbol{k}$ within eq. 2.51, the coefficients k_i can take on integer as well as fractional values. Substituting eq. 2.53 into eq. 2.49, we obtain the nth band wavefunction at wave vector $\boldsymbol{k}$, in the fully-expanded planewave basis set:

$$\psi_{\boldsymbol{k}n}(\boldsymbol{r}) = \frac{1}{\sqrt{\Omega}} \sum_{\boldsymbol{G}} c_{\boldsymbol{k}n}(\boldsymbol{G}) e^{i(\boldsymbol{k}+\boldsymbol{G})\cdot\boldsymbol{r}}. \tag{2.55}$$

Eq. 2.55 is essentially a Fourier expansion of the real-space wavefunction in terms of its components in the so-called "reciprocal space", i.e. momentum space. The wave vector $\boldsymbol{k}$ represents the kinetic energy of its associated planewave component

via $E_{\boldsymbol{k}} = \frac{1}{2}|\boldsymbol{k}|^2$. Eq. 2.55 has the following property:

$$\psi_{\boldsymbol{k}n}(\boldsymbol{r} + \boldsymbol{R}) = \psi_{\boldsymbol{k}n}(\boldsymbol{r})e^{i\boldsymbol{k}\cdot\boldsymbol{R}}, \tag{2.56}$$

which leads to:

$$|\psi_n(\boldsymbol{r} + \boldsymbol{R})|^2 = |\psi_n(\boldsymbol{r})|^2 \cdot |e^{i\boldsymbol{k}\cdot\boldsymbol{R}}|^2 = |\psi_n(\boldsymbol{r})|^2, \tag{2.57}$$

which is guaranteed by $|e^{i\boldsymbol{k}\cdot\boldsymbol{R}}|^2 = 1$, for all k and R. Eq. 2.57 implies that the electronic density of a planewave wavefunction observes the same periodicity as the real-space lattice.

The planewave basis of the periodic wavefunction is inherently orthogonal and complete as the summation over all allowable $\boldsymbol{k}$ approaches infinity. In practice, an upper limit to the momentum-space component summation is set to obtain a finite number of planewave basis functions: $\frac{1}{2}|\boldsymbol{k}|^2 < E_{\text{cut,wfn}}$, where $E_{\text{cut,wfn}}$ is the wavefunction kinetic-energy cutoff. Such a truncation is valid for a physical system where momentum-space components with higher kinetic energy become progressively insignificant. The electron density can likewise be expressed as a Fourier-series expansion:

$$\rho(\boldsymbol{r}) = \sum_n \psi_n^*(\boldsymbol{r})\psi_n(\boldsymbol{r}) = \sum_{\boldsymbol{k}} \tilde{\rho}(\boldsymbol{k})e^{i\boldsymbol{k}\boldsymbol{r}}. \tag{2.58}$$

Different from eq. 2.49, in eq. 2.58 components of $\boldsymbol{k}$ are restricted to the multiples of the momentum-space lattice vectors, since $\rho(\boldsymbol{r})$ has the periodicity of the lattice. Truncating eq. 2.58 leads to a cutoff energy with respect to the electron density: $\frac{1}{2}|\boldsymbol{k}|^2 < E_{\text{cut},\rho}$. $E_{\text{cut,wfn}}$ and $E_{\text{cut},\rho}$ are proportional to the number of planewaves, i.e. the size of the planewave basis set. In calculations, higher cutoff values will lead to higher accuracy at the cost of increasing computational time. It is often necessary to gradually increase the cutoff values until the resulting total energy converges under some set threshold. When employing planewave basis sets, one evaluates a certain real-space quantity, be it $\psi_n(\boldsymbol{r})$ or $\rho(\boldsymbol{r})$, by sampling its components in momentum space. This is most often done on a Monkhorst-Pack (MP) style grid[127] consisting of discrete and evenly-spaced grid points in momentum space defined in the basis of $\boldsymbol{b}_i$. A specific MP-style sampling grid (also called $\boldsymbol{k}$-mesh) is denoted by

$k_1 \times k_2 \times k_3$, with each index referring to the number of grid points to be sampled along its corresponding dimension.

2.4.2 Pseudopotentials

Due to their delocalized and sinusoidal nature, planewave basis sets are competent in describing the slowly-varying interstitial potential between the nuclei within the unit cell. However, the potential oscillates rapidly in the regions near the nuclei (see Figure 2.1), where the core electrons typically reside. It would take an excessive number of planewaves to properly capture the core potential. One way to significantly reduce the number of planewaves needed is to replace the wavefunction description of the core electrons with a so-called pseudopotential,[128,129] which maintains the same effective potential felt by the valence electrons. Pseudopotentials are constructed to vary much more smoothly than the actual all-electron (AE) potential in the near-core region of an atom (see Figure 2.2). Beyond a set radius, $\boldsymbol{r}_{\text{cut}}$, from the nucleus, the pseudopotential will behave identically to the AE potential. The use of pseudopotentials is justified by the fact that the core electrons are chemically inert and, in general, have a much less significant effect on the physical properties of the material than its valence electrons. Also, due to the screening effect of the core-electrons, the Coulomb potential beyond the near-core regions (felt mostly by the valence electrons) is indeed much more smoothly-varying.

Figure 2.1: Schematic sketch of the behavior of the electronic wavefunction in a periodic system. Notice the rapid oscillation in the near-core regions within the dashed circles.

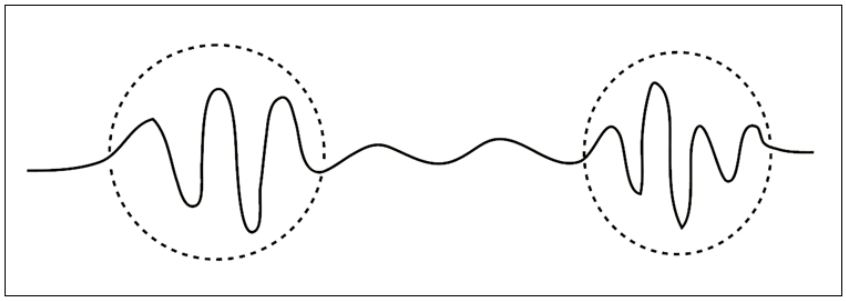

Pseudopotentials are specifically assigned to each element. When used in a planewave DFT calculation, the pseudopotentials are also parametrized using the specific exchange-correlation functional to be employed. While such a pseudopotential approximation works remarkably well in many cases, its validity is

Figure 2.2: Schematic diagram of the pseudopotential approximation. The all-electron potential, V_{AE}, is replaced by the "flattened" pseudopotential, V_{PS}, within the cut-off radius, r_{cut}. As a result, the rapidly oscillating all-electron wavefunction, ψ^{AE}, becomes the smoothed wavefunction, ψ^{PS}, in the near-core regions.

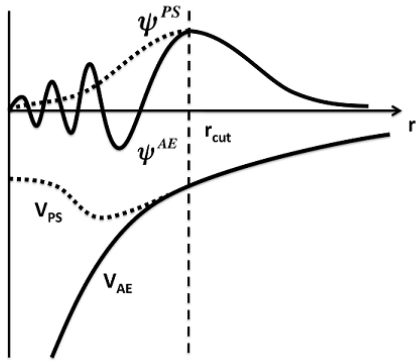

diminished when one wishes to model certain hyperfine properties, such as spin-orbit coupling,[130] where information regarding the full wavefunction in the near-core regions becomes important. Also, one does not have beforehand knowledge of the reliability of the results when using pseudopotentials, which poses the potential issue of transferability.[131]

2.4.3 The Projector Augmented-Wave (PAW) Method

An all-electron approximation that is now frequently used is the projector augmented-wave (PAW) method first proposed by Blöchl in 1994.[132] Methodologically speaking, the PAW method could be viewed as an extension of the previously described pseudopotential approach. The PAW method uses fix-shaped atomic orbitals within the near-core regions to mimic the rapidly-oscillating nature of the core-electron wavefunctions. The all-electron single-particle wavefunction ($|\Psi\rangle$) is mapped to a smoothly-varying pseudo-wavefunction ($|\tilde{\Psi}\rangle$) via a linear transformation ($\mathcal{T}$):

$$|\Psi\rangle = \mathcal{T}|\tilde{\Psi}\rangle. \tag{2.59}$$

Since the pseudo- and all-electron wavefunctions only differ within a certain cut-off radius, r_{cut}, from the atomic nucleus, the transformation operator $\mathcal{T}$ should differ from 1 only within r_{cut} (refer to Figure 2.2).

The overall pseudo-wavefunction can be further expanded into a linear combination of pseudo partial waves:

$$|\tilde{\Psi}\rangle = \sum_i |\tilde{\phi}_i\rangle c_i. \tag{2.60}$$

The index, i, is the quantum state label, which contains a momentum-space wave vector index, a band index, and a spin index.[133] For the coefficients c_i, we define a set of "projector functions", $|p_i\rangle$, such that

$$c_i = \langle p_i|\tilde{\Psi}\rangle, \tag{2.61}$$

where $\langle p_i|\tilde{\phi}_j\rangle = \delta_{ij}$. Subsequently, $\mathcal{T}$ can be explictly written as

$$\mathcal{T} = 1 + \sum_i (|\phi_i\rangle - |\tilde{\phi}_i\rangle)\langle p_i|. \tag{2.62}$$

Note that $|p_i\rangle$ is always taken to be 0 outside of r_{cut}. The transformation is therefore uniquely defined by a set of all-electron partial waves, $|\phi_i\rangle$, and a set of projector functions, $|p_i\rangle$. The all-electron partial waves, $|\phi_i\rangle$, are also mapped to the pseudo partial waves, $|\tilde{\phi}_i\rangle$, via $\mathcal{T}$:

$$|\phi_i\rangle = \mathcal{T}|\tilde{\phi}_i\rangle. \tag{2.63}$$

Importantly, within the PAW cutoff sphere, the transformed pseudo wavefunction necessarily reduces to $|\tilde{\Psi}\rangle$ itself:[133]

$$\sum_i |\tilde{\phi}_i\rangle\langle p_i|\tilde{\Psi}\rangle = |\tilde{\Psi}\rangle, \tag{2.64}$$

which leads to the key result of projector-partial-wave completeness:[133,134]

$$\sum_i |\tilde{\phi}_i\rangle\langle p_i| = 1. \tag{2.65}$$

The pre-computed sets of all-electron atom-like orbitals and projector functions collectively constitute the PAW dataset. Atom-specific PAW datasets are readily available in online repositories[135,136] and can be called when a planewave-PAW calculation is requested.

2.4.4 Spin-Magnetized Calculations

In this work, spin-magnetized/polarized calculations with the Quantum ESPRESSO (QE) program[101] are frequently employed to simulate non-singlet spin states (in particular, the first triplet state, T_1) in periodic solid systems. These calculations require two additional inputs: (i) the specification of a constant total spin-magnetization, which restricts the system to the desired non-singlet spin state, and (ii) the assignment of an initial magnetization bias, which alters the ansatz used as the initial guess for the self-consistent field (SCF) cycles of the calculations.

To indicate that a spin-magnetized calculation is to be conducted, and specify the total spin-magnetization of the system, the QE keywords[137] `nspin` and `tot_magnetization` are used, respectively. We first specify that the system should be spin-magnetized along the z-axis, which is done by using the option `nspin = 2`. Then, the `tot_magnetization` keyword is given a value which equals the total number of majority-spin (α) electrons, minus the number of minority-spin (β) electrons in the system. For a T_1 state, we specify `tot_magnetization = 2`, since there are 2 more α-spin electrons than β-spin electrons in a triplet-state system.

In QE, initial magnetization biases can be assigned to specific individual atoms within the crystal lattice. This is done in order to facilitate SCF convergence to a non-singlet energy minimum, by providing a spin-polarized initial guess electron density. The QE keyword `starting_magnetization(n) = x` is used to assign an initial magnetization bias to the nth atom type in the input's list of atoms. The x value gives the magnitude of the bias, which can range from -1 (all electrons are β-spin) to 1 (all electrons are α-spin). The solid-state spin-polarized calculation itself resembles an unrestricted Hartree-Fock (UHF) calculation[138] on a molecule, in which the Kohn-Sham equations are solved for the α- and β-spin orbitals independently.

2.4.5 Applied Pressure

In QE, an external pressure can be specified in a variable-cell (i.e. "full") optimization of the crystalline geometry, using the `press` keyword. This is done in order to optimize the crystalline geometry under a specific external pressure. While a crystal's response to an external pressure can be quite complex, the QE `press` keyword operates on a rather simple principle: at constant external pressure, the

equilibrium geometry of a crystal is found when the enthalpy (H^{cryst}) is minimized, instead of the electronic energy (E^{cryst}). The enthalpy of the crystal is:

$$H^{\text{cryst}} = E^{\text{cryst}} + pV, \tag{2.66}$$

where p is the applied external pressure and V is the volume of the crystal lattice. It is evident that, in order to minimize H^{cryst}, there is an incentive for the crystal lattice to shrink under high external pressures and expand under negative external pressure (as results from the lattice vibrations). The `press` keyword simply adds an extra pV constraint to the variable-cell geometry optimization, compared to a regular, unconstrained optimization without any applied external pressure. The crystal geometry obtained under such a constraint is thus the optimized geometry subject to the specified external pressure.

2.4.6 Crystalline Band Structure

The QE package employs a multi-step procedure to calculate the band structure of a crystal. Initially, a simple single-point SCF calculation is performed on the geometry-optimized crystal, which generates a set of Kohn-Sham orbitals (in the momentum space) for the crystal. These Kohn-Sham orbitals include all occupied, and a number of unoccupied, orbitals. This set of Kohn-Sham orbitals is then used as input to a second, non-SCF calculation (via the `calculation = bands` keyword) to obtain the electronic energy states (i.e. bands), spanning the crystal's valence band and including a certain number of states within the conduction band (assuming an insulator). The total number of bands to be calculated is specified using the `nbnd` keyword.

In addition, a "path" of wave vectors is specified for this non-SCF calculation for the momentum-space sampling of the calculated states. To achieve efficient momentum-space sampling, the specified path generally starts from the $\mathbf{\Gamma}$ point, with wave vector $\boldsymbol{k} = (0, 0, 0)$. It then passes through a number of high-symmetry points (denoted by letters such as W, X, L, Z, etc.) within the first Brillouin zone,[87] and finally loops back to the $\mathbf{\Gamma}$ point. Figure 2.3 gives an illustrative example of such a path selection. Along this **k**-path, a specified number of points are sampled between each two adjacent high-symmetry points. The band energies

Figure 2.3: The first Brillouin zone of a face-centered cubic (FCC) crystal, showing possible paths connecting its major high-symmetry points. Drawing taken from Ref. 141. Image reused with permission from Setyawan *et al.*, Comput. Mater. Sci. **49**, 299-312 (2010). Copyright 2010 Elsevier.

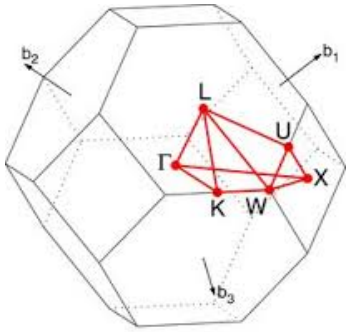

(i.e. the eigenvalues) are obtained via a single iteration of diagonalization of the Fock matrix,[139] which is constructed from the previously acquired SCF Kohn-Sham orbitals. This Fock-matrix diagonalization is done at each sampled point in the momentum space until the specified **k**-path is completed.[140]

Finally, a third calculation is performed to extract the crystal band structure from the wavefunction outputs of the previous non-SCF calculation, using the `bands.x` program within the QE package. The end result is a list of electronic-state energies with respect to the wave vector, from which the crystal band diagram and the valence-conduction band gap can be easily obtained.

2.5 The XDM Dispersion Model

It is well-known that conventional exchange-correlation density functionals, such as the local density approximation (LDA) and generalized-gradient approximations (GGAs), are incapable of properly describing London dispersion interactions.[142,143] This is due to the "near-sightedness" of these density functionals, which only consider the local electron density (for LDA) or, in addition, the density gradients near the vicinity of a reference point (for GGAs). The lack of long-range dispersion interactions severely limits the use of these conventional functionals in modeling weakly-bound systems,[144–146] or in deciding the preferred crystal polymorphs when many close energetic competitors are present.[147,148]

The exchange-hole dipole moment (XDM) model is a semi-classical dispersion

correction developed by Becke and Johnson starting in 2005, with the final version of the equations formulated in 2007.[102,103] The XDM model belongs to the category of *a posteriori* dispersion-correction methods, which calculate an additive dispersion energy term to obtain the dispersion-corrected DFT energy:

$$E = E_{\mathrm{DFT}} + E_{\mathrm{disp}}. \tag{2.67}$$

The central idea behind XDM is to consider the interaction between the exchange-hole dipole moments in atoms as the origin of the London dispersion interactions. XDM borrows from the concept of interacting instantaneous dipole moments in the classical theory of London dispersion, although in XDM such dipole moments arise from the purely quantum-mechanical phenomenon of Pauli exclusion between the same-spin electrons in atoms.

The exchange hole, $h_{X\sigma}(\boldsymbol{r}_1, \boldsymbol{r}_2)$, measures the depletion of the probability density of finding a same-spin electron 2 in the space around a reference σ-spin electron 1:

$$h_{X\sigma}(\boldsymbol{r}_1, \boldsymbol{r}_2) = -\frac{1}{\rho_\sigma(\boldsymbol{r}_1)} \sum_{ij} \psi_{i\sigma}(\boldsymbol{r}_1)\psi_{j\sigma}(\boldsymbol{r}_1)\psi_{i\sigma}(\boldsymbol{r}_2)\psi_{j\sigma}(\boldsymbol{r}_2), \tag{2.68}$$

where $\boldsymbol{r}_1$ and $\boldsymbol{r}_2$ are the respective position vectors of the electrons and $\rho_\sigma(\boldsymbol{r}_1)$ is the σ-spin density at $\boldsymbol{r}_1$. The summation runs over all occupied σ-spin Hartree-Fock or Kohn-Sham orbitals, $\psi_{i\sigma}$. The exchange hole completely eliminates the probability density of the σ-spin electron 2 at the reference point (i.e. the position of the reference electron 1):

$$h_{X\sigma}(\boldsymbol{r}_1, \boldsymbol{r}_1) = -\rho_\sigma(\boldsymbol{r}_1), \tag{2.69}$$

which is in agreement with the Pauli exclusion principle stating that it is impossible to find two same-spin electrons occupying the same point in space. The exchange hole is normalized to -1 electron (i.e. $+1$ charge) when integrated over all space:

$$\int d\boldsymbol{r}_2 h_{X\sigma}(\boldsymbol{r}_1, \boldsymbol{r}_2) = -1. \tag{2.70}$$

In general, the exchange hole is not spherically symmetric. This gives rise to

an exchange-hole dipole moment between the negatively-charged electron and its corresponding exchange hole, which can be considered positively charged. The exchange-hole dipole moment is expressed as

$$\boldsymbol{d}_{X\sigma}(\boldsymbol{r}_1) = \left[\frac{1}{\rho_\sigma(\boldsymbol{r}_1)}\sum_{ij}\psi_{i\sigma}(\boldsymbol{r}_1)\psi_{j\sigma}(\boldsymbol{r}_1)\int d\boldsymbol{r}_2\boldsymbol{r}\psi_{i\sigma}(\boldsymbol{r}_2)\psi_{j\sigma}(\boldsymbol{r}_2)\right] - \boldsymbol{r}_1. \tag{2.71}$$

The expectation value of the square of the exchange-hole dipole moment is:

$$\langle d_X^2\rangle = \sum_\sigma \int d\boldsymbol{r}\rho_\sigma(\boldsymbol{r})\boldsymbol{d}_{X\sigma}^2(\boldsymbol{r}). \tag{2.72}$$

Based on $d_{X\sigma}$, one can derive a general expression for higher-order l-pole (quadrupole, octopole, and so on...) moment integrals, with $\langle d_X^2\rangle = \langle M_1^2\rangle$:

$$\langle M_l^2\rangle = \sum_\sigma d\boldsymbol{r}\rho_\sigma(\boldsymbol{r})[r^l - (r - d_{X\sigma})^l]^2. \tag{2.73}$$

The XDM expressions for the C_6 and higher-order dispersion coefficients (C_8, C_{10}, etc.) can be derived from the second-order perturbation theory of dispersion.[149,150] The expression for the leading-order C_6 coefficient (between atoms A and B) is:

$$C_6 = \frac{\alpha_A\alpha_B\langle d_X^2\rangle_A\langle d_X^2\rangle_B}{\alpha_B\langle d_X^2\rangle_A + \alpha_A\langle d_X^2\rangle_B}, \tag{2.74}$$

where α_A and α_B are the atomic polarizabilities of atoms A and B, respectively. For atom i, α_i is proportional to its atomic volume V_i:

$$\alpha_i = \frac{V_i}{V_{i,\text{free}}}\alpha_{i,\text{free}}, \tag{2.75}$$

where $\alpha_{i,\text{free}}$ denotes the free atomic polarizability, which is experimentally measured *in vacuo*. $V_i/V_{i,\text{free}}$ is determined through Hirshfeld charge analysis[151] of the calculated electron density.

The HF exchange hole shown in eq. 2.68 is infeasible to compute for periodic systems. In practical XDM calculations, a density-functional approximation to the exact-exchange hole, the Becke-Roussel[152] model ("the BR hole") is used instead. The BR hole model simplifies the exchange hole into an exponential function,

$-Ae^{-ar}$, centered at distance b from the reference electron. There are three property constraints on the BR hole:

- normalization to -1 electron,
- elimination of spin-density, ρ_σ, at the reference point,
- same reference-point curvature as the HF exchange hole.

From these constraints we can obtain the value of the three parameters: A, a, and b. In particular we have

$$b^3 = \frac{x^3 e^{-x}}{8\pi\rho_\sigma}, \tag{2.76}$$

with $x = ab$ obtained via solving the nonlinear equation

$$\frac{xe^{-2x/3}}{x-2} = \frac{2}{3}\pi^{2/3}\frac{\rho_\sigma^{5/3}}{Q_\sigma}. \tag{2.77}$$

The curvature, Q_σ, is obtained from ρ_σ and the kinetic-energy density, τ_σ:

$$Q_\sigma = \frac{1}{6}\left[\nabla^2\rho_\sigma - 2\left(\tau_\sigma - \frac{1}{4}\frac{(\nabla\rho_\sigma)^2}{\rho_\sigma}\right)\right], \tag{2.78}$$

where τ_σ is

$$\tau_\sigma = \sum_i (\nabla\psi_{i\sigma})^2. \tag{2.79}$$

Under the BR-hole approximation, the exchange-hole dipole moment is simply $d_{X\sigma} = b$, which is used in the practical calculation of dispersion coefficients. The BR hole by itself can be regarded as a meta-GGA density functional due to its dependence on ρ_σ, $\nabla\rho_\sigma$, τ_σ, and $\nabla^2\rho_\sigma$. The BR-hole variant of XDM has been shown to yield excellent results for molecular C_6 dispersion coefficients, improving upon the HF-exchange hole, when paired with pure density functionals.[143]

The energy correction for London dispersion is a series expansion of all pairwise interatomic interactions:

$$E_{\text{disp}} = -\sum_{ij}\sum_{n=6,8,10}\frac{C_{n,ij}f_n(R_{ij})}{R_{ij}^n}, \tag{2.80}$$

where R_{ij} is the distance between atoms i and j, and f_n is the so-called Becke-Johnson (BJ) damping function[153] for the C_n dispersion term. The purpose of f_n is to prevent the divergence of E_{disp} at short interatomic distances, converging E_{disp} to some finite value at the onset of the repulsive potential wall between two approaching atoms. f_n has the form

$$f_n(R_{ij}) = \frac{R_{ij}^n}{R_{ij}^n + (a_1 R_{c,ij} + a_2)^n}. \tag{2.81}$$

Here $R_{c,ij}$ denotes a "critical" interatomic separation distance where contributions to E_{disp} from the C_6, C_8, and C_{10} terms become equal. $R_{c,ij}$ depends on the dispersion coefficients and, in practice, has three possible choices of definition:

$$R_{c,ij} = \left(\frac{C_{8,ij}}{C_{6,ij}}\right)^{\frac{1}{2}}, \left(\frac{C_{10,ij}}{C_{8,ij}}\right)^{\frac{1}{2}}, \left(\frac{C_{10,ij}}{C_{6,ij}}\right)^{\frac{1}{4}}. \tag{2.82}$$

In XDM, $R_{c,ij}$ is taken as the average of these three possible values. The BJ damping function incorporates two damping parameters, a_1 and a_2, which are empirically fit to minimize binding-energy errors for Kannemann and Becke's training set of 49 molecular dimers[143] for each specific exchange-correlation functional used.

The XDM model, paired with the B86bPBE density functional, has been shown to yield excellent results in solid-state calculations,[154] comparable (within 1 kcal/mol for lattice energies) to values obtained from much more expensive methods, such as the random phase approximation (RPA)[155] and non-local correlation functionals based on the adiabatic-connection fluctuation-dissipation theorem (ACFDT).[156] The overall performance of the XDM model is on par with, or better than, other popular post-SCF dispersion correction methods, such as Grimme's DFT-D3,[157,158] the Tkatchenko-Scheffler van der Waals (TS-vdW) method,[159] and its many-body dispersion (MBD) extension.[160,161] The XDM model also stands out for its strong physical motivation and its dynamic dependence of both the moment integrals and polarizabilities on the calculated electron density. The XDM model also possesses high transferability between molecular and solid-state systems without any modification.

Chapter 3

The Effect of Electronic Excitation on London Dispersion

The work presented in this current chapter has been published as an article: Xibo Feng, Alberto Otero-de-la-Roza, and Erin R. Johnson, *The Effect of Electronic Excitation on London Dispersion*, Can. J. Chem. **96**: 730–737 (2018).

Synopsis: Atomic and molecular dispersion coefficients can now be calculated routinely using density-functional theory. In this work, we present the first determination of how electronic excitation affects molecular C_6 London dispersion coefficients from the exchange-hole dipole moment (XDM) dispersion model. Excited states are typically found to have larger dispersion coefficients than the corresponding ground states, due to their more diffuse electron densities. A particular focus is both intramolecular and intermolecular charge-transfer excitations, which have high absorbance intensities and are important in organic dyes, light-emitting diodes, and photovoltaics. In these classes of molecules, the increase in C_6 for the electron-accepting moiety is largely offset by a decrease in C_6 for the electron-donating moiety. As a result, the change in dispersion energy for a chromophore interacting with neighbouring molecules in the condensed phase is minimal.

3.1 Introduction

The study of electronic excitations is essential in many areas of chemistry. Molecular electronic excitations play important roles in the design and fabrication of organic electronics[162,163] (sensors, light-emitting diodes, photovoltaics, etc.). While properties of the excited state have been extensively studied for single molecules in the gas-phase and in solution, little is known regarding how excitation of a single molecule affects the intermolecular interactions with its neighbours.[164,165] In particular, to our knowledge, there has only been one investigation to date as to how electronic excitation affects the strength of intermolecular London dispersion interactions[166] and this was limited to a small set of van der Waals complexes rather than common chromophores.[167] This may be, in part, because popular empirical dispersion models have dispersion coefficients that are either fixed[89,168] or depend only on the geometry[157] and consequently cannot describe correctly the change in intermolecular dispersion during a vertical excitation. Alternatively, while non-local density-functional dispersion models are transferable to excited states,[166] they do not directly provide atomic or molecular dispersion coefficients.

The exchange-hole dipole moment (XDM) model,[102,103,169,170] in the context of density-functional theory (DFT), is uniquely suited to address the question of how electronic excitation affects London dispersion. The XDM model provides a non-empirical means of calculating accurate C_6 (and higher-order[171]) dispersion coefficients directly from the electron density. As such, the XDM dispersion coefficients are sensitive to changes in an atom's electronic environment[172–174] and the method is completely transferable, without modification, from ground-state to excited-state electron densities.

In XDM, the dispersion energy is an *a posteriori* correction to the self-consistent energy, calculated using one of the common density functionals. The dispersion energy is written as a sum over all pairs of atoms, i and j separated by a distance R_{ij}, and includes C_6, C_8, and C_{10} dispersion terms.

$$E_{\text{disp}}^{\text{XDM}} = -\sum_{n=6,8,10}\sum_{i<j}\frac{C_{n,ij}f_n(R_{ij})}{R_{ij}^n} \tag{3.1}$$

The damping function, $f_n(R_{ij})$, prevents the divergence of the dispersion energy at

small internuclear separations. The atomic C_6 dispersion coefficients are determined from the exchange-hole dipole moment integrals, $\langle d_X^2 \rangle$, and atom-in-molecule polarizabilities, α.

$$C_{6,ij} = \frac{\alpha_i \alpha_j \langle d_X^2 \rangle_i \langle d_X^2 \rangle_j}{\alpha_i \langle d_X^2 \rangle_j + \alpha_j \langle d_X^2 \rangle_i} \tag{3.2}$$

Analogous formulae can be written for the higher-order dispersion coefficients and involve higher-order exchange-hole multipole moments. The moment integrals and polarizabilities are both functions of the electron density and consequently vary with atomic environment. Interested readers are directed to Ref. 170 for a comprehensive review of the XDM equations and the theory underpinning the model. The overall molecular C_n dispersion coefficient can be evaluated by summing over all atom pairs.

$$C_n = \sum_{ij} C_{n,ij} \tag{3.3}$$

This value is the C_n dispersion coefficient for the interaction between one molecule and a second, identical molecule.

In this work, the XDM model is applied to investigate how the molecular dispersion coefficients change upon electronic excitation for a small collection of molecular systems, which can be broken down into three classes. These are $\pi \rightarrow \pi^*$ excitations in conjugated hydrocarbons, charge-transfer excitations in push-pull chromophores of 4,4′-disubstituted biphenyls, and intermolecular excitations in charge-transfer complexes. Additionally, we consider a set of ten molecular crystals and co-crystals and assess how changes in dispersion coefficients resulting from electronic excitation affect the dispersion energy for interaction of a single excited molecule with the surrounding bulk. This dispersion contribution to the excitation energy has not previously been considered when modeling electronic excitations of molecules in the condensed phase.

3.2 Computational Methods

3.2.1 Molecular calculations

All molecular calculations were performed using the Gaussian 09 program.[175] Geometries of all molecules and intermolecular complexes were optimized using

B3LYP[90,114] or B3LYP-XDM, respectively, both with the 6-31+G* basis set. Subsequent single-point energy calculations and time-dependent density-functional theory (TDDFT)[118,176–178] calculations were performed with either the 6-31+G* basis set for single molecules or aug-cc-pVDZ for complexes and either the B3LYP[90,114] or CAM-B3LYP[120] density functionals. Usually the first singlet excited state was considered, but occasionally a higher excited state was investigated, corresponding to the charge-transfer state for the push-pull chromophores or intermolecular charge-transfer complexes (see below).

Change-transfer excitations are well known to be problematic for functionals with little or no exact-exchange mixing,[119,179–184] due to the density-functional "delocalization" or "charge-transfer" error.[112,185–189] As such, calculations on intermolecular charge-transfer complexes were performed using systematic series of hybrid and range-separated hybrid density functionals with varying exact-exchange mixing. Specifically, a family of BLYP[108,114]-based hybrid functionals of the form

$$E_{\mathrm{XC}} = a_{\mathrm{X}} E_X^{\mathrm{exact}} + (1 - a_{\mathrm{X}}) E_{\mathrm{X}}^{\mathrm{B88}} + E_{\mathrm{C}}^{\mathrm{LYP}} \tag{3.4}$$

was used, where the exact-exchange mixing fraction, a_{X} was varied from 0 to 1 in increments of 0.1. Similarly, we also considered a family of range-separated hybrid functionals based on LC-BLYP.[190] In these functionals, the interelectronic Coulomb potential is divided into short- and long-range terms using the error function:

$$\frac{1}{r_{12}} = \frac{1 - \mathrm{erf}(\omega r_{12})}{r_{12}} + \frac{\mathrm{erf}(\omega r_{12})}{r_{12}}. \tag{3.5}$$

This modified Coulomb potential is then used in evaluation of the exchange energy such that the short-range portion is treated with the B88 generalised-gradient-approximation functional[108] and the long-range component is treated with exact exchange. The length of this range-separation is determined by the parameter ω, whose value was varied from 0 to 1 Bohr^{-1} in increments of 0.1 Bohr^{-1}. In evaluation of the exchange-hole dipole moments, and resulting XDM dispersion coefficients, the Becke-Roussel exchange-hole model[152] was used in all calculations. As such, the full two-particle density matrix for the excited state was not required. We need only the expansion of the Kohn-Sham orbitals in terms of the atomic basis functions,

which can be obtained from the wavefunction file. The `density=current` option in the Gaussian program[175] was used to generate wavefunction files for excited states. The ground state density, ρ_{gs}, is obtained from the usual sum of the squares of the occupied, real Kohn-Sham orbitals: $\rho_{gs} = \sum_{i,\sigma} \psi_{i\sigma}^2(\mathbf{r})$. The excited-state density, ρ_{ex} is determined from the first-order density response and is given by[118,191]

$$\rho_{ex} = \rho_{gs} + \sum_{i,a,\sigma} P_{ia\sigma}\psi_{i\sigma}(\mathbf{r})\psi_{a\sigma}(\mathbf{r}), \tag{3.6}$$

where index i refers to the occupied Kohn-Sham orbitals, index a the virtual Kohn-Sham orbitals, and σ denotes the electron spin. The $P_{ia\sigma}$ coefficients are determined from solution of the Casida equation in TDDFT.[176,192] The BR procedure is then applied to calculate the exchange-hole dipole moments and dispersion coefficients[169,170,193] from the density and orbitals. The postg program[194] was used to calculate the C_6 dispersion coefficients and Hirshfeld[151] atomic charges for both the ground and excited states.

3.2.2 Solid-state calculations

Crystal structures of 4-amino-4′-nitrobiphenyl, A3MN [2-Amino-3-((E)-(4-(diethylamino) benzylidene)amino)maleonitrile],[195] coumarin, 6-aminocoumarin, and the benzene/hexafluoro-benzene, N,N-dimethylaniline/hexafluorobenzene, naphthalene/hexafluorobenzene, tetracyanoethylene/naphthalene, chloranilic acid/pyrazine, and 2,5-dimethylbenzoquinone/bis-(hydroquinone) co-crystals, were obtained from the Cambridge Crystallographic Data Centre[196] (codes: KEFLEM01, PAQMIE01, RAZLEK, BEZZAJ, BICVUE01, DMAFBZ01, IVOBOK, CYENAP, BOQHOE, and CISCOW, respectively). The structures of these crystals (both atomic positions and unit-cell parameters) were then optimized with B86bPBE-XDM[88,107,154,170] using the Quantum ESPRESSO program.[101] These calculations used Projector-Augmented-Wave (PAW) pseudopotentials, a $4 \times 4 \times 4$ k-point mesh, and energy and density plane-wave cut-offs of 60 and 600 Ry, respectively. After optimization, single-point energy and TDDFT calculations were performed on a single molecule cut from the crystal at this fixed geometry. These calculations used Gaussian 09 as detailed above, with the B3LYP functional and the 6-31+G* basis set. The London dispersion coefficients were calculated from the resulting electron

densities using the postg program.[194] These coefficients were then used to evaluate the dispersion energy for interaction of this single molecule, in either its ground or excited state, with the remainder of the crystal, using the critic2 program.[197]

Figure 3.1: The constituents of conjugated-chain set of molecules.

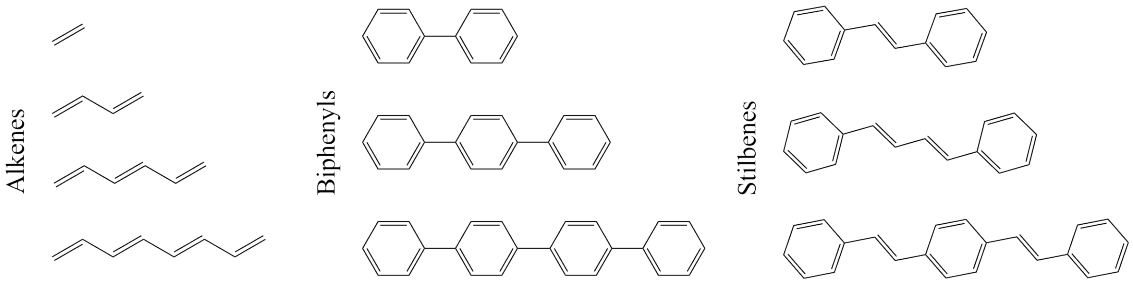

3.3 Results and Discussion

3.3.1 Conjugated hydrocarbons

We begin by considering the $\pi \rightarrow \pi^*$ excitations for the set of conjugated hydrocarbon molecules shown in Figure 3.1. This set consists of a mixture of straight-chain alkenes, biphenyls, and stilbenes. As $\pi \rightarrow \pi^*$ excitations are much less sensitive to the choice of DFT method than are charge-transfer excitations, we consider only B3LYP results. Figure 3.2 shows the percent change in molecular C_6 dispersion coefficients for all members of this set, as a function of either excitation energy (a,b) or chain length (c,d).

The results in Figure 3.2(a,b) show that the percent change in molecular C_6 upon excitation increases exponentially with increasing excitation energy for each distinct series of compounds (alkenes, stilbenes, and biphenyls). This is to be expected as the valence electron becomes more weakly bound in higher-energy excited states, causing the electron density to be more diffuse, which in turn causes the dispersion coefficients to increase. In particular the percent increase in C_6 upon excitation of ethylene is extremely large (in excess of 200%) and even larger increases appear in high-energy Rydberg excitations. However, as such high-energy excitations are not observed in everyday chemical applications, we focus our attention on lower-energy

$\pi \rightarrow \pi^*$ and charge-transfer excitations.

While the excitation energies for the conjugated-chain set vary significantly depending on the molecule type, a simplified picture of the effect of excitation on C_6 can be obtained by recourse to a particle-in-a-box model in which only the chain length of each hydrocarbon is considered. Figure 3.2(c,d) shows the that percent change in C_6 decreases with increasing chain length, using two possible definitions (either the Euclidean length or number of C-C bonds between distal carbon atoms, with the latter yielding a slightly improved correlation). In the context of the particle-in-a-box, a shorter chain, or box, length results in a more loosely-bound excited state, leading to large increases in C_6 upon excitation. Conversely, a longer chain length results in a more-tightly bound excited state, leading to smaller relative increases in C_6 upon excitation. Figure 3.2(c,d) also shows that C_8 and C_{10} follow the same trends as seen for C_6, although the percentage increase induced by the excitation is higher for the higher-order dispersion coefficients.

Lastly, we decompose the changes in C_6 into contributions from the two types of terms in Equation 3.2: the moment integrals and atomic polarizabilities. As the densities in the excited states are more diffuse, one might expect that an increase in polarizability would be the primary contribution to the change in molecular C_6. However, more diffuse densities will also cause a larger average displacement between a reference electron and its corresponding exchange hole, which remains centered near the nearest atomic nucleus.[152] Thus the moment integrals also increase upon excitation, and Figure 3.3 shows that the relative contributions from the moment integrals and polarizabilities are roughly equivalent. This is similar to what is seen for changing chemical environments in ground-state molecules,[170,172] but contrary to solids where changes in C_6 are dominated by changes in the exchange-hole dipole moment integrals.[170,173]

3.3.2 Push-pull chromophores

Next we consider the set of 4,4'-disubstituted biphenyls shown in Figure 3.4(a). These molecules can be classified as "push-pull" systems since one substituent is a strong electron-donating group (EDG) while the other is an electron-withdrawing group (EWG). In all cases either the first or second excited state corresponds to a charge-transfer state, as determined from the Hirshfeld charges. In our

Figure 3.2: Changes in molecular C_6 dispersion coefficients as a function of excitation energy for subsets of (a) alkenes and (b) stilbenes and biphenyls. Also shown are changes in C_6, C_8, and C_{10} dispersion coefficients for the conjugated-chain set as a function of chain length using two different definitions: (c) the Euclidean distance between terminal carbon atoms and (d) the number of C-C bonds forming the chain. The lines are to guide the eye.

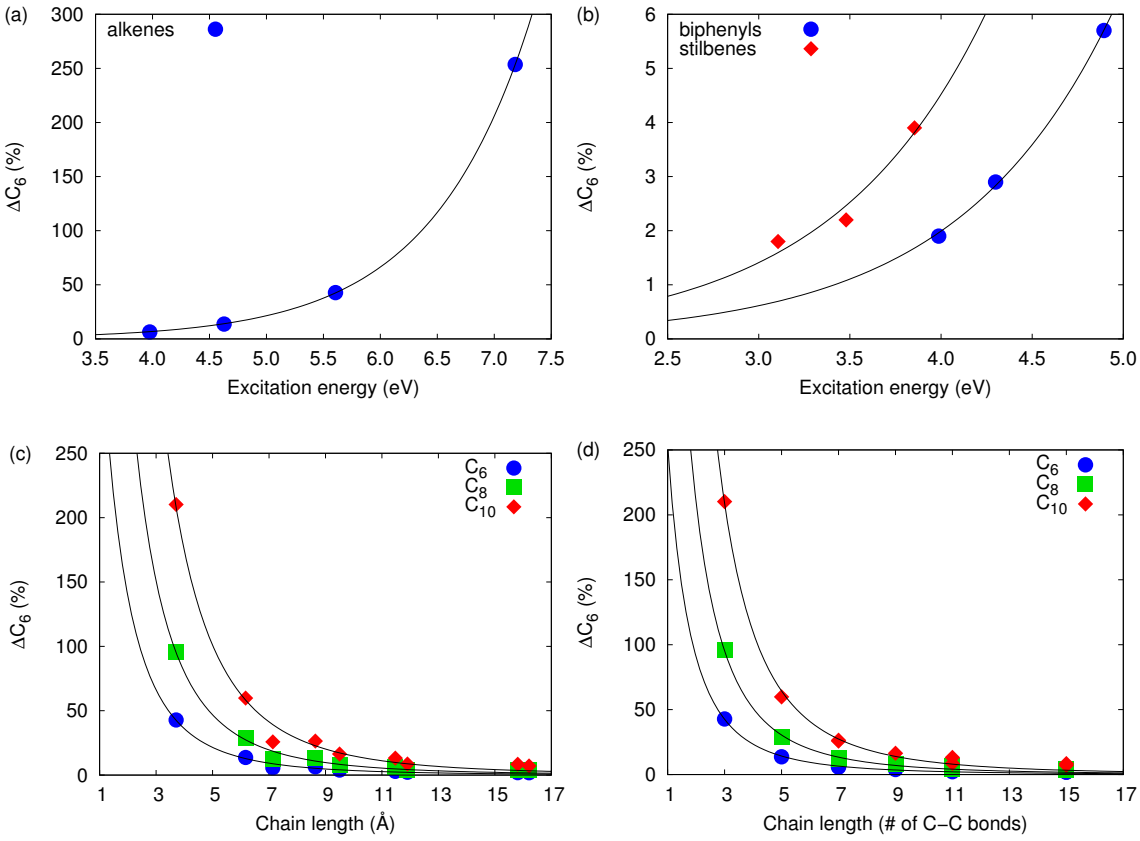

analysis, the charges and dispersion coefficients of these molecules are partitioned into contributions from the electron-donating and electron-accepting halves which are separated by the central C-C single bond. The extent of charge transfer is determined as the absolute value of the difference in the Hirshfeld charge between the ground and excited state, for either of these two halves of a given molecule.

Figure 3.4(b) shows the extent of charge transfer as a function of the calculated excitation, with both B3LYP and CAM-B3LYP. Range-separated functionals, such as CAM-B3LYP, are conventionally viewed as being the more reliable for charge-transfer excitations,[95,97,198,199] although one must be careful not to generalise this result, particularly to large systems, as the performance of range-separated

Figure 3.3: Decomposition of the changes in molecular C_6 dispersion coefficients into contributions from the dipole-moment integrals and polarizabilities. Results are shown for the conjugated-chain set as a function of chain length, defined as the number of C-C bonds forming the chain.

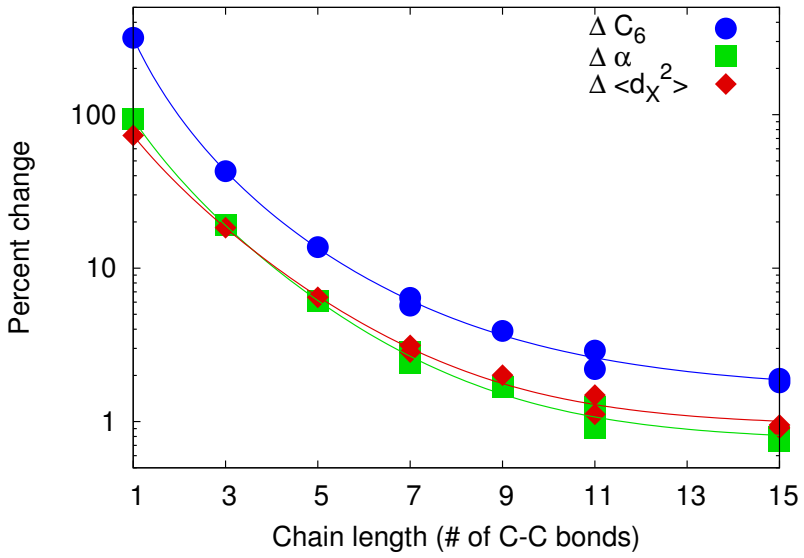

functionals is highly system-dependent.[200–202] Figure 3.4(b) shows that going from B3LYP to CAM-B3LYP leads to higher excitation energies and reduced charge transfer, as expected since the latter functional was designed to minimise charge-transfer errors. However, the correlation between these two quantities becomes less clear than with B3LYP. Considering trends with substituent, the amino group is a stronger EDG than the hydroxyl group, resulting in greater charge-transfer and lower excitation energies. For the EWGs, the excitation energies follow the trend $NO_2 < CHO < COOH < CN < CF_3$ and the extent of charge transfer follows the inverse trend.

Figure 3.4 also shows the change in C_6 for the EDG and EWG halves of the biphenyls, obtained with B3LYP (c) and CAM-B3LYP (d). In general, the C_6 for the EDG decreases upon excitation as charge is transferred away from this region of the molecule, resulting in a more compact electron density. Conversely, the C_6 for the EWG increases upon excitation as charge is transferred to this region of the molecule, resulting in a more diffuse electron density. CAM-B3LYP predicts somewhat lower charge transfer, which results in smaller increases in the EWG C_6 and smaller decreases in the EDG C_6 compared to B3LYP. However, as these effects

Figure 3.4: The set of selected 4,4'-disubstituted biphenyls (a) together with the calculated extent of charge transfer as a function of excitation energy (b). Also shown are the excitation-induced changes in C_6 for the electron-donating and electron-withdrawing halves of each biphenyl from B3LYP (c) and CAM-B3LYP (d). Coloured symbols correspond to hydroxyl electron donors and open symbols correspond to amino electron donors.

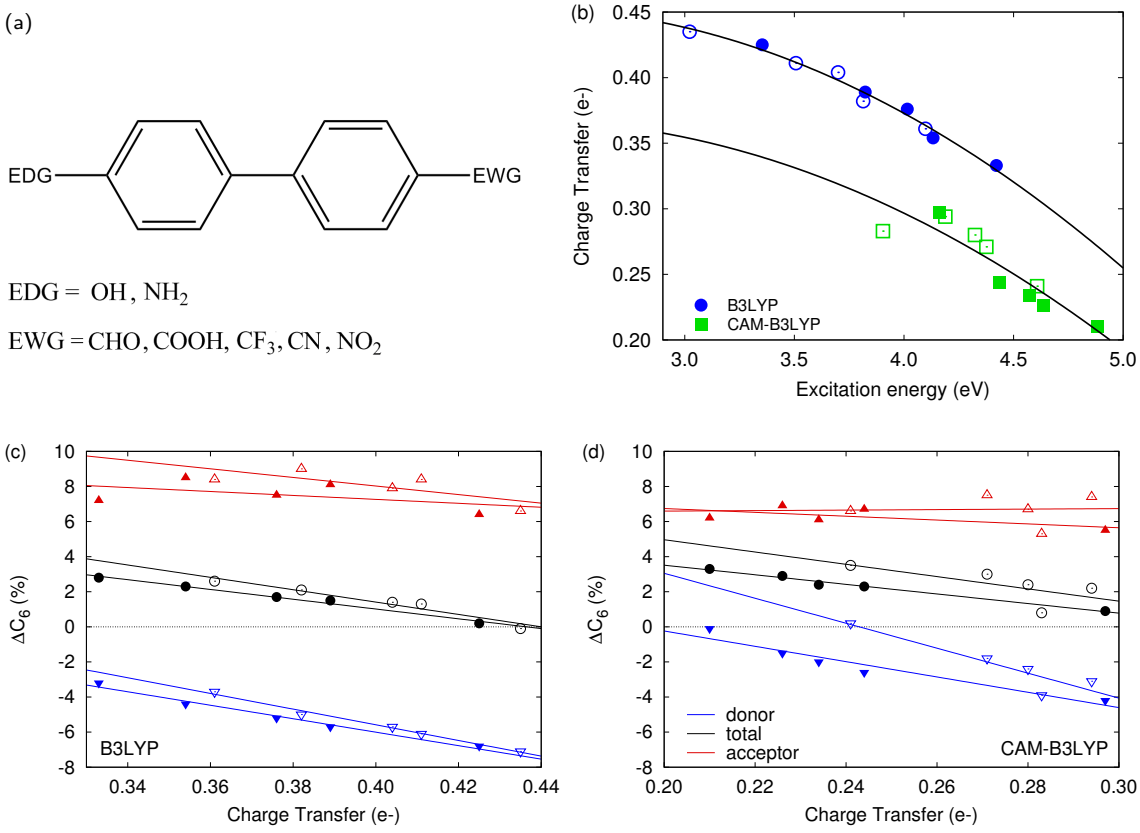

offset, the overall differences in total C_6 values remain small and are only 0-4% for the molecules in the set, with both functionals.

Lastly, regarding substituent effects, the magnitude of ΔC_6 for the EDG tends to increase with greater charge transfer, as it becomes more positive in the excited state. For the EWG, the ΔC_6 tends to increase as the extent of charge transfer decreases. This is due to the inverse relationship between charge transfer and excitation energy; reduced charge transfer occurs when the excited state is higher in energy, resulting in more diffuse electron densities and higher C_6 coefficients in the excited state. Additionally, two distinct trends lines are present in Figure 3.4(c,d), one for each EDG, with larger increases in C_6 occurring for the amino substituent than for the

hydroxyl substituent.

3.3.3 Intermolecular charge-transfer excitations

As shown in the previous section, overall increases in molecular dispersion coefficients on excitation are minimal for intramolecular charge-transfer excitations. In this section, we consider two intermolecular charge-transfer complexes: benzene/hexafluorobenzene (in C_{6v} symmetry) and benzene/tetracyanoethylene (in C_{2v} symmetry), both of which possess fairly low-lying intermolecular charge-transfer excitations. Due to the delocalization (or charge-transfer) error, we expect the results for these intermolecular complexes to be much more sensitive to the choice of density functional than were the data for the biphenyls. We therefore consider the effect of exact-exchange mixing on the extent of excitation-induced charge transfer and changes in the C_6 coefficients using series of hybrid and range-separated hybrid functionals.

Figure 3.5(a,b) show plots of the charge-transfer excitation energy as a function of exact-exchange mixing fraction or range-separation parameter for the two intermolecular complexes. In general, the density-functional delocalization error causes local density functionals (i.e. those with no exact-exchange mixing) to over-stabilise fractional charges and to underestimate charge-transfer excitation energies.[112,119,179–189] This is reflected in Figure 3.5(a,b) which show systematic increases in the excitation energies as the exact-exchange mixing fraction or range-separation parameter is increased.

Next, Figure 3.5(c,d) show the excitation-induced charge transfer and reveal differing behaviour for these complexes. In both cases, the BLYP functional, with no exact-exchange mixing, predicts fractional charge transfer of near one-half of an electron (0.58 e^- for benzene/hexafluorobenzene and 0.44 e^- for benzene/tetracyanoethylene). This is expected as delocalization error causes local functionals to over-stabilise fractional charges. As exact exchange is incorporated into the functional, the extent of charge transfer tends towards integer values. However, the trends are opposing for the complexes, with the charge transfer decreasing to zero for benzene/hexafluorobenzene and increasing to 0.8 e^- for benzene/tetracyanoethylene. This would seem to imply that the latter case is a "true" charge-transfer excitation, while the low-energy charge-transfer excitation

Figure 3.5: Calculated properties of the benzene-hexafluorobenzene (left) and benzene-tetracyanoethylene (right) complexes as a function of exact-exchange mixing (a_X) in BLYP-based hybrids (filled symbols, solid lines) or range-separation (ω) parameters in LC-BLYP-based functionals (open symbols, dashed lines). Shown are the excitation energies (top row), extent of excitation-induced charge transfer (middle row), and excitation-induced changes in C_6 dispersion coefficients (bottom row).

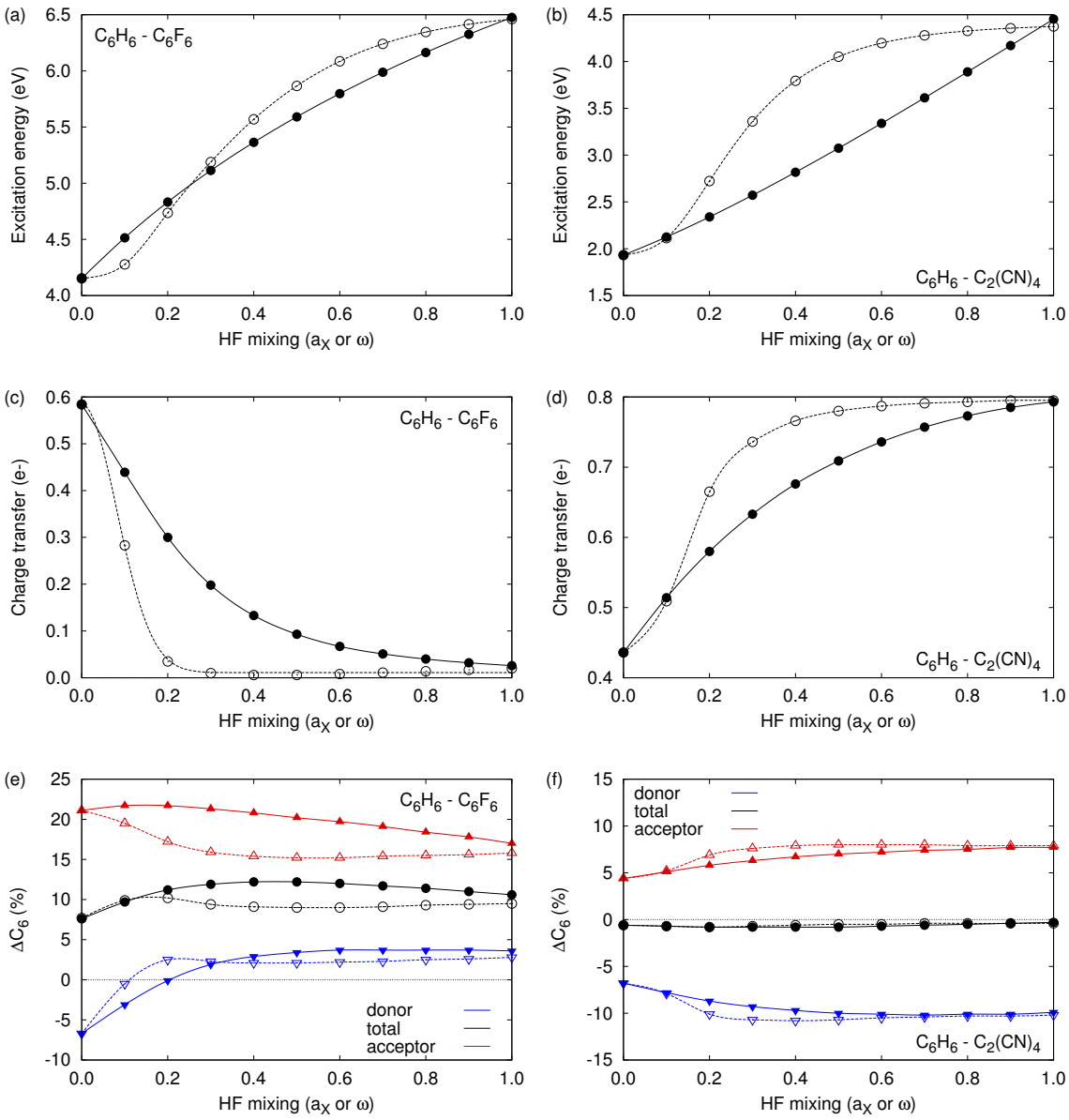

seen in the former complex is an artifact caused by delocalization error.

Finally, Figure 3.5(e,f) show the excitation-induced changes in C_6 London dispersion coefficients for the complexes, as well as for the component donor and acceptor molecules. Despite the high sensitivity of both the charges and excitation energies, the dispersion coefficients show minimal functional dependence, particularly for benzene/tetracyanoethylene. This indicates that use of popular hybrid functionals, like B3LYP, should be adequate to describe dispersion properties, even for strong charge-transfer excitations. As for the disubstituted biphenyls, the C_6 of the electron donor decreases on excitation while the C_6 of the electron acceptor increases. These effects offset almost completely for benzene/tetracyanoethylene; however, for benzene/hexafluorobenzene, there is a net increase in C_6 of roughly 10%, much larger than those seen in the biphenyls or conjugated hydrocarbons. This implies that changes in dispersion energy coming from excitation may be larger for co-crystals than single-molecule crystals, and this will be confirmed in the following section.

3.3.4 Dispersion in crystalline solids

Having established that electronic excitation has the potential to cause large changes in molecular dispersion coefficients, we next assess the impact of this effect on the dispersion energy for interaction of a single molecule with a surrounding crystal environment. We consider a set of 4 single-molecule crystals and 6 co-crystals, shown in Figure 3.6.

The results in Table 3.1 show that the changes in C_6 on excitation remain quite low for the single molecules exhibiting intramolecular charge-transfer excitations, as expected from the results in Section 3.3.2. While $\%\Delta C_6$ may be significantly larger in magnitude for some of the intermolecular charge-transfer excitations, the resulting changes in dispersion energy for excitation of a molecular dimer within the co-crystal remain quite small in magnitude. This is partly because the moment integrals and polarizabilities for only a single molecular dimer are changing, so the resulting effect on the dispersion coefficients for interactions with the remainder of the crystal are effectively halved relative to what would be seen for interaction between two excited moieties. Additionally, the larger relative increases in the higher-order dispersion coefficients (Figure 3.1) cause increases in the effective atomic van der Waals radii

Figure 3.6: Structures of selected chromophores present in molecular crystals together with their CCDC codes.

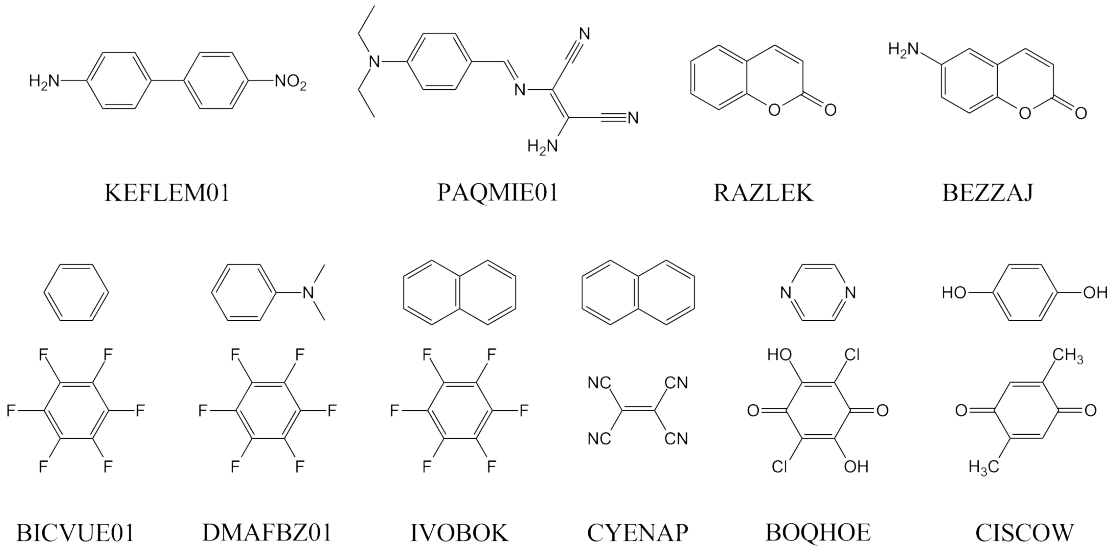

used in the XDM damping function. This results in increased damping of the dispersion energy, which largely offsets the effect of increasing dispersion coefficients. Indeed, in the majority of cases considered, the increased damping causes a lower dispersion energy in the excited state than in the ground state, as reflected by the many positive values of ΔE_{disp} in Table 3.1.

The largest changes in dispersion energy resulting from a localised excitation are -1.2 kcal/mol for benzene/hexafluorobenzene and 1.2 kcal/mol for naphthalene/hexafluorobenzene. While examples could likely be found with larger dispersion-energy changes, this finding indicates that this dispersion effect has a very minor contribution to the overall excitation energy for a molecule or dimer in the condensed phase.

3.4 Summary

This is the first work to consider the effect of electronic excitation on molecular London dispersion coefficients. Excitation increases the dispersion coefficients as the electron density distribution in the excited state is more diffuse, resulting in larger atomic polarizabilities and exchange-hole multipole moment integrals, with these two contributions being roughly equivalent in size. The percentage change in

Table 3.1: Changes in molecular C_6 coefficients for a single excited moiety (single molecule or charge-transfer dimer) and overall dispersion energies for interaction of the chromophore with surrounding molecules in the crystal.

Molecule	$\%\Delta C_6$	ΔE_{disp} (kcal/mol)
4-amino-4′-nitrobiphenyl	0.3	-0.16
A3MN	0.9	0.17
coumarin	1.9	0.18
6-aminocoumarin	2.8	0.14
benzene/hexafluorobenzene	7.8	-1.24
N,N-dimethylaniline/hexafluorobenzene	2.8	0.07
naphthalene/hexafluorobenzene	4.6	1.23
tetracyanoethylene/naphthalene	-0.3	0.39
chloranilic acid/pyrazine	-0.3	0.46
2,5-dimethylbenzoquinone/bis(hydroquinone)	24.4	1.02

the C_6 dispersion coefficient was found to decrease with increasing chain length for $\pi \rightarrow \pi^*$ excitations in conjugated hydrocarbons. For charge-transfer excitations, the dispersion coefficients for the electron-donating moiety decrease, while the dispersion coefficients for the electron-withdrawing moiety increase. The combined effect on the overall dispersion coefficient is negligible for intramolecular charge transfer, but can be fairly large for intermolecular charge transfer. However, despite the potential for large changes in dispersion coefficients, electronic excitation of a single molecule has only a minimal effect on the dispersion energy for interaction of the chromophore with the surrounding bulk in a molecular crystal or co-crystal.

Chapter 4

Assessing the Performance of Becke's Virial Exciton Model for Charge-Transfer Excitations

The work presented in this current chapter has been published as an article: Xibo Feng, Axel D. Becke, and Erin R. Johnson, *Communication: Becke's Virial Exciton Model Gives Accurate Charge-Transfer Excitation Energies*, J. Chem. Phys. **149**, 231101 (2018).

Synopsis: First singlet (S_1) excitations are of primary importance in the photoluminescence spectra of organic chromophores. However, due to the multi-determinantal nature of the singlet excited states, standard Kohn-Sham density-functional theory (DFT) is not applicable. While linear-response time-dependent DFT is the method of choice for the computation of excitation energies, it fails severely for excitations with charge-transfer character. Becke's recent virial exciton model[100] offers a promising solution to employ standard DFT for calculation of the S_1 excitation energy in molecular systems. Here, it is shown that the virial exciton model is free of charge-transfer error. It is equally reliable for S_1 excitations with significant charge-transfer character as for other classes of transitions.

4.1 Introduction

The photoluminescence of organic chromophores plays a fundamental role in nature, with prominent examples being photosynthesis,[203] vision,[204] and bioluminescence.[205] Recent applications of photoluminescent materials include development of organic light-emitting diodes,[8,9] fluorescent sensors,[4,19] lasers,[10] waveguides,[206] and biomedical imaging.[11,19] The first singlet (S_1) electronic excitation is of primary importance in photoluminescence spectra. Computational modeling of these excitations is complicated as standard Kohn-Sham density-functional theory (DFT)[106] is not applicable to the S_1 excited state due to its multi-determinant nature. Linear-response time-dependent density-functional theory (TDDFT)[45,46,118] is the predominant method employed for the calculation of S_1, and higher, excitation energies. However, TDDFT typically exhibits a severe underestimation of the excitation energy (frequently in excess of 1 eV) when the excitation is of charge-transfer (CT) character.[97,119,181,182,207] This problem can be ameliorated using long-range-corrected hybrid functionals, but the optimum range-separation parameter in these functionals is extremely system dependent.[200,202,208] Also, time-independent methods as exemplified by the very recent work of the Van Voorhis group (see Ref. 209 and references therein) are known which can handle CT excitations well. We recommend Ref. 210 for extensive reviews of both time-dependent and time-independent approaches to excited states in DFT.

Becke recently derived a simple model[100] for the energy splitting between the first singlet and triplet (S_1-T_1) excited states, and hence the S_1 excitation energy itself, based on the virial theorem.[211] This "virial exciton model" only requires conventional DFT calculations for the S_0 ground state and the (single-determinant) T_1 excited state. It therefore represents a simple alternative to TDDFT for calculation of the S_1 excitation energy in molecular systems. For Thiel's benchmark set[124] of 28 small-molecule excitation energies, the virial exciton model achieves a mean absolute error (MAE) for S_1 on par with TD-B3LYP (0.26 and 0.24 eV, respectively), relative to high-level correlated wavefunction reference data. Remarkably, it significantly out-performs TD-B3LYP for S_1 excitation energies of polycyclic aromatic hydrocarbons,[212] achieving a MAE of 0.13 eV, versus the TD-B3LYP value of 0.31 eV.[100]

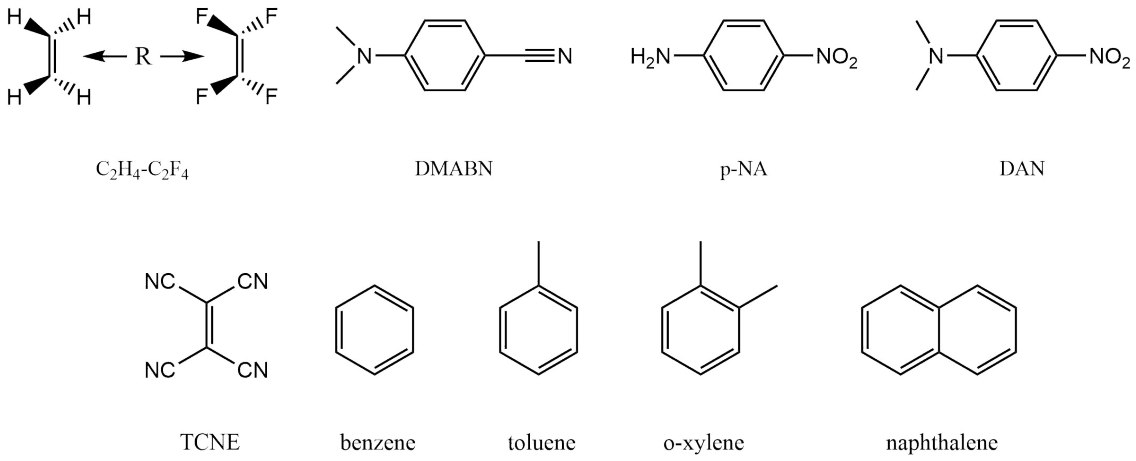

Figure 4.1: The chemical systems investigated in this work. Shown are the ethylene-tetrafluoroethylene (C_2H_4-C_2F_4) complex; the donor-acceptor molecules 4-dimethylamino-benzonitrile (DMABN), *para*-nitroaniline (p-NA), and *N,N*-dimethyl-4-nitroaniline (DAN); and the intermolecular CT dimers between tetracyanoethylene (TCNE) and each of benzene, toluene, o-xylene, and naphthalene.

In this work, the performance of the virial exciton model for systems that feature S_1 excitations of significant CT character will be assessed for the first time. It is a two-step method, beginning with a conventional T_1 excitation-energy computation, followed by a simple two-electron integral correction. The first step ensures, in large part, that the method does not suffer the CT failures of TDDFT. Our benchmark set (see Fig. 4.1) consists of three subsets: (i) the ethylene-tetrafluoroethylene intermolecular CT dimer that has been used as a classic demonstration of TDDFT charge-transfer error;[119] (ii) four intermolecular CT dimers consisting of tetrafluoroethylene and aromatic hydrocarbons, for which experimental S_1 excitation energies are available;[213,214] and (iii) three donor-acceptor molecules featuring S_1 excitations with intramolecular CT, for which high-level correlated wavefunction benchmark data are available.[215,216] The results show that the virial exciton model is free of CT error.

4.2 Theory

In the virial exciton model, the difference between the S_1 and T_1 excitation energies is given by the following two-electron integral:

$$\Delta E_{\mathrm{ST}} = H_{12} = \int\int d^3\mathbf{r}_1 d^3\mathbf{r}_2 \frac{\phi_i(\mathbf{r}_1)\phi_f(\mathbf{r}_1)\phi_i(\mathbf{r}_2)\phi_f(\mathbf{r}_2)}{r_{12}}, \tag{4.1}$$

where ϕ_i and ϕ_f are the initial and final Kohn-Sham (KS) orbitals involved in the single-electron excitation, respectively. This expression is the result of adding a correlation correction to the uncorrelated S_1-T_1 splitting. In the following, we briefly summarise how this result is derived.

For a non-interacting system, the S_1-T_1 excitation-energy difference is

$$\Delta E^0_{\mathrm{ST}} = \frac{1}{2}\int\int d^3\mathbf{r}_1 d^3\mathbf{r}_2 \frac{\Delta\Pi^0_{\mathrm{ST}}(\mathbf{r}_1,\mathbf{r}_2)}{r_{12}}, \tag{4.2}$$

where $\Delta\Pi^0_{\mathrm{ST}}(\mathbf{r}_1,\mathbf{r}_2)$ is the non-interacting pair-density difference between the S_1 and T_1 states:

$$\Delta\Pi^0_{\mathrm{ST}}(\mathbf{r}_1,\mathbf{r}_2) = 4\phi_i(\mathbf{r}_1)\phi_f(\mathbf{r}_1)\phi_i(\mathbf{r}_2)\phi_f(\mathbf{r}_2). \tag{4.3}$$

Substituting eq. 4.3 into eq. 4.2, one obtains

$$\Delta E^0_{\mathrm{ST}} = 2\int\int d^3\mathbf{r}_1 d^3\mathbf{r}_2 \frac{\phi_i(\mathbf{r}_1)\phi_f(\mathbf{r}_1)\phi_i(\mathbf{r}_2)\phi_f(\mathbf{r}_2)}{r_{12}} = 2H_{12}. \tag{4.4}$$

A correlation correction, $\Delta E^{\mathrm{corr}}_{\mathrm{ST}}$, must be added to ΔE^0_{ST} to recover the correlated S_1-T_1 splitting, ΔE_{ST}:

$$\Delta E_{\mathrm{ST}} = \Delta E^0_{\mathrm{ST}} + \Delta E^{\mathrm{corr}}_{\mathrm{ST}}. \tag{4.5}$$

$\Delta E^{\mathrm{corr}}_{\mathrm{ST}}$ consists of kinetic and potential energy contributions:

$$\Delta E^{\mathrm{corr}}_{\mathrm{ST}} = \Delta T^{\mathrm{corr}}_{\mathrm{ST}} + \Delta V^{\mathrm{corr}}_{\mathrm{ST}}. \tag{4.6}$$

The quantum virial theorem states that, for a system at equilibrium, its kinetic (T) and potential (V) energies have the simple relation $2T = -V$. This theorem is valid for both the ground and excited states. It also equally applies to both the correlated and uncorrelated systems. Therefore, this theorem can be used to simplify eq. 4.6

and write

$$\Delta E_{\mathrm{ST}}^{\mathrm{corr}} = \frac{1}{2}\Delta V_{\mathrm{ST}}^{\mathrm{corr}}. \tag{4.7}$$

Becke argued[100] that electron correlation would have the effect of "smoothing out" the S_1-T_1 non-interacting pair-density difference (eq. 4.3), reducing it to zero everywhere. Correlation would then lower the potential energy of the S_1 state, relative to the T_1 state, by $\Delta V_{\mathrm{ST}}^{\mathrm{corr}} = -2H_{12}$. Thus,

$$\Delta E_{\mathrm{ST}}^{\mathrm{corr}} = -H_{12} \tag{4.8}$$

and substitution into eq. 4.5 gives the correlated S_1-T_1 splitting,

$$\Delta E_{\mathrm{ST}} = 2H_{12} - H_{12} = H_{12}, \tag{4.9}$$

which is the result in eq. 4.1.

The S_1 energy, E_{S_1}, and the corresponding excitation energy, $\Delta E_{0\mathrm{S}} = E_{S_1} - E_{S_0}$, can therefore be obtained from the energies of the S_0 and T_1 states and the H_{12} integral by

$$E_{S_1} = E_{T_1} + H_{12}, \tag{4.10a}$$

$$\Delta E_{0\mathrm{S}} = E_{T_1} + H_{12} - E_{S_0} = E_{0\mathrm{T}} + H_{12}, \tag{4.10b}$$

where $\Delta E_{0\mathrm{T}} = E_{T_1} - E_{S_0}$ is the triplet excitation energy. To evaluate $\Delta E_{0\mathrm{S}}$, the virial exciton model requires the energy of the S_0 state, as well as a restricted-open-shell (RO) calculation for the T_1 state. The calculation must be RO in order to uniquely define ψ_i and ψ_f.

4.3 Computational Details

The geometries of the four TCNE-aromatic dimers (B3LYP/cc-pVDZ),[213] and DMABN (B3LYP/6-31G*)[216] were taken from the literature. The geometries of p-NA and DAN were optimized using B3LYP/6-311G(d,p), consistent with Ref. 215. The C_2H_4-C_2F_4 dimer geometry (C_{2v} symmetry) was optimized using B3LYP/6-31+G* at a fixed intermolecular separation of 4 Å. This intermolecular separation, R, was defined by the distance between the midpoints of the two C=C bonds, as

Figure 4.2: Calculated S_1 excitation energy (E_{0S}) as a function of the intermolecular separation, R, for the C_2H_4-C_2F_4 dimer. The B3LYP functional was used for both the TDDFT and virial exciton model calculations.

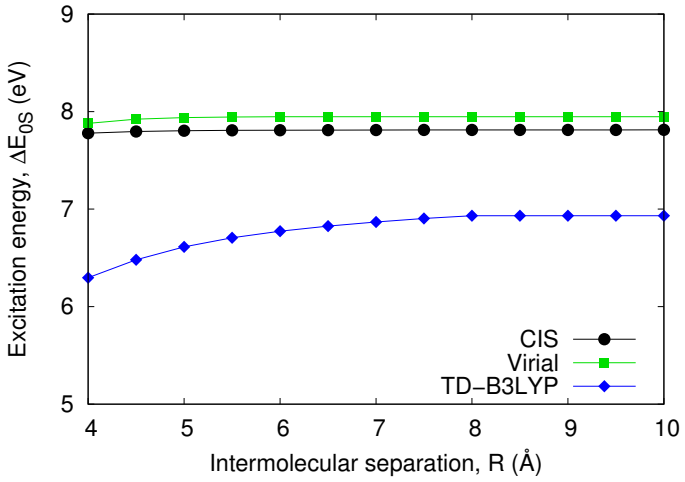

shown in Figure 4.1, and was varied from 4.0 to 10.0 Å in 0.5 Å increments. Ground-state, unrestricted and RO triplet-state, and TDDFT single-point calculations, were performed on the optimized geometries of all species using B3LYP[90]/cc-pVTZ. Configuration interaction singles (CIS)[217] calculations were also performed using the cc-pVTZ basis set for the C_2H_4-C_2F_4 dimer. The Gaussian 09 package[175] was employed throughout. An in-house "postG" program was used to compute the H_{12} integrals employing the numerical method of Becke and Dickson.[218]

4.4 Results and Discussion

4.4.1 C_2H_4-C_2F_4: A Classic CT Test

We first apply the virial exciton model to the C_2H_4-C_2F_4 intermolecular dimer,[119] which is an established test of CT-excitation errors. The S_1 excitation energy was calculated for a range of intermolecular separations with the virial exciton model, TD-B3LYP, and CIS. The results are shown in Figure 4.2.

CIS theory, which will serve as our benchmark, predicts a localized $\pi \rightarrow \pi^\star$ transition on the ethylene molecule as the lowest-energy singlet excitation. In contrast, various TDDFT calculations erroneously predict the intermolecular CT

state to lie lower in energy.[95,119] This causes TD-B3LYP to drastically underestimate the S_1 excitation energy over the entire range of intermolecular separations. Moreover, because the TD-B3LYP S_1 excitation has CT character, the excitation energy shows a strong dependence on the intermolecular distance, as seen in Figure 4.2. Conversely, the lowest-energy triplet excitation is localized on the ethylene molecule and is of $\pi \rightarrow \pi^\star$ character. As a result, the virial exciton model is in good agreement with CIS over the entire range of intermolecular separations and does not share the same CT breakdown displayed by TD-B3LYP.

Calculations were also attempted on the bacteriochlorin-zincbacteriochlorin (ZnBC-BC) intermolecular dimer, which is the second complex popularized as a demonstration of CT error.[95] However, due to the near degeneracy of the first three excited states,[95] we have not yet been able to converge the RO triplet calculations required for the virial exciton model.

4.4.2 TCNE-Aromatic Dimers and Push-Pull Dye Molecules

We now turn to a set of systems for which the S_1 excitation does correspond to a CT state. The S_1 excitation energies were computed for four TCNE-aromatic CT dimers and three donor-acceptor molecules featuring intramolecular CT excitations. The resulting excitation energies, and related quantities required for the virial exciton model, are tabulated in Table 1. The S_1 excitation energies are compared to experimental or high-level theoretical reference values.[213,215,216]

To verify that the T_1 excited states in question indeed possess CT character, we computed density differences relative to the S_0 ground state. The results are presented in Figure 4.3. For each of the four TCNE-aromatics dimers, notable intermolecular CT is observed, with the electron density shifting from the aromatic moiety to the TCNE molecule. DMABN, p-NA, and DAN all show typical intramolecular, push-pull CT from the electron-donating to the electron-withdrawing substituent.

Returning to Table 4.1, the S_1-T_1 energy splitting, given by the H_{12} integral, ranges from 1.1-1.7 eV for these systems. One might expect a vanishing H_{12} integral for CT excitations, as the ground-state frontier orbitals will be localised on either the donor or acceptor moieties and will consequently have negligible overlap. However, this is not the case, as the two singly-occupied molecular orbitals in the RO triplet

Table 4.1: Calculated excitation energies, and related quantities, in eV. Absolute errors from the literature reference values ($\Delta E_{0S}^{\mathrm{Ref.}}$) are given in parentheses. Tabulated values are: the unrestricted and restricted T_1 excitation energies ($\Delta E_{0T}^{\mathrm{U}}$ and $\Delta E_{0T}^{\mathrm{RO}}$), the H_{12} integral, the unrestricted and restricted S_1 excitation energies ($\Delta E_{0S}^{\mathrm{U}}$ and $\Delta E_{0S}^{\mathrm{RO}}$), and the TD-B3LYP S_1 excitation energies ($\Delta E_{0S}^{\mathrm{TD}}$).

System	$\Delta E_{0T}^{\mathrm{U}}$	$\Delta E_{0T}^{\mathrm{RO}}$	H_{12}	$\Delta E_{0S}^{\mathrm{U}}$	$\Delta E_{0S}^{\mathrm{RO}}$	$\Delta E_{0S}^{\mathrm{TD}}$	$\Delta E_{0S}^{\mathrm{Ref.}}$
TCNE-benzene	2.27	2.41	1.55	3.82 (0.23)	3.96 (0.37)	1.91 (-1.68)	3.59[213]
TCNE-toluene	2.21	2.33	1.30	3.51 (0.15)	3.63 (0.27)	1.74 (-1.62)	3.36[213]
TCNE-o-xylene	2.14	2.25	1.12	3.26 (0.11)	3.37 (0.22)	1.48 (-1.67)	3.15[213]
TCNE-naphthalene	1.61	1.72	1.10	2.71 (0.11)	2.82 (0.22)	0.81 (-1.79)	2.60[213]
DMABN	3.33	3.41	1.66	4.99 (0.27)	5.07 (0.35)	4.31 (-0.41)	4.72[216]
p-NA	3.12	3.17	1.46	4.58 (0.19)	4.63 (0.24)	3.50 (-0.89)	4.39[215]
DAN	2.91	2.97	1.37	4.28 (0.34)	4.34 (0.40)	3.19 (-0.75)	3.94[215]
MAE				0.20	0.29	1.26	–

calculations are delocalised over both moieties and have substantial overlap.

Table 4.1 shows that TD-B3LYP drastically underestimates the CT excitation energies, as expected, with a MAE of 1.26 eV. For all seven systems, the virial exciton model provides significantly more accurate CT excitation energies than TD-B3LYP, with a MAE of 0.29 eV. An even lower MAE of 0.20 eV can be achieved by adding H_{12} (which must be computed from the RO triplet orbitals) to the *un*restricted T_1 excitation energy. Contrary to the typical underestimation by TDDFT methods, the virial exciton model systematically overestimates the CT excitation energies in Table 4.1. This is possibly a result of using the cc-pVTZ basis set, which lacks diffuse functions. The CT nature of the present excitations results in anionic moieties in the excited states, which will be preferentially stabilised by the addition of diffuse functions. Unfortunately, the RO triplet calculations are somewhat difficult to converge with the present basis set, and addition of diffuse functions greatly exacerbates the problem. This emphasizes the importance of improving self-consistent-field algorithms for RO calculations, as one must be able to efficiently converge to the correct triplet state before applying the virial correction. Regardless, the performance of the virial exciton model is impressive and confirms that it does not suffer from the same intrinsic CT errors as TDDFT.

Figure 4.3: Computed T_1-S_0 density differences for the TCNE-aromatic dimers and donor-acceptor molecules. Violet (green) isosurfaces represent an increase (decrease) in electron density in the T_1 state relative to the S_0 state. The isovalues are ± 0.001 a.u.

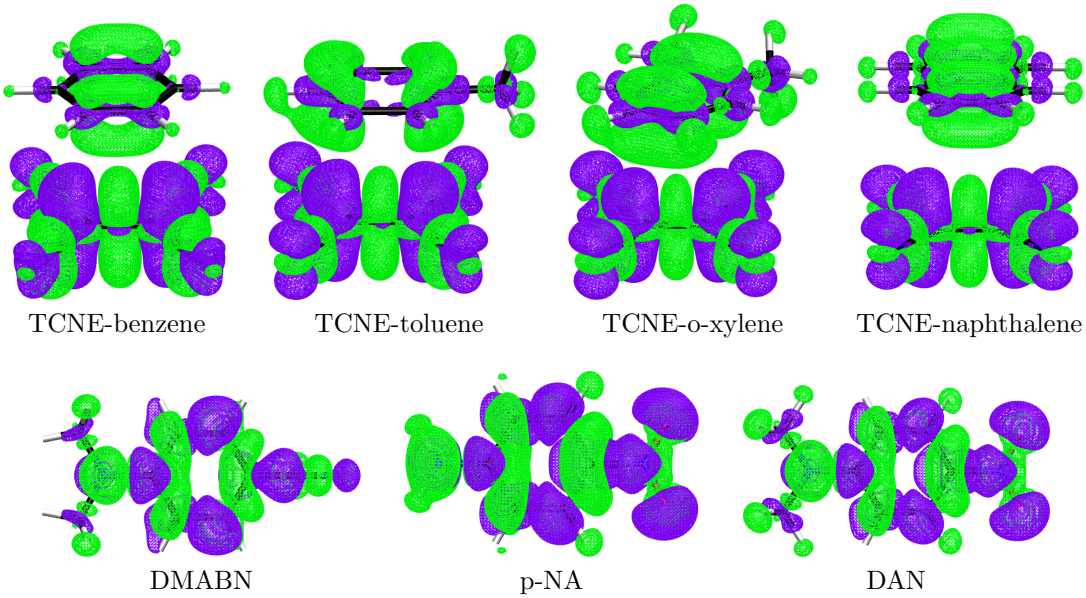

4.5 Conclusions

In this work, the accuracy of Becke's virial exciton model was assessed for CT excitation energies. The results demonstrate that the model is free of the systematic CT errors that plague conventional TDDFT methods. For a benchmark set consisting of four intermolecular TCNE-aromatic dimers and three donor-acceptor molecules, the virial exciton model achieves an overall MAE of 0.29 eV (or 0.20 eV using unrestricted T_1 energies) compared to literature reference data, significantly improving upon the accuracy of the widely used TD-B3LYP method. This error is roughly on par with the MAE of 0.26 eV previously obtained[100] for Thiel's small-molecule excitation data set.[124] We therefore conclude that the virial exciton model can be reliably used to predict S_1 excitation energies in molecular systems, even for excitations with CT-character. See, also, the very recent application of the model to computation of the optical gap in polyacetylene.[219]

Chapter 5

A Novel Computational Methodology for Modeling Solid-State Excitations: Design and Initial Testing

5.1 Design of the Computational Framework

It is our intention to design a fully *ab initio* (i.e. first-principles) computational methodology. The underpinning theoretical method is ground-state KS-DFT, which is carried out via a combination of the PW-PAW implementation of periodic-boundary calculations on the crystalline solid and non-periodic calculations on isolated molecules. The various stages of calculations are described in detail in the following subsections.

5.1.1 Solid-State Calculations: The Ground State

We start by extracting the experimental crystal structures of our chromophores of interest from the Cambridge Crystallographic Data Centre (CCDC).[196] The first step of the calculations is to optimize the geometry of the crystal unit cell using periodic-boundary DFT with the PAW formalism, implemented in the Quantum ESPRESSO (QE) program.[101] In order to accurately model the intermolecular interactions in the crystal structure, we use the well-tested B86bPBE exchange-correlation functional[88,107] in conjunction with the XDM dispersion correction model.[104] B86bPBE-XDM has been found to yield an optimal description of non-covalent interactions in solids.[154]

5.1.2 Solid-State Calculations: The First Triplet State

After obtaining the optimized ground-state geometric structure and ground-state energy, E_0^{crystal}, we model the first triplet-state energy of the crystal. An initial spin-magnetization bias[220] is assigned to one molecule within the unit cell to let the SCF calculation converge to the first triplet excited state, with energy $E_{\text{T}}^{\text{crystal}}$. The first triplet excitation energy of the crystal is then

$$E_{0\text{T}}^{\text{crystal}} = E_{\text{T}}^{\text{crystal}} - E_0^{\text{crystal}}. \tag{5.1}$$

To model the emission process, we allow relaxation of the atomic positions in the unit cell during the spin-magnetization calculation. The relaxed triplet excited state corresponds to the state at the initiation of the photonic emission.

5.1.3 Gas-Phase Calculations

Having optimized the ground-state crystal structure, we select a single moiety in the crystal unit cell to model the singlet excitation. This moiety could be either a single molecule or a charge donor-acceptor dimer, depending on the nature of the singlet excitation being modeled, and is excised from the crystal structure using the critic2 program.[197,221] Gas-phase Gaussian 09[175] single-point energy calculations are then performed on both the ground and first triplet states of the excised moiety. The restricted open-shell (RO) formalism is used for the first triplet state and the .wfn (wavefunction) file is written at the end of the SCF procedure to obtain orbitals for the singlet-triplet energy splitting. Additionally, the spin-density distribution obtained for the first triplet state can be used to determine the initial magnetic biases to be assigned to each atom of the excited moiety in the aforementioned solid-state calculations.

5.1.4 Determination of the First Singlet Excitation Energy

Finally, we apply Becke's virial exciton model to calculate the energy splitting between the T_1 and S_1 excited states of the excised molecular moiety, $\Delta E_{\text{ST}}^{\text{mol}}$. The calculation of $\Delta E_{\text{ST}}^{\text{mol}}$ (i.e. Eq. 2.46) is performed numerically using the method of Becke and Dickson[218] via an in-house "postG" code. The expansion of the HOMO and LUMO orbitals in terms of the Gaussian basis functions, contained

in the wavefunction (.wfn) files written during the RO triplet-state calculations, are required as input. We assume that the crystal environment affects both the first singlet and triplet excited states very similarly, such that

$$\Delta E_{\mathrm{ST}}^{\mathrm{mol}} \approx \Delta E_{\mathrm{ST}}^{\mathrm{crystal}}. \tag{5.2}$$

Such an assumption should be valid, as photon-induced single-electronic excitations generally produce very similar total electron densities for the lowest singlet and triplet excited states,[222–224] which differ from each other by a mere spin-flip of the excited electron. Given this key assumption, $\Delta E_{\mathrm{ST}}^{\mathrm{mol}}$ can be used to recover the first singlet-excitation energy in the crystal:

$$E_{0\mathrm{S}}^{\mathrm{crystal}} = E_{0\mathrm{T}}^{\mathrm{crystal}} + \Delta E_{\mathrm{ST}}^{\mathrm{crystal}} \approx E_{0\mathrm{T}}^{\mathrm{crystal}} + \Delta E_{\mathrm{ST}}^{\mathrm{mol}}. \tag{5.3}$$

Lastly, it is useful to note that Becke's scheme was conceptualized for isolated molecular systems with localized molecular orbitals. This makes its direct application to simple inorganic solids (such as silicon and diamond) with fully delocalized electronic energy bands infeasible. Despite this, we are confident that Becke's scheme is perfectly transferable to calculating the T_1-S_1 splitting for molecular crystals. Unlike periodic inorganic solids, where the entire material is connected via covalent bonds, distinct molecular moieties can be clearly identified in organic molecular crystals. These constituent moieties are held together via non-covalent intermolecular interactions and, consequently, they have significant degrees of autonomy. Thus, the electronic orbitals closely resemble those of isolated gas-phase molecules and remain highly localized around their respective constituent molecules in the crystal lattice. This high similarity in terms of orbital localization supports the virial exciton model's transferability from gas-phase molecules to molecules within organic solids.

5.2 Preliminary Tests on Ethylene and Nucleobase Crystals

Our first task is to test the viability and the robustness of the proposed methodology. To provide a proof-of-concept, we have chosen five simple crystals with archived structures[225,226] to carry out preliminary calculations: ethylene, thymine, cytosine, adenine, and uracil, the molecular structures of which are shown in Figure 5.1. Ethylene is chosen for the obvious reason of simplicity, allowing for fast testing of the computational scheme. The four nucleobases, while still possessing moderate unit-cell sizes, feature strong hydrogen bonding in the crystalline phase. This is of particular interest as we aim to quantify the effect of the intermolecular interactions in the crystalline environment on the excitation energies.

Figure 5.1: The systems chosen for the preliminary tests. The CCDC[196] codes for their crystal structures are labeled in the parentheses. The ethylene crystal structure was extracted from the Crystallography Open Database (COD).[225]

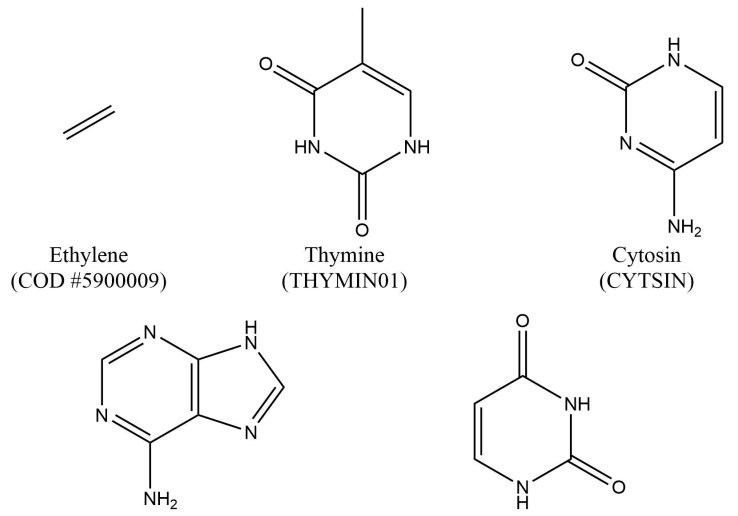

Specific goals for these preliminary tests are: (i) to demonstrate that the predicted first triplet (and therefore the first singlet) excitation energies of the crystals converge with increasing unit cell sizes and (ii) to quantify the effect of the crystalline environment on the first singlet excitation energies of the tested systems.

Preliminary calculations were performed for both the crystals and excised

molecules of ethylene and the four nucleobases (A, T, C, U). QE periodic-boundary calculations used the B86bPBE-XDM method with $E_{\mathrm{cut,wfn}} = 60$ Ry and $E_{\mathrm{cut},\rho} = 600$ Ry. Gaussian 09 calculations on the excised molecules used the B3LYP functional and the cc-pVTZ basis set.[227] Becke's virial exciton model was used to correct the crystalline-phase first triplet excitation energies towards the first singlet excitation energies.

5.2.1 Super-Cell Size Effect

We first probed the effect of super-cell size on the first triplet excitation energy ($E_{0\mathrm{T}}^{\mathrm{crystal}}$) of our test crystals. After ground-state optimizations, the original $1 \times 1 \times 1$ unit cells were replicated to form $N_x \times N_y \times N_z$ super cells, where N_x, N_y and N_z denote the numbers of replications in the x, y, and z directions, respectively. Initial-magnetization biases were assigned to one molecule in each super-cell expansion and the first triplet excitation energy was then calculated according to eq. 5.1. The results are presented in Table 5.1.

It is clear from the results that variations in $E_{0\mathrm{T}}^{\mathrm{crystal}}$ with respect to the super-cell size are minimal, being well under 0.1 eV in magnitude in the vast majority of cases. This implies that the interactions of the triplet-excited molecule with its translated images in neighboring super cells have a negligible effect on $E_{0\mathrm{T}}^{\mathrm{crystal}}$. The density differences between the ground and first triplet states were visualized for the excised molecules and crystals of all cell sizes using the VMD program.[228] For the outliers with a $E_{0\mathrm{T}}^{\mathrm{crystal}}$ shift greater than 0.1 eV, the density differences corresponded to a delocalized triplet state in the crystal. Such a delocalized triplet state was also found for the $1 \times 1 \times 3$ super cell of uracil, even though its $E_{0\mathrm{T}}^{\mathrm{crystal}}$ only deviates from the $1 \times 1 \times 1$ unit cell by less than 0.03 eV. These results indicate that, in future crystalline-phase calculations, using the $1 \times 1 \times 1$ unit cell should be adequate as the cell size has a negligible effect on $E_{0\mathrm{T}}^{\mathrm{crystal}}$.

Density-difference plots for all $1 \times 1 \times 1$ unit cells are shown in Figure 5.2 and compared with the results for the excised molecules. The density-difference plots for the three super cells possessing a delocalized triplet state are shown in Figure 5.3. Overall, our magnetized, solid-state calculations were able to converge to first triplet states that highly resemble the gas-phase RO triplet-state results, confirming the validity of our approach. Meanwhile, we should be mindful of the

Figure 5.2: Density differences between the ground and first triplet states: $1 \times 1 \times 1$ unit cells (left) vs excised molecules (right). The purple (green) isosurfaces represent regions with increased (decreased) electron density in the first triplet state. The density isovalues are +/-0.005 a.u. for all cases except for ethylene, where +/- 0.01 au. are used. Coloring scheme: C, black; H, gray; N, blue; O, red. The unit cells are delineated by the red boxes. Cell orientations have been adjusted for optimal views of the density differences.

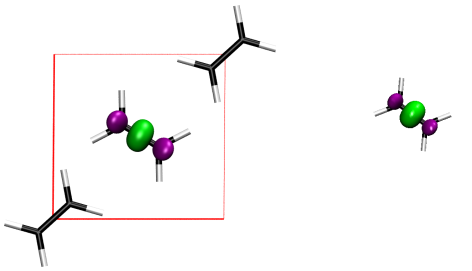

(a) ethylene

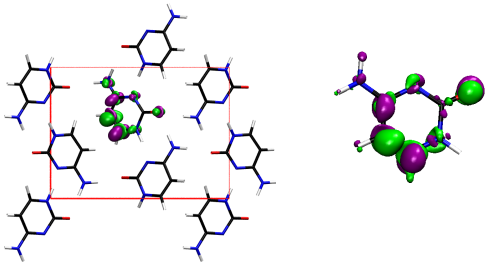

(b) cytosine

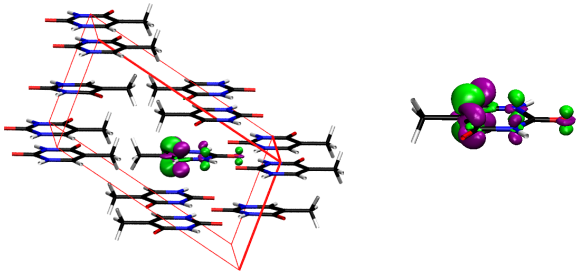

(c) thymine

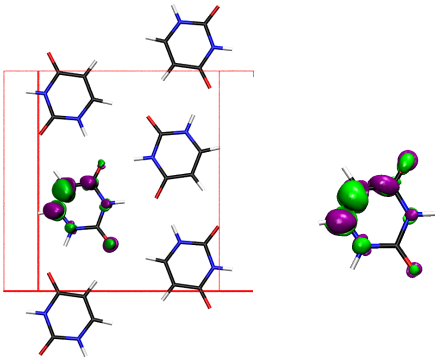

(d) uracil

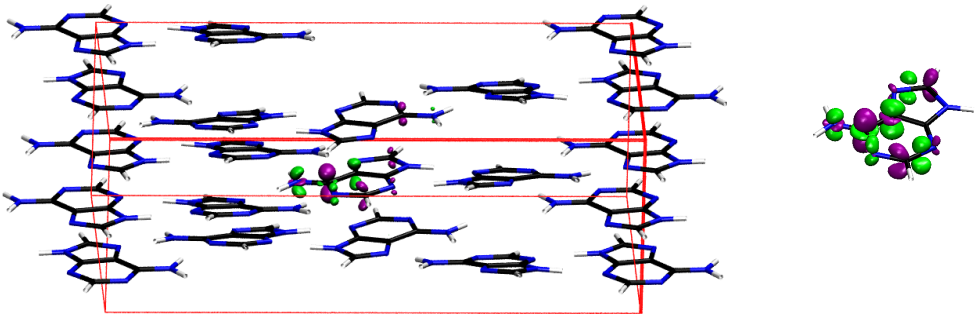

(e) adenine

Table 5.1: First triplet excitation energies calculated for various super-cell expansions of the test crystals. One molecule in each super cell was assigned an initial magnetic bias. $E_{0\mathrm{T}}^{\mathrm{crystal}}$ shift denotes the shift in the triplet excitation energy from that of the original $1 \times 1 \times 1$ cell. For super cells labeled with a $*$, a delocalized triplet state was obtained from the magnetized calculation. All energies are in eV.

Crystal	Super cell	$E_{0\mathrm{T}}^{\mathrm{crystal}}$	$E_{0\mathrm{T}}^{\mathrm{crystal}}$ shift
ethylene	$1 \times 1 \times 1$	4.42	0.00
	$1 \times 1 \times 2$	4.36	-0.06
	$1 \times 2 \times 1$	4.42	-0.00
	$2 \times 1 \times 1$	4.41	-0.01
	$1 \times 2 \times 2$	4.36	-0.07
	$2 \times 1 \times 2$	4.36	-0.07
	$2 \times 2 \times 1$	4.42	-0.00
	$2 \times 2 \times 2^*$	4.62	0.20
cytosine	$1 \times 1 \times 1$	3.50	0.00
	$1 \times 1 \times 2$	3.51	0.01
	$1 \times 1 \times 3$	3.50	0.00
adenine	$1 \times 1 \times 1$	3.15	0.00
	$1 \times 1 \times 2$	3.13	-0.02
	$2 \times 1 \times 1$	3.12	-0.03
thymine	$1 \times 1 \times 1$	3.32	0.00
	$1 \times 1 \times 2^*$	3.44	0.12
	$1 \times 2 \times 1$	3.32	0.00
	$2 \times 1 \times 1$	3.32	0.00
	$1 \times 2 \times 2$	3.32	0.00
uracil	$1 \times 1 \times 1$	3.46	0.00
	$1 \times 1 \times 2$	3.41	-0.05
	$1 \times 1 \times 3^*$	3.43	-0.03

potential inconsistency between the first triplet states obtained from the crystalline- and gas-phase calculations due to charge delocalization in the extended crystal lattice, although we expect the effect of such charge delocalization on $E_{0\mathrm{T}}^{\mathrm{crystal}}$ to remain minor for systems of practical interest. Excessive charge delocalization is a common artifact of the GGA density functionals,[183,185,229,230] including B86bPBE.

5.2.2 Quantification of Crystalline-Environment Effects

We quantified the effect of the crystalline environment on $E_{0\mathrm{T}}$ for our test crystals to gauge its relative significance. This was achieved by performing additional PW-PAW calculations on the excised molecules by placing them in a very large cubic unit

Figure 5.3: Density differences between the ground and first triplet states for super cells that converged to a delocalized first triplet state. The purple (green) isosurfaces represent regions with increased (decreased) electron density in the first triplet state. The density isovalues are +/-0.002 a.u. for all cases. Coloring scheme: C, black; H, gray; N, blue; O, red. The unit cells are delineated by the red boxes. Cell orientations have been adjusted for optimal views of the density differences.

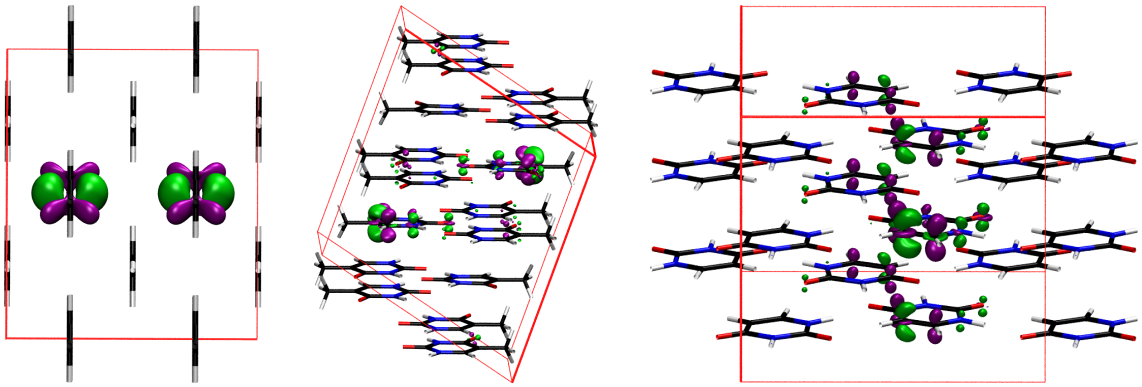

(a) ethylene ($2\times2\times2$) (b) thymine ($1\times1\times2$) (c) uracil ($1\times1\times3$)

cell comprised mostly of vacuum. The sizes of vacuum cells were chosen such that the total ground-state energy was converged to within 0.001 eV and correspond to $30\times30\times30$ Å^3 for ethylene and $40\times40\times40$ Å^3 for the nucleobases. The calculated first triplet excitation energies of the isolated molecules in vacuum, $E_{0\mathrm{T}}^{\mathrm{vacuum}}$, were compared to the $E_{0\mathrm{T}}^{\mathrm{crystal}}$ values. The results are presented in Table 5.2.

Table 5.2 shows that, while rather small in magnitude, the effect of crystalline environment on $E_{0\mathrm{T}}$ is non-trivial. This is especially true for the nucleobases featuring strong intermolecular H-bonding, where the absolute values of $E_{0\mathrm{T}}^{\mathrm{crystal}} - E_{0\mathrm{T}}^{\mathrm{vacuum}}$ can be as large as 0.3 eV. Also intriguing is that the crystalline environment can shift the $E_{0\mathrm{T}}$ values either higher or lower, which potentially indicates a competition between H-bonding and other intermolecular interactions within the crystalline environment. One can reasonably expect that the relative significance of the crystalline-environment effect will manifest to greater degrees in cases such as polymorphs and co-crystals, where intermolecular interactions are likely the primary driving force behind the subtle shifts in the absorption/emission spectra.

The first singlet excitation energies, $E_{0\mathrm{S}}^{\mathrm{crystal}}$, for the $1\times1\times1$ unit cells of ethylene and the four nucleobases were calculated using Eq. 5.3. The results are presented in Table 5.3. Unfortunately, we are unable to assess the quality of our $E_{0\mathrm{S}}^{\mathrm{crystal}}$

Table 5.2: Quantification of the crystalline-environment effect on $E_{0T}^{crystal}$. The differences between the first triplet excitation energies in the crystal and vacuum, $E_{0T}^{crystal} - E_{0T}^{vacuum}$, are used to indicate the magnitude of the crystalline-environment effect. All energies are in eV.

Crystal	E_{0T}^{vacuum}	$E_{0T}^{crystal}$	$E_{0T}^{crystal} - E_{0T}^{vacuum}$
ethylene	4.47	4.42	-0.05
cytosine	3.34	3.50	0.16
adenine	3.44	3.15	-0.29
thymine	3.26	3.32	0.06
uracil	3.35	3.46	0.11

Table 5.3: The first singlet excitation energies ($E_{0S}^{crystal}$) calculated for the $1 \times 1 \times 1$ unit cells of the test crystals using Becke's scheme. ΔE_{ST}^{mol} denotes the energy gap between the first triplet and singlet excited states of the excised molecules. All energies are in eV.

Crystal	$E_{0T}^{crystal}$	$E_{0S}^{crystal}$	ΔE_{ST}^{mol}
ethylene	4.42	7.76	3.34
cytosine	3.50	4.78	1.28
adenine	3.15	4.77	1.62
thymine	3.32	5.21	1.89
uracil	3.46	5.34	1.88

predictions due to the lack of experimental/theoretical benchmark values for the crystals involved in these preliminary tests. In Chapters 6 and 7, we apply the same approach to more crystals with experimentally measured absorption or emission energies to benchmark its predictive accuracy.

Chapter 6

Computational Modeling of Piezochromism in Molecular Crystals

The work presented in this current chapter has been published as an article: Xibo Feng, Axel D. Becke, and Erin R. Johnson, *Computational Modeling of Piezochromism in Molecular Crystals*, J. Chem. Phys. **152**, 234106 (2020).

Synopsis: Piezochromic materials, whose luminescence responds to external pressure, have recently garnered much experimental attention. Computational modeling of piezochromism is of high theoretical interest, yet currently lacking. Herein, we present a computational effort to predict the piezochromism for a selection of molecular crystals. The current methodology employs a combination of dispersion-corrected solid-state and gas-phase density-functional theory (DFT), and Becke's virial exciton model. Our study finds that piezochromism is primarily driven by the modification of intermolecular interactions within the molecular crystal and can be understood from the perspectives of changing polarizability or band gaps upon the application of mechanical pressure.

6.1 Introduction

Piezochromism[231] refers to changes in the photoluminescence (PL) wavelength and/or intensity of certain molecular crystals in response to the external stimulus of mechanical pressure (grinding or hydraulic pressure). Molecular crystals that

Figure 6.1: Molecular structures of the investigated piezochromic crystals, with their Cambridge Crystallographic Data Centre[196] (CCDC) identifiers included in parentheses. **1**: Tetrathiazolythiophene, **2**: boron diketonate, **3**: 2,7-diaryl-[1,2,4]triazolo[1,5-a]pyrimidine (2,7-diaryl-TAP). For **1**, two crystal structures were reported, one measured under ambient pressure (FIFGUY01), and the other (FIFGUY02) under 2.8 GPa of isotropic hydraulic pressure.[28]

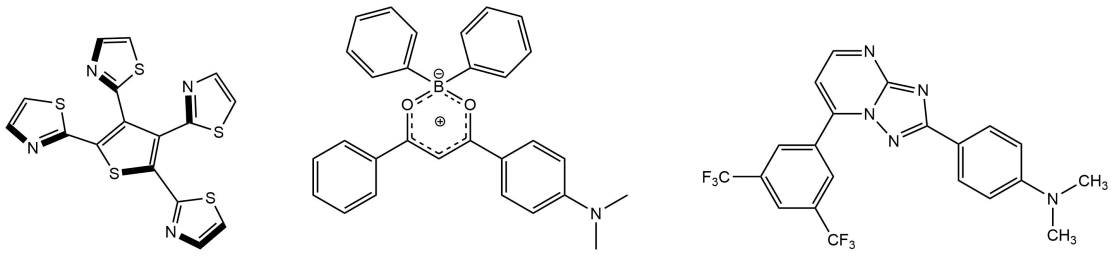

1 (FIFGUY01, FIFGUY02) **2** (XAPLUY) **3** (IXICUP)

display piezochromism have attracted considerable research attention, due to their potential applications in fields such as mechano-sensors,[232,233] memory devices,[234,235] and optoelectronics.[236,237] The potential utility of many piezochromic materials also lies in the fact they concurrently possess aggregation-induced emission[2,57] (AIE), meaning that their PL is significantly enhanced in the crystalline form relative to a dilute solution. It has been hypothesized that piezochromic behaviors could be induced when the inter- or intra-molecular environment within the crystal is modulated through the change in the crystal packing mode, or simply spatial constriction, when external pressure is applied.[238–240]

Computational investigation of piezochromism in molecular crystals is theoretically intriguing, as it represents a challenging case where the interplay of multiple inter- and intra-molecular factors might drive the modification of the electronic structure in the solid state, which is manifested by shifts in the crystals' luminescent properties. Despite much experimental effort to synthesize and characterize a variety of novel molecular crystals showing significant piezochromism,[26,238–243] theoretical modeling and rationalization of this phenomenon is currently limited.[244] We suspect that this is primarily due to complications in applying the popular time-dependent density-functional theory (TDDFT[45,46]) method to periodic solids.

Figure 6.1 shows the molecular structures of the three investigated molecular

Table 6.1: Experimental PL properties and piezochromism of the investigated molecular crystals. $\lambda_{\max}^{\text{emi}}$: emission maximum wavelength; ΔE^{emi}: emission energy.

Species	Ambient pressure		Highest pressure			Max. PL	Piezochromism	Ref.
	$\lambda_{\max}^{\text{emi}}$ (nm)	ΔE^{emi} (eV)	$P_{\max}$ (GPa)	$\lambda_{\max}^{\text{emi}}$ (nm)	ΔE^{emi} (eV)	shift (eV)	type	
1	556	2.23	3.20	609	2.04	0.19	Rev. red shift	28
2	585	2.14	5.77	660	1.88	0.26	Rev. red shift	29
3	524	2.37	14.5	676	1.83	0.53	Rev. red shift	30

crystals. Organic chromophores **1**,[28] **2**,[29] and **3**[30] have been previously synthesized and crystallized. These crystals' experimentally-observed PL properties and piezochromic behaviors are summarized in Table 6.1. Note that all three molecular crystals display a gradual red shift in the PL maximum wavelength under increasing isotropic hydraulic pressure. Such a red shift appears to be generally observed in the experimental literature. For the investigated crystals, this red shift is also reversible, *i.e.* the original PL maximum wavelength measured at ambient pressure is restored once the applied hydraulic pressure is removed.

6.2 Computational Methods

We employ a multi-step approach in this work involving standard density-functional theory (DFT) calculations on the target molecular crystals and on excised gas-phase molecular moieties. The crystals are modeled with the plane-wave formalism and projector augmented-wave[132] (PAW) atomic datasets. Computations are performed for the ground state (S_0) and the first excited triplet state (T_1), the latter using constrained magnetization to localize the excitation. A correction is then applied to the T_1 energy to obtain the first singlet (S_1) excited-state energy from gas-phase excised molecular calculations. The correction, or S_1-T_1 gap, is based on the virial exciton model of Becke[100] and the assumption that the excitation is localized on molecular sites in the crystal.

The S_1-T_1 gap is represented by the two-electron H_{12} integral (denoted as K_{if} in Ref. 100) and computed as the exchange integral involving the two singly occupied frontier orbitals of the molecular T_1 state:

$$H_{12} = \left\langle \phi_a(1)\phi_b(2) \left| \frac{1}{r_{12}} \right| \phi_a(2)\phi_b(1) \right\rangle . \tag{6.1}$$

The virial exciton model has the advantage of computational simplicity, while also eliminating errors seen with TDDFT for charge-transfer excitations.[245] It is assumed that the total electron densities in the T_1 and S_1 states are very similarly affected by the surrounding crystalline environment, so that the H_{12} value calculated in the gas phase for an extracted molecular moiety can be used to approximate the S_1-T_1 energy gap of the molecular crystal. Thus, the singlet excitation energy in the crystal can be approximated as

$$\Delta E_{0\mathrm{S}}^{\mathrm{cryst}} = \Delta E_{0\mathrm{T}}^{\mathrm{cryst}} + H_{12}^{\mathrm{mol}}, \tag{6.2}$$

where $\Delta E_{0\mathrm{T}}^{\mathrm{cryst}}$ is computed from periodic-boundary DFT and H_{12}^{mol} from finite-molecule calculations.

The virial exciton model itself also relies on the assumption that the T_1 and S_1 states have similar densities in the computation of the singlet-triplet splitting, H_{12}.[100] This assumption is based on the fact that the T_1 and S_1 states have identical orbital occupations, differing only in the spin of one electron, and is supported by the success of the model. One would expect the largest singlet-triplet density differences to occur for the smallest systems. The error introduced for the helium $1s2s$ singlet-triplet splitting is 0.20 eV,[100] and much smaller errors are expected for large organic molecules. Additionally, following our previous work,[246] the effect of excitation on the dispersion component of the lattice energy may be determined using the critic2 program.[197] The computed dispersion coefficients for a single ground-state molecule within the crystal lattice are replaced with the corresponding values for the T_1 or S_1 state, and the resulting intermolecular dispersion energy evaluated. The molecular excited-state densities were obtained from SCF calculations for T_1 and from TDDFT for S_1, and the dispersion coefficients evaluated using the postg program.[194] For the three compounds considered here, the T_1 state experiences slightly greater dispersion interactions within the crystal; however, the lattice-energy differences are extremely small (*viz.* 0.02-0.10 kcal/mol). This supports our assumption that the S_1 and T_1 states will experience sufficiently similar intermolecular interactions with the surrounding crystal lattice.

Figure 6.2 sketches the overall computational framework. We first optimized the S_0 geometries of the experimentally reported crystal structures, taken from the

Figure 6.2: The computational scheme employed in this work.

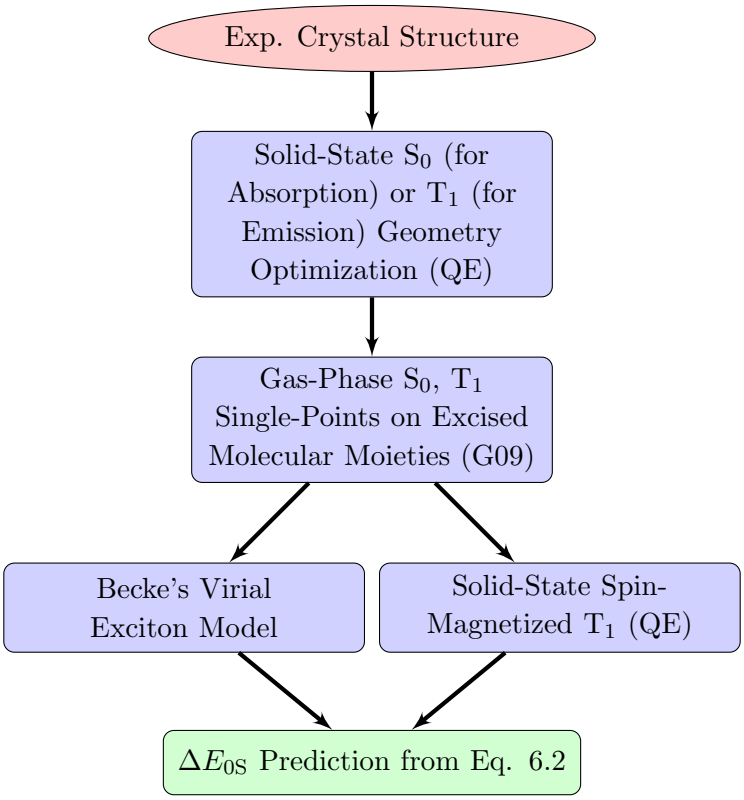

CCDC.[196] After the initial S_0 geometry optimizations, the crystal lattices were cut into (symmetry equivalent) molecular moieties using the critic2 program.[197] One single molecule was chosen, upon which single-point gas-phase calculations on the S_0 and T_1 (restricted open-shell, RO) states were performed. The resulting T_1 frontier orbitals were used to calculate the H_{12} integral. The initial spin-density biases used in the spin-magnetized calculation on the T_1 state in the crystal were then assigned based on the gas-phase RO spin-densities. To acquire the absorption energy, a single-point spin-magnetized T_1 calculation sufficed. For emission, spin-magnetized T_1 geometry optimization was performed, and the H_{12} integral was calculated again for the molecular moiety excised from the T_1-optimized crystal lattice.

All calculations on the molecular crystals were performed with the B86bPBE functional,[88,107] in conjunction with the exchange-hole dipole moment (XDM) model[102,103,154] dispersion correction. The Quantum ESPRESSO[101] (QE) package was used for these solid-state calculations. The `press` keyword was used to designate

the isotropic pressure applied to the crystal lattice. For all QE calculations, the well-converged $2 \times 2 \times 2$ Monkhorst-Pack[127] k-point mesh and planewave cutoff values of 80 and 800 Ry for the wavefunction and density, respectively, were used. All PAW datasets were generated via the `atomic` code by Dal Corso.[247] Gas-phase calculations on the molecular moieties were performed for the S_0 and restricted open-shell T_1 states with the B3LYP[90] (for **1** and **2**) and the BHandHLYP[248] (for **3**, due to B3LYP's failure in RO convergence) functionals, using the Gaussian 09 (G09) package.[175] Molecular polarizabilities were calculated for the S_0 and unrestricted T_1 states, with the B3LYP functional for all compounds, using the `polar` keyword. The Dunning-style cc-pVDZ basis set[227] was used for all G09 molecular calculations. An in-house program, which employs the numerical integration method of Becke and Dickson,[218] was used to calculate the H_{12} integrals.

6.3 Results and Discussion

6.3.1 Replication of Piezochromism

Applying our computational scheme, we obtained the absorption/emission energies for each crystal under a series of pressure values. The pressure ranges considered for the four crystal structures are: FIFGUY01/FIFGUY02 (**1**): 0.0-4.0 GPa (in 0.5 GPa increments); XAPLUY (**2**): 0.0-6.0 GPa (in 0.5 GPa increments); IXICUP (**3**): 0-15 GPa (in 1 GPa increments). The emission energies as functions of pressure are presented in Figure 6.3, with comparison to the experimental emission data extracted from literature.[28–30] Similar results were also obtained for the absorption energies versus pressure, as shown in the Supplementary Information. For each molecular crystal, red shift of the emission from the absorption is predicted for the entire pressure range, in agreement with the experimental observations.

Overall, our calculations were able to replicate the piezochromism of the modeled molecular crystals. As Figure 6.3 shows, the calculated emission energies red shift with increased external pressure for all four molecular crystals, which is consistent with the experimentally observed trends. Note that the calculated "compression curves" for the excitation energies are smooth. This suggests a gradual and reversible red shift of the excitation energy as the external pressure is increased within the calculated range, which also agrees with experimental observations. We point out

that the results for the two crystals of **1** (FIFGUY01 and FIFGUY02) are essentially identical, which indicates that the geometry optimizations correctly "linked" the two ends of the same reversible compression cycle.[28] Compression from the low-pressure structure and decompression from the high-pressure structure lead to identical piezochromic behavior; for this reason, we shall report only on FIFGUY01 in our further discussions.

Figure 6.3: Calculated emission energies (ΔE_{0S}^{emi}) versus applied pressure, decomposed into the triplet-excitation (ΔE_{0T}^{emi}) and the H_{12}^{mol} integral contributions. The triplet excitation energies for the excised molecules (ΔE_{0T}^{mol}) are also shown. The calculated results are compared to experimentally-measured emission energies under varying pressure (ΔE_{0S}^{exp}).

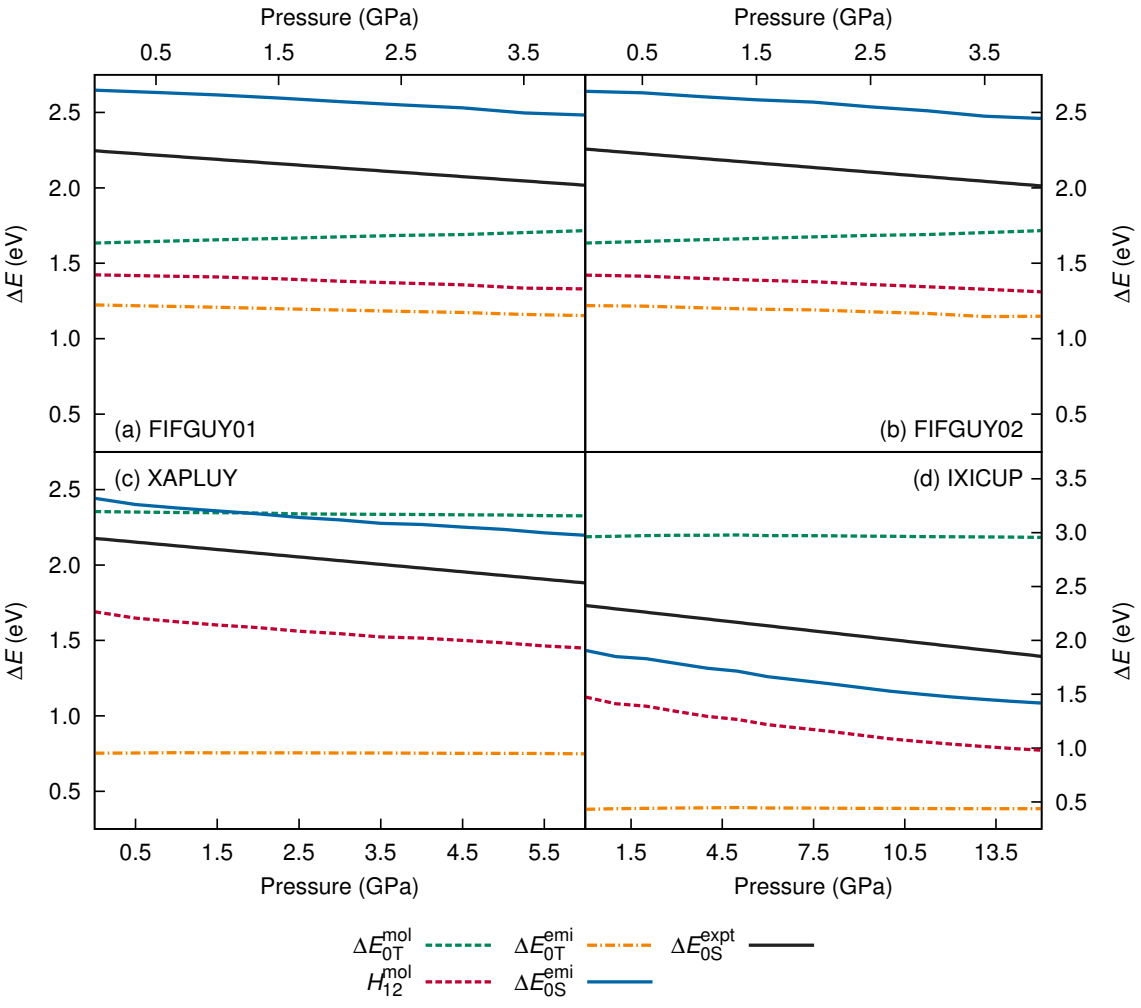

In terms of eV-accuracy, our predictions over-estimate the experimental emission

Table 6.2: Calculated emission piezochromism, showing both the total red shift (eV) and red shift per unit pressure (eV/GPa). Results, linearly fit and interpolated to match the full experimental pressure ranges, are shown for both the full calculations of the S_1 excitation energy (ΔE_{0S}^{emi}) and the T_1 band gaps (ΔE_{T1}^{gap}). The band-structure calculations correspond to the difference between valence and conduction band edges from the ground-state electronic configuration, using the T_1 geometries for each applied pressure. Experimental data are given for comparison.

Species	Total red shift			Shift per unit pressure		
	ΔE_{0S}^{emi}	ΔE_{T1}^{gap}	Expt.	ΔE_{0S}^{emi}	ΔE_{T1}^{gap}	Expt.
1	0.14	0.13	0.19	0.044	0.041	0.059
2	0.22	0.27	0.26	0.038	0.047	0.045
3	0.48	0.52	0.53	0.033	0.036	0.037

energies by *ca.* 0.40 eV for **1** and 0.25 eV for **2**, while an under-estimation by *ca.* 0.45 eV occurred for **3**. These errors are comparable to those previously obtained for three organic push-pull molecules (0.24-0.40 eV).[245] However, the relative changes in ΔE_{0S}^{emi} with pressure are in more impressive agreement with experiment. As shown in Table 6.2, the predicted magnitudes of the piezochromic red shifts and their pressure derivatives (*i.e.* the slopes of the emission compression curves) match very closely to the experimental data.

By decomposing our calculated singlet-excitation energies into the triplet-excitation and H_{12} integral contributions, as in Figure 6.3, it can be argued that the piezochromism of the investigated molecular crystals is driven by pressure-induced changes in the intermolecular interactions. For each compound in Figure 6.3, the values of the H_{12} integrals and intramolecular triplet excitation energies are nearly constant with respect to pressure. Thus, the overall piezochromic red shift is determined primarily from the solid-state triplet excitation energy. These results indicate the importance of properly accounting for the non-covalent, intermolecular interactions within the crystal lattice when modeling piezochromism.

6.3.2 Origin of the Universal Red Shift

One intriguing observation from both the experimental and calculated excitation-energy data is the consistent finding of a red shift with increased isotropic pressure. The fact that this red-shift behavior is shared by most other reported piezochromic molecular crystals in the experimental literature implies the universality of its origin.

We suggest that the piezochromic red shift can be rationalized from two different perspectives: molecular and solid-state.

Figure 6.4: Potential energy curves for the S_0 and S_1 states of the molecular crystals as functions of applied pressure.

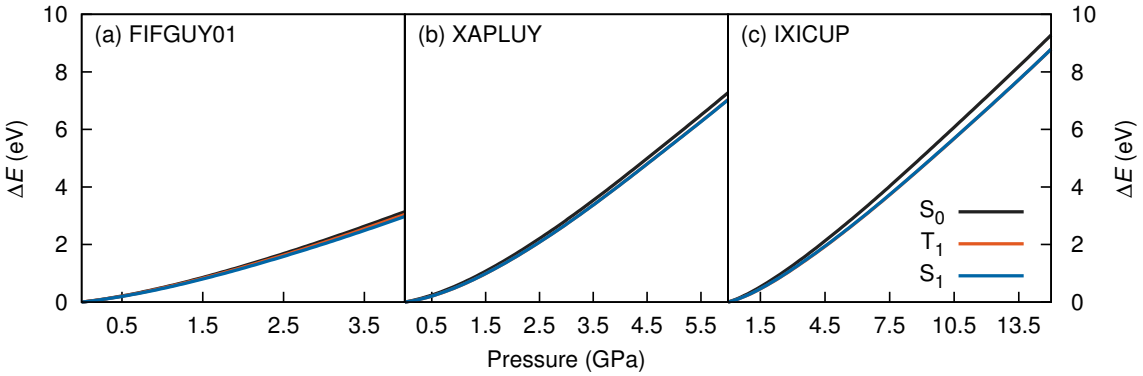

6.3.2.1 The Molecular Polarizability Perspective

From a molecular point of view, one might suspect that the piezochromic red shift could be caused by the difference in the response of the molecule in the ground or excited state to increasing pressure. The ground- and excited-state energies are each expected to increase with pressure due to confinement effects, as shown in Figure 6.4 (note that the S_1 curves are directly above the T_1 for XAPLUY and IXICUP). However, the energy of the ground state is raised to a larger degree than the excited states when the surrounding crystal lattice is compressed, reducing the excitation energy and leading to a pressure-induced red shift. This result can be explained if the excited-state molecule, which typically possesses a more diffuse electronic density than the ground state, is more able to polarize itself to adapt to increasing spacial constriction. Applied pressure increases Pauli repulsion between molecules. The densities of highly malleable (*i.e.* highly polarizable) molecules are better able to adjust themselves to avoid density overlaps and hence reduce Pauli repulsion. This reasoning is akin to a similar polarization argument made by Feng *et al.* in their experimental work.[240]

To validate the hypothesis of the excited states being more polarizable, we calculated the polarizabilities of the excised molecules in both S_0 and T_1 states. Results for both the zero-pressure absorption and emission geometries are summarized in

Table 6.3: Molecular S_0 and T_1 polarizabilities (in a.u.) calculated for the excised molecules at zero pressure, using the crystal geometries obtained for either the absorption or emission.

Species	S_0 Polarizability		T_1 Polarizability	
	Abs.	Emi.	Abs.	Emi.
1	301	327	381	372
2	390	393	591	588
3	303	310	508	500

Table 6.3. At zero pressure, the polarizability of the excised molecular moiety is significantly higher for the T_1 state than for the S_0 state of each species. The same trend holds for the full pressure ranges as well, albeit both the S_0 and T_1 polarizabilities decline slightly at higher pressures (see Supplementary Information). Thus, for the investigated species, the single molecule becomes more polarizable in the excited state, which induces the piezochromic red shift of the excitation energy via reduction of intermolecular repulsion. However, there is no direct correlation between the T_1-S_0 polarizability difference and the red shift per unit pressure, which is expected as the extent of compression will be highly anisotropic, depending on the molecular packing.

6.3.2.2 The Solid-State Band Structure Perspective

Alternatively, when one considers the entire crystal lattice, it is also of potential value to probe the effect of increased pressure on the calculated band structure. We might reasonably expect that external pressure will change (even if only slightly) the band gap of the compressed crystal. The crystal band gap is directly linked to the first-singlet excitation energy and the behavior of a molecular crystal's band gap under pressure could indicate its piezochromism. We hence conducted standard ground-state band-structure calculations for the investigated molecular crystals over the entire range of applied pressures. In each case, up to 6 bands above the conduction band edge were calculated. The resulting bands are extremely flat, as expected for molecular systems; representative band structures are shown in the Supplementary Information.

Figure 6.5 shows the variation in the valence and conduction band edges, which correspond to the highest-occupied and lowest-unoccupied bands, computed at the

Figure 6.5: Valence and conduction band edges, and band gaps, of the molecular crystals as functions of applied pressure, using the T_1 geometries.

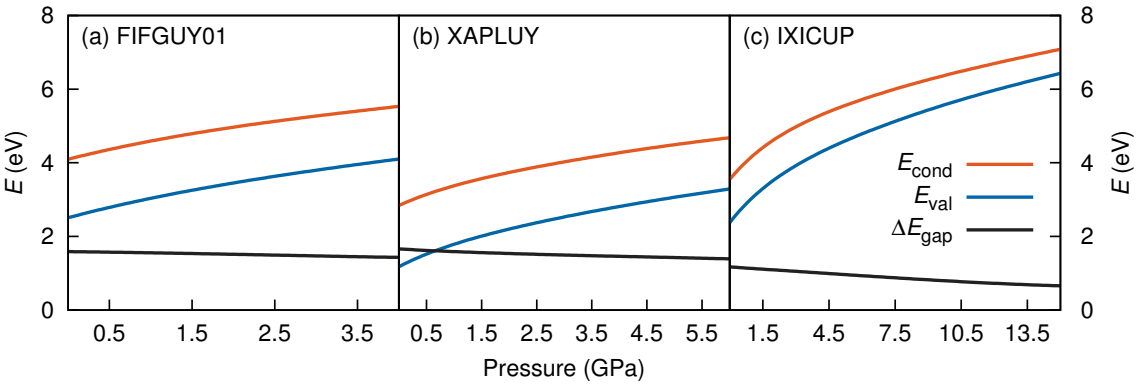

T_1 (emission) optimized geometries. These individual band energies both increase with pressure, due to molecular confinement. The crystal band gap values were extracted from the calculated band structure and are also plotted in Figure 6.5. The band gaps are consistently lower than the T_1 excitation energies obtained from the difference in self-consistent energies, as expected for the type of density-functional approximation used.[249–252] The band gaps for all three crystals smoothly decrease with pressure, in agreement with the observed piezochromism. The maximum emission red shifts are compared with the full computational results and the experimental data in Table 6.2. The red shifts in the band gap and in the full S_1 excitation energy with pressure are virtually identical for all three molecular crystals. Thus, we can view the pressure-induced closing of the band gap as driving piezochromism.

6.4 Conclusion

In this work, a novel computational scheme, combining solid-state and gas-phase DFT and Becke's virial exciton model, was proposed and applied to predict the piezochromism for a selection of molecular crystals. Our results indicate that the proposed method correctly captures the experimentally observed piezochromic red shifts. The magnitudes of the red shifts, and their rates of change with applied pressure, were predicted with impressive accuracy. Our calculations also revealed that the piezochromism observed for the investigated molecular crystals

is predominantly a result of pressure modulation of the intermolecular interactions within the crystal lattice. Further, theoretical insights into the origin of the universal piezochromic red shift were gained. We found that the piezochromic red shift could be rationalized from two perspectives: i) molecular, as the polarizability of the excited moiety consistently increases upon excitation, preferentially stabilizing the excited state upon compression; and ii) solid state, as closing of the crystal band gap under increasing pressure is consistently predicted. We hope that this work will contribute to the understanding of piezochromism and electronic excitations in molecular crystals in general, and aid the design of novel molecular crystals displaying PL properties of potential applicability.

Supplementary Material

The reader may consult Appendix A for supplementary material to this work, which includes: calculated absorption energies as functions of pressure; molecular polarizabilities for the S_0 and T_1 states as functions of pressure; valence and conduction band edges and band gaps as functions of pressure using the solid-state S_0 geometries; and representative zero-pressure band structures.

Chapter 7

Polymorph- and Coformer-Dependent Electronic Excitations in the Solid State: A Theoretical Perspective

The work presented in this current chapter has been published as an article: Xibo Feng, Axel D. Becke and Erin R. Johnson, *Theoretical Investigation of Polymorph- and Coformer-Dependent Photoluminescence in Molecular Crystals*, CrystEngComm **23**, 4264-4271 (2021).

Synopsis: Polymorph- and coformer-dependent photoluminescence (PL) are among the variety of novel solid-state PL phenomena recently observed in many molecular crystals. They are of particular research interest due to their direct connections to two heavily investigated topics in crystal engineering: polymorphism and cocrystalization. Herein, we apply a novel computational methodology, initially proposed and successfully applied in our previous investigation of piezochromism, to theoretical modeling of the polymorph- and coformer-dependent PL in the well-known ROY polymorphs and the recently synthesized 9-acetylanthracene (9-ACA) cocrystals, respectively. Our methodology offers satisfactory prediction of the experimentally observed color zoning for the ROY polymorphs and provides good qualitative and quantitative accuracy for the emission (fluorescence) energies of the 9-ACA cocrystals, although the results in both cases may be adversely affected by delocalization error in the density-functional methods employed. While the

polymorph-dependent PL in ROY is found to be controlled by the intramolecular geometry, modeling of the periodic crystal environment is necessary for accurate prediction of the coformer-dependent PL in the 9-ACA cocrystals, which is driven by charge transfer.

7.1 Introduction

Solid-state materials displaying photoluminescence (PL) have garnered significant research attention due to their wide range of potential applications in manufacture of solar cells,[253,254] fluorescent sensors,[4,14,255] and organic light-emitting diodes (OLEDs).[256–258] Recent experimental works have discovered a variety of novel solid-state PL properties in many crystalline systems, including polymorph-dependency,[259–261] coformer-dependency,[19,262] PL response to applied pressure (piezochromism),[28–30] and PL response to temperature (thermochromism).[261,263] Since polymorphism and cocrystal formation are two intensively investigated aspects of crystal engineering, which are critically relevant to the discovery and manufacture of pharmaceuticals, molecular crystals displaying polymorph- or coformer-dependent PL are particularly intriguing. Consistent with many other novel solid-state PL phenomena, intermolecular interactions within the crystal lattice are thought to play a subtle, yet potentially critical, role in polymorph- and coformer-dependent PL.

Computationally modeling polymorph- and coformer-dependent PL is of high theoretical interest, as periodic-boundary calculations can potentially unveil their mechanistic origin, and may also serve as a screening tool to optimize properties of candidate photoluminescent materials. Yet, such an endeavor also presents a great theoretical challenge, as the cost of wavefunction-based, correlated excited-state methods would be prohibitive in the molecular crystal context. Meanwhile, until very recently, successes in developing efficient time-dependent density-functional theory (TD-DFT) algorithms for periodic-boundary calculations[83,91,93] have been scarce. Another potential alternative is the quantum-mechanics/molecular-mechanics (QM/MM) embedding scheme,[37,244] where a MM cluster mimicking the crystalline environment could be built around a QM core on which the excitation is localized. However, the QM/MM scheme is not without its own shortcomings

as it neglects Pauli repulsion between the QM and MM subsystems, leading to the unphysical penetration of the QM-electron density into the MM subsystem.[55] Artificial accumulation of QM-electronic charge is also found at the QM/MM boundary, in cases when there exists an extensive H-bond network.[56]

We recently developed a novel and cost-efficient computational scheme to predict first-singlet excitation energies for molecular solids.[264] Our methodology combines isolated-molecule and dispersion-corrected periodic-boundary DFT calculations, and incorporates Becke's virial exciton model[100] to entirely bypass conventional excited-state methods. The virial exciton model has the advantage of computational simplicity, while also eliminating errors seen with TD-DFT for charge-transfer excitations.[245] We previously applied this methodology to modeling the piezochromic behaviors of a selection of molecular crystals,[264] and achieved general success in both cost-efficiency and predictive capability. In this work, we employ the same methodology to model the polymorph- and coformer-dependent PL in selected molecular crystals.

The best-known example of polymorph-dependent PL is the plethora of polymorphic crystals of 5-Methyl-2-[(2-nitrophenyl)amino]-3-thiophenecarbonitrile (Figure 7.1). This compound is better known as ROY due to the various colors ranging from Red to Orange to Yellow displayed by its polymorphs.[260] Herein, we model the absorption of a series of 8 ROY polymorphs whose crystallographic structures have been hitherto archived.[24] The experimental absorbance data for the investigated ROY polymorphs are summarized in Table 7.1. For coformer-dependent PL, we select a group of 4 cocrystals formed between 9-acetylanthracene (9-ACA) and each of 4 coformers (Figure 7.2). These 9-ACA cocrystals were found to display coformer-dependency in their emission (fluorescence) wavelengths, with their emission colors ranging from blue to green under UV light.[19] Their experimental emission data are summarized in Table 7.2. As the results will indicate, our methodology once again achieves qualitative to semi-quantitative success in predicting the polymorph- and coformer-dependent PL, demonstrating excellent transferrability between a variety of solid-state PL problems.

Figure 7.1: Molecular structure of 5-Methyl-2-[(2-nitrophenyl)amino]-3-thiophenecarbonitrile, commonly known as ROY due to the colors of its various polymorphic molecular crystals. A correlation exists between the colors of the ROY polymorphs and the internal rotation angle θ_{thio}.

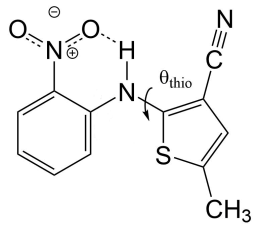

Figure 7.2: Molecular structures of 9-acetylanthracene (**A**) and its four coformers: 4-bromotetrafluorobenzenecarboxylic acid (**B**); 2,3,5,6-tetrafluorohydroquinone (**C**); octafluoro-naphthalene (**D**); and 1,2,4,5-tetracyanobenzene (**E**).

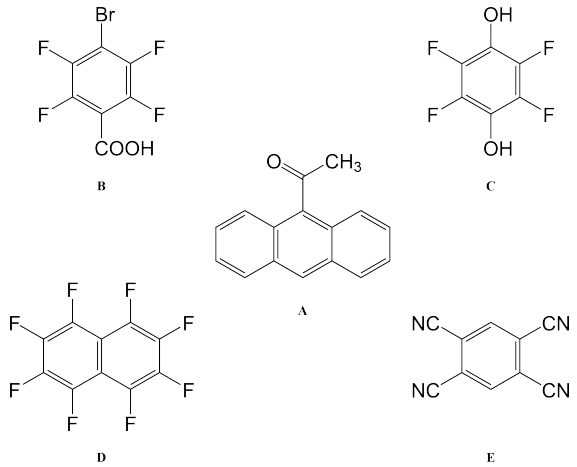

7.2 Computational Methods

Initial geometries of all molecular crystals were obtained from the Cambridge Crystallographic Data Centre (CCDC).[196] The atomic positions and cell parameters were fully relaxed using periodic-boundary DFT calculations. We employed the projector-augmented wave method[132] and the B86bPBE functional[88,107] paired with the exchange-hole dipole moment (XDM) dispersion correction,[102,103,154] using the Quantum ESPRESSO (QE) program.[101] The well-converged $2 \times 2 \times 2$ Monkhorst-Pack[127] k-point mesh and planewave cutoff values of 80 and 800 Ry for the kinetic energy and electron density, respectively, were used. All PAW datasets were generated via the "atomic" code by Dal Corso.[247]

Table 7.1: Eight investigated polymorphic crystals of ROY, with their conventional names and their corresponding Cambridge Structural Database (CSD) code names. Also given are magnitudes of the internal rotation angle, $|\theta_{\text{thio}}|$, from both experiment[265] and DFT relaxation, partially-available experimental absorption maximum wavelengths ($\lambda_{\text{max}}^{\text{abs}}$) and energies ($\Delta E^{\text{abs}}$). R: Red; R05: Red, 2005; ORP: Orange-Red Plate; OP: Orange Plate; ON: Orange Needle; YN: Yellow Needle; Y: Yellow; YT04: Yellow Transformed, 2004. The conventional names are color-coded according to the approximate colors of their corresponding polymorphs to render a more intuitive view

Polymorph	CSD code	$\lvert\theta_{\text{thio}}^{\text{expt}}\rvert$ (°)	$\lvert\theta_{\text{thio}}^{\text{calc}}\rvert$ (°)	$\lambda_{\text{max}}^{\text{abs}}$ (nm)	ΔE^{abs} (eV)
R	QAXMEH02	21.7	19.8	451	2.75
R05	QAXMEH33	34.0/44.9	23.3	-	-
ORP	QAXMEH05	39.4	29.0	-	-
OP	QAXHEM03	46.1	37.7	448	2.77
ON	QAXMEH	52.6	42.2	419	2.96
YN	QAXMEH04	104.1	113.0	415	2.99
Y	QAXMEH01	104.7	112.0	415	2.99
YT04	QAXMEH12	112.8	119.9	-	-

Table 7.2: The pristine 9-ACA crystal (**A**) and its four cocrystals (**A**·**B** to **A**·**E**), with their CSD code names, and their respective experimental emission (fluorescence) maximum wavelengths[19] ($\lambda_{\text{max}}^{\text{emi}}$) and energies ($\Delta E^{\text{emi}}$)

Species	CSD code	$\lambda_{\text{max}}^{\text{emi}}$ (nm)	ΔE^{emi} (eV)
A	DEZCAM	476	2.61
A·**B**	QAHNIZ	450	2.76
A·**C**	QAHNUL	466	2.66
A·**D**	QAHPAT	451	2.75
A·**E**	QAHNOF	600	2.07

Following geometry relaxation, absorption and emission energies were computed using the same multi-step approach used in our previous work modeling piezochromism,[264] which combines spin-polarized calculations on the target molecular crystals and on excised gas phase molecules. For absorption, a single-point energy calculation is performed on the crystal using constrained magnetization to model the first excited triplet state (T_1). The initial magnetic bias is applied to a single molecule to localize the excitation. For emission, the atomic positions of this T_1 state are relaxed, although the lattice constants are kept fixed at their ground-state values.

To obtain the absorption and emission energies for the first singlet excited state (S_1), a correction term obtained from Becke's virial exciton model[100] is applied to

the T_1 energy. This correction corresponds to the S_1-T_1 gap for a single molecule, excised from the relaxed crystal structure. The S_1-T_1 gap is given by the two-electron exchange integral, H_{12} (denoted as K_{if} in Ref. 100), computed from the two singly occupied HOMO and LUMO orbitals of the molecular T_1 state:

$$H_{12} = \left\langle \phi_a(1)\phi_b(2) \left| \frac{1}{r_{12}} \right| \phi_a(2)\phi_b(1) \right\rangle. \tag{7.1}$$

Thus, for a finite-molecule calculation, the S_1 excitation energy from the virial exciton model is

$$\Delta E_{0\mathrm{S}}^{\mathrm{mol}} = \Delta E_{0\mathrm{T}}^{\mathrm{mol}} + H_{12}^{\mathrm{mol}}. \tag{7.2}$$

Gas-phase calculations on the molecular moieties were performed with the Gaussian 09 (G09) program, using the B3LYP functional[90] and the cc-pVDZ basis set.[227] The BHandHLYP functional[248] was used in the θ_{thio}-scanning calculations on the ROY molecule, due to restricted open-shell convergence issues with the B3LYP functional. The molecular geometries were taken from the relaxed crystal structures for either the S_0 or T_1 states, for absorption or emission, respectively. In both cases, single-point restricted open-shell calculations were used to model the T_1 states and obtain the wavefunctions of the frontier orbitals. An in-house program, which employs the numerical integration method of Becke and Dickson,[218] was used to calculate the H_{12} integrals.

It is assumed that the total electron densities of the T_1 and S_1 states are very similarly affected by the surrounding crystalline environment, so that the single-molecule H_{12} value is a good approximation to the S_1-T_1 energy gap of the molecular crystal. Thus, the singlet excitation energy in the crystal can be written as

$$\Delta E_{0\mathrm{S}}^{\mathrm{cryst}} = \Delta E_{0\mathrm{T}}^{\mathrm{cryst}} + H_{12}^{\mathrm{mol}}. \tag{7.3}$$

Here $\Delta E_{0\mathrm{T}}^{\mathrm{cryst}}$ is the T_1 excitation energy, computed from periodic-boundary DFT, and H_{12}^{mol} is the S_1-T_1 gap from the finite-molecule calculation.

The assumption that the S_1-T_1 gap should be comparable for the molecule and crystal is based on the conjecture that the S_1 and T_1 states will have similar electron densities, differing only in the spin of one electron. This is also a fundamental assumption used in the virial exciton model itself and is supported by the excellent

performance of the model for gas-phase excitation benchmarks.[100,245] Additionally, we have found that the S_1 and T_1 states experience very similar dispersion interactions with the surrounding crystal lattice, as quantified by differences in the resulting lattice energies.[246,264]

In our previous study of piezochromism,[264] we found that the pressure-dependent shifts in absorption and emission energies were captured as well by changes in the molecular crystal's band gap. The valence-conduction band gap in a molecular crystal, analogous to the HOMO-LUMO (optical) gap in the context of an isolated molecule, is directly related to its S_0-S_1 excitation energy. As such, additional band-structure calculations were performed on the investigated molecular crystals and the valence-conduction band gap values (ΔE_{BG}) extracted. These calculations used the S_0 or T_1 geometries for comparison with experimental absorption or emission energies, respectively.

7.3 Results and Discussion

7.3.1 Polymorph-Dependent Absorption of ROY

We first apply our computational scheme to predict the polymorph-dependent PL of the 8 polymorphic crystals of ROY. The absorption energies are computed under the assumption of vertical excitation from S_0 to S_1. The results are compared to available experimental absorption data in Table 7.3. The virial exciton computations systematically underestimate the experimental absorption energies by $0.11-0.60$ eV. However, this quantitative comparison is complicated by the broad-band nature of the absorption spectral peaks,[265] which diminishes the precision of the experimental absorption-energy values. Impressively, upon ranking the 8 polymorphs' computed and experimental absorption energies in ascending order, the virial exciton model almost perfectly reproduces the experimentally observed R-O-Y "color-zoning", grouping each polymorph into the correct Red-Orange-Yellow tricolor regime.

The R-O-Y color zoning can be correlated with the intramolecular rotation angle, θ_{thio}, shown in Figure 7.1. The red and orange forms have small intramolecular angles, ranging from ca. $20-50°$, while the yellow forms have larger angles near $110°$. Smaller angles increase the extent of conjugation between the phenyl and thiophene rings, resulting in lower excitation energies, while larger angles break

Table 7.3: Calculated (ΔE_{0S}^{cryst}) vs. experimental[265] (ΔE_{abs}^{exp}) absorption energies for the 8 ROY polymorphs under investigation. ΔE_{0S}^{mol} are the molecular singlet-excitation energies, which are obtained by summing the H_{12} integral and the first-triplet excitation energies computed for the excised molecules. Also shown are the band gaps (ΔE_{BG}) for each polymorph. Each column is sorted in ascending order. All values are in eV.

Polymorph	ΔE_{abs}^{exp}	Polymorph	ΔE_{0S}^{cryst}	Polymorph	ΔE_{0S}^{mol}	Polymorph	ΔE_{BG}
R	2.75	R05	2.17	ON	3.30	R	1.12
R05	-	ORP	2.20	R05	3.38	R05	1.25
ORP	-	R	2.25	ORP	3.38	ON	1.30
OP	2.77	ON	2.28	R	3.40	ORP	1.37
ON	2.96	OP	2.36	OP	3.57	OP	1.38
YN	2.99	YT04	2.80	YT04	3.89	YN	1.62
Y	2.99	Y	2.88	YN	3.89	YT04	1.67
YT04	-	YN	2.92	Y	3.93	Y	1.84

conjugation and give rise to higher excitation energies. To verify the correlation between the excitation energies and θ_{thio}, gas-phase BHandHLYP[114,248]/cc-pVDZ calculations were conducted on the isolated ROY molecule using Gaussian 09.[175] The molecular geometry was relaxed with θ_{thio} constrained to values from 0° to 180°, in steps of 10°, and the S_1 excitation energy computed for each. As shown in Figure 7.3, our gas-phase results agree with the trends seen both in experiment and our crystalline calculations: the molecular excitation energy increases as the level of conjugation decreases, and peaks when θ_{thio} is exactly 90°, where the conjugation is completely broken. Thus, when the ROY molecule becomes more planar, the polymorph's color tends to red; when the ROY molecule becomes more twisted, the polymorph's color tends to yellow.

Our results in Table 7.3 show a pronounced separation in absorption energies between the yellow- and red/orange-colored polymorphs. Meanwhile, the red-orange separation is predicted to be much narrower, indicating an orange-colored transition zone that bears more structural resemblance to the red-colored regime. It is possible that our calculations are underestimating the spread in excitation energies for the red/orange polymorphs due to delocalization error,[187,188,266,267] which affects all generalized gradient approximations (GGAs), including the B86bPBE functional used in this work. One manifestation of delocalization error is that GGA functionals artificially stabilize systems with extended conjugation,[268–271] and this can affect molecular crystal structure prediction.[272–274] From Table 7.1, geometry

Figure 7.3: Correlation between θ_{thio} and the gas-phase singlet-excitation (absorption) energy ($\Delta E_{0S}^{\text{mol}}$) of the isolated ROY molecule.

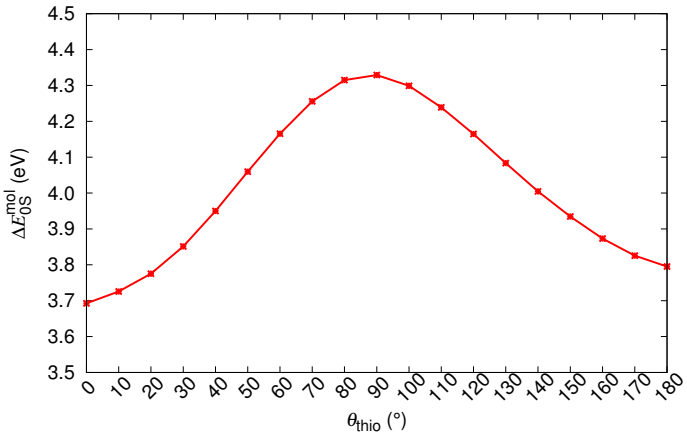

optimizations of the R05, ORP, OP, and ON polymorphs provide intramolecular angles that are ca. 10° smaller than in the experimental crystal structures, favouring increased planarity and conjugation. Underestimation of this dihedral could lead to underestimation of the T_1, and consequently the S_1, excitation energies for these four polymorphs.

Another possible cause for the observed discrepancies between our calculated internal dihedral angle and the experimental crystal structures is the omission of thermal expansion (or contraction) of the cell volume within the present computational scheme. Thermal effects may be particularly significant for ROY, as the PL of the Y polymorph has been demonstrated to be quite sensitive to the cell volume.[241] In agreement with previous work,[273,274] we found that fixed-lattice optimizations of the S_0 geometries significantly reduced the deviations in θ_{thio} for the 8 ROY polymorphs, from 15.8 to 3.8% mean absolute error, relative to experiment. We therefore conclude that the geometric discrepancies are mostly driven by the lack of thermal effects, which eventually leads to the aforementioned underestimation of the red-orange separation.

To further demonstrate the intramolecular nature of ROY's polymorph-dependent PL, the singlet excitation energies of the excised molecular moieties ($\Delta E_{0S}^{\text{mol}}$) are also shown in Table 7.3. While the molecular excitation energies yield large quantitative errors when compared to the experimental absorption energies for the crystal polymorphs, this is expected due to complete neglect of the surrounding

crystalline environment in computation of ΔE_{0S}^{mol}. However, the single-molecule results are able to replicate the experimental absorption-energy ranking and color zoning quite well, with the only one notable exception of polymorph ON. Thus, the polymorphism-dependent PL of ROY is predominantly due to the differences in the intramolecular geometry, in particular the internal rotation angle θ_{thio} of the ROY molecule in its various polymorphic crystals. Intermolecular interactions within the crystal only affect the color zoning of the ON polymorph. Since the ON crystal involves close π-stacking of ROY molecules, it is reasonable that the effects of intermolecular interactions are more pronounced for this form relative to the other polymorphs.

The final column in Table 7.3 shows the valence-conduction band gap (ΔE_{BG}) values. Unsurprisingly, the computed band gaps massively underestimate the experimental absorption energies, with errors of 1.3-1.6 eV for all 8 polymorphs. This underestimation is, in part, a manifestation of the well-known band gap problem seen with GGA density functionals.[250,275–277] Additionally, the valence-conduction band gap cannot be fully equated to the optical gap of a periodic solid.[278] However, ΔE_{BG} mostly reproduces the R-O-Y color-zoning, except for a minor crossover of the orange-colored ON polymorph into the red-colored regime, which was also seen in the molecular results. Furthermore, the clear separation between the red/orange-colored polymorphs and the yellow-colored polymorphs observed in the virial exciton calculations, using both the single molecules and molecular crystals, is retained.

7.3.2 Coformer-Dependent Emission of 9-ACA Cocrystals

Next, we turn our focus onto modeling the emission/fluorescence of the 9-acetylanthracene (9-ACA) cocrystals, which exhibit coformer-dependent PL. Applying our computational scheme specifically to emission, the results are tabulated in Table 7.4, together with the experimental emission data from the work of Li *et al.*[19] Unlike the ROY polymorphs, the 9-ACA cocrystals offer a good case for quantitative comparison between our calculations and experimental measurements. This is due to both the completeness of the experimental emission data and the sharp-peak nature of the emission/fluorescence spectrum, which allows for precise peak identification. Overall, our computed emission energies achieved a mean absolute error (MAE) of

0.31 eV compared to experiment. This MAE is on-par with the accuracy previously attained by the virial exciton model[100] on the Thiel small-molecule benchmark set,[124] as well as for a set of charge-transfer excitations.[245]

Our solid-state virial-exciton calculations are able to reproduce the experimental trend in emission energies among the four cocrystals: $\mathbf{A}\cdot\mathbf{E} \ll \mathbf{A}\cdot\mathbf{C} < \mathbf{A}\cdot\mathbf{B} \approx \mathbf{A}\cdot\mathbf{D}$. However, the experimental relations between the emission energies of the pristine crystal and the cocrystals are not fully reproduced by our calculations. Specifically, the experimental blue-shift of $\mathbf{A}\cdot\mathbf{B}$ and $\mathbf{A}\cdot\mathbf{D}$ from $\mathbf{A}$ is not predicted; rather, all three crystals are predicted to have similar emission energies. We also note that the largest quantitative error from experiment (0.45 eV) is seen for the single-component crystal $\mathbf{A}$, making it an outlier relative to the set of cocrystals.

Table 7.4: Calculated (ΔE_{0S}^{cryst}) vs experimental (ΔE_{0S}^{cryst}) emission energies for the four cocrystals ($\mathbf{A}\cdot\mathbf{B}$ to $\mathbf{A}\cdot\mathbf{E}$) and the pristine crystal ($\mathbf{A}$) of 9-ACA. ΔE_{0S}^{mol} are the molecular singlet-excitation energies and ΔE_{BG} are the computed band gaps. All values are in eV.

Species	ΔE_{emi}^{exp}	ΔE_{0S}^{cryst}	ΔE_{0S}^{mol}	ΔE_{BG}
$\mathbf{A}$	2.61	3.06	3.21	1.74
$\mathbf{A}\cdot\mathbf{B}$	2.76	2.96	3.15	1.65
$\mathbf{A}\cdot\mathbf{C}$	2.66	2.82	3.50	1.58
$\mathbf{A}\cdot\mathbf{D}$	2.75	3.08	3.19	1.81
$\mathbf{A}\cdot\mathbf{E}$	2.07	2.45	3.51	0.80
MAE	–	0.31	0.74	1.05

The computed band gaps, ΔE_{BG} shown in Table 7.4, also replicate the trends in experimental emission energies of the 9-ACA cocrystals to an impressive degree, despite large quantitative deviations. However, the difference between $\mathbf{A}\cdot\mathbf{C}$ and $\mathbf{A}\cdot\mathbf{B}$ is now considerably smaller than seen from the ΔE_{0S}^{cryst} results, while the difference between $\mathbf{A}\cdot\mathbf{B}$ and $\mathbf{A}\cdot\mathbf{D}$ is widened slightly. The experimental blue-shift of $\mathbf{A}\cdot\mathbf{B}$ and $\mathbf{A}\cdot\mathbf{D}$ from $\mathbf{A}$ is again not captured by ΔE_{BG}, further solidifying the status of the pristine 9-ACA crystal as an outlier, compared to its cocrystals. The large quantitative underestimation of $\Delta E_{abs/emi}^{exp}$ by ΔE_{BG} reflects the value of including the localized virial exciton model in our methodology, which can correct for the band-gap problem and hone in on the actual excitation energies.

Similar to the previous case of the ROY polymorphs, we also computed the gas-phase emission energies for the 9-ACA molecules (ΔE_{0S}^{mol}) excised from each

Figure 7.4: Degrees of intermolecular CT within the cocrystals and the pristine crystal of 9-ACA, as indicated by the absolute charge per molecule.

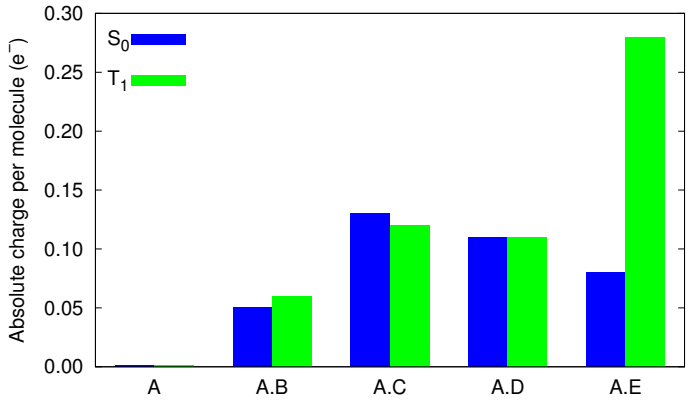

relaxed crystal structure. The large quantitative deviation from the experimental values is again to be expected due to neglect of the surrounding intermolecular interactions. However, in the case of the 9-ACA cocrystals, the single-molecule emission energies are entirely unable to capture any experimental trends. ΔE_{0S}^{mol} even fails to predict the largest red shift in emission energy, seen for **A**·**E**, and instead predicts a substantial blue shift for this cocrystal. This indicates that the coformer-dependent emission of the 9-ACA cocrystals is controlled by *inter*molecular interactions, necessitating the inclusion of the crystalline surroundings to distinguish between red and blue shifts in emission wavelengths. This stands in stark contrast to the *intra*molecular nature of the polymorph-dependent absorption of ROY, where a fairly decent prediction of the polymorphs' color zoning could be still obtained by merely modeling the molecular moiety excised from the crystal lattice. Indeed, the importance of intermolecular factors for the 9-ACA cocrystals can be inferred from the strategy used by Li *et al.*[19] in their design, which aimed to exploit different degrees of intermolecular charge transfer (CT) between the 9-ACA molecule and the various coformers.

To verify the role played by intermolecular CT in shifting the emission energies, Bader charge analysis,[279] using the critic2 program,[197] was performed on the molecular moieties within the cocrystals **A**·**B** to **A**·**E**, and the pristine crystal **A**, in both the S_0 and T_1 states. Figure 7.4 shows the results of this analysis, in the form of the absolute charge per molecular moiety within each (co)crystal. While no intermolecular CT is predicted between the 9-ACA molecules within the pristine

crystal, intermolecular CT from 9-ACA to the coformer is consistently predicted for all 4 cocrystals. Moderate amounts of CT ($\sim 0.05 - 0.13$ e^-) are seen for both S_0 and T_1 states of each cocrystal, with the exception of **A**·**E** in the T_1 state, where the intermolecular CT increases drastically to 0.28 e^-. This increased charge transfer should preferentially stabilize the T_1 state of **A**·**E**, relative to S_0, and lead to a red shift in the emission energy. This charge analysis affirms the validity of the experimental designing strategy for **A**·**E**.[19] The tetracyano-substituted coformer **E** has by far the strongest electron-withdrawing effect, and therefore induces a larger amount of CT from the 9-ACA molecule, especially in the excited state, leading to its large emission red-shift.

The lack of intermolecular CT in the pristine crystal likely contributes to the apparent irregularity in its computed emission energy compared to the set of cocrystals. As noted above, the B86bPBE functional (like all GGA functionals) exhibits delocalization error, which causes preferential stabilization of systems with more CT.[183,185,229,230] Thus, there is likely a systematic error cancellation in the computed properties of the cocrystals and the comparability between results for the pristine crystal and the cocrystals is significantly diminished. This explains the inability of our calculations to fully replicate the experimental relations between the emission energies of **A** and **A**·**B** to **A**·**E**.

7.4 Conclusions

In this work, we applied our novel computational methodology, which combines plane-wave periodic-boundary DFT calculations for solids and isolated-molecule DFT calculations using the virial exciton model, to the modeling of polymorph- and coformer-dependent PL in the polymorphs of ROY and the cocrystals of 9-ACA, respectively. For the 8 ROY polymorphs, our results were able to replicate the experimentally-observed R-O-Y color zoning. For this compound, the polymorph-dependent PL was shown to be driven by the intramolecular geometry, and the key role of the internal rotation angle θ_{thio} in determining the coloration of these ROY polymorphs was confirmed.

For 9-ACA, our results were able to replicate the experimental ordering of the emission energies among the cocrystals and, quantitatively, an overall MAE of 0.31

eV was achieved by our calculations. However, trends regarding blue-shifting with respect to the pristine 9-ACA crystal were not captured. This can be attributed to delocalization error, which likely causes overstabilization of the cocrystals, all of which exhibit significant CT, relative to the pure 9-ACA crystal. Inclusion of the crystalline environment is necessary to model the coformer-dependent PL of 9-ACA, as it is predominantly driven by CT and other intermolecular interactions. This stands in contrast to the previous case of polymorph-dependent PL of ROY. The significant red-shift in the emission energy of the cocrystal **A**·**E** was rationalized through the increase in intermolecular CT from the ground to the excited state.

Although not as accurate as the combined solid-state and isolated molecule scheme, computed valence-conduction band gap values also offered fair qualitative replications of the experimental trends for both the ROY polymorphs and 9-ACA cocrystals. Due to their computational simplicity, use of band-structure calculations for qualitative prediction of solid-state PL warrants further exploration in future modeling studies.

Within the confines of our current computational methodology, we are not yet able to reproduce full absorption/emission spectra for our modeled systems. While the first singlet transition energy is of primary spectroscopic importance for most luminescent molecular crystals, knowledge of the full spectral line shape may be required to fully determine crystal colour, particularly for cases with broad adsorption/emission bands. Theoretically, it is possible to approximate the full spectrum by incorporating vibrational levels via the Franck-Condon principle.[280] However, the computational cost of the requisite phonon calculations borders on prohibitive, even with sampling of only the Γ point, considering that our systems of interest frequently contain 150 to 200 atoms (or more) in their unit cells.

In closing, our employed methodology was successful in capturing the experimentally observed polymorph- and conformer-dependent PL behaviors of the investigated sets of molecular crystals. Along with its previous success in modeling piezochromism,[264] the current methodology displays excellent transferrability among a diversity of solid-state PL properties in molecular crystals. This work opens the door for theory-driven crystal engineering to optimize PL properties of molecular materials for targeted device applications.

Supplementary Material

The reader may consult Appendix B for supplementary material to this work, which includes: calculated crystalline and molecular triplet excitation energies for all investigated species; calculated valence and conduction band edges for all investigated molecular crystals; the internal rotation angle (θ_{thio}) values for the ROY polymorphs using fixed-cell and variable-cell optimizations; data for the amounts of absolute charge per 9-ACA molecule in 9-ACA and its cocrystals; and an expanded version of Figure 7.3.

Chapter 8

Conclusions and Future Work

The central objective of this thesis is the design, validation, and application of a novel theoretical methodology for the accurate and cost-efficient calculation of the first singlet (i.e. S_0 to S_1) excitation energy in molecular crystals. A systematic endeavor in this direction is highly valuable, as a theoretical methodology combining both prediction accuracy and cost-efficiency might enable the fast pre-laboratory screening of candidate molecular crystals potentially displaying industrially-applicable solid-state PL properties. Successful theoretical modeling could also aid our understanding of the underlying physical mechanism that gives rise to the diverse solid-state PL properties seen experimentally.

To achieve our goal, we proposed a highly innovative computational scheme. Most significantly, our methodology completely circumvents all conventional time-dependent excited-state methods, such as time-dependent correlated wavefunction theories and the very popular TDDFT, both of which are currently too costly to fully implement in the context of periodic solids. Our methodology features a combination of first-principles ground-state DFT calculations for both isolated molecules and solids under periodic-boundary conditions, and the use of the virial exciton model for direct prediction of the S_1-T_1 energy splitting. In order to properly model the intermolecular interactions within the crystal lattice, which are potentially crucial in rendering the modeled solid-state PL properties, our periodic-boundary solid-state calculations are combined with the XDM dispersion correction, which has previously seen much success when applied to the solid state.

Our initial studies served as theoretical preparations and validations for our

proposed methodology. In a first-of-its-kind investigation, we probed the effect of electronic excitations on London dispersion, which is a key source of intermolecular interactions in both molecular and solid-state systems. Our results demonstrated that, despite potentially large changes in the molecular dispersion coefficients upon intermolecular charge-transfer excitations, the effect of such an excitation on the overall dispersion energy of the whole crystal lattice remains minimal. This finding helps justify a key assumption in our computational approach, which is that the intermolecular interactions will be effectively equivalent for the S_1 and T_1 excited states within the crystal.

In the next study, we addressed concerns with the capability of our proposed methodology to accurately model excitations of significant CT nature, which are highly problematic for conventional TDDFT methods. The virial exciton model, which is directly responsible for the calculation of the first singlet excitation energy in our methodology, was tested for a set of molecular systems featuring CT excitations. The results showed that the virial exciton model is equally reliable when applied to CT excitations, achieving a very similar accuracy to that for the non-CT cases, when compared to high-level theoretical benchmark data. Therefore, the virial exciton model proved to be free from the well-known CT errors suffered by conventional TDDFT methods, giving our methodology a significant edge over TDDFT when modeling similar excitations in the solid state.

After building a solid theoretical foundation via the aforementioned preparatory studies, we moved on to the full application of our methodology to model a range of experimentally-observed solid-state PL properties in a variety of luminescent molecular crystals. Overall, our methodology achieved satisfactory performance in replicating the experimental trends with respect to the first singlet excitation energies of the investigated molecular crystals. Valuable theoretical insights into the mechanisms of these solid-state PL properties were also obtained from the analysis of our results. Quantitative success was achieved for replication of the pressure dependency (i.e. piezochromism) of the emission energies of the tetrathiazolylthiophene, boron diketonate and 2,7-diaryl-TAP molecular crystals. In particular, both the magnitudes of the overall piezochromic red shifts and the corresponding rates of change in the emission energies with applied pressure were

predicted with impressive quantitative accuracy, for all three investigated molecular crystals. Significantly, our results found that piezochromism is predominantly driven by the subtle pressure modulation of the intermolecular interactions within the crystal lattice. Additionally, our results were also able to elucidate the origin of the universally-observed piezochromic red shifts from two perspectives: molecular and solid-state. From the molecular perspective, it was found that the polarizability of the embedded molecular moiety is consistently higher in the excited state than in the ground state. This leads to the preferential stabilization of the excited state under increasing constriction of the surrounding lattice, resulting in a piezochromic red shift. From the solid-state perspective, band-structure calculations revealed that increasing pressure has the effect of steadily narrowing the valence-conduction band gap of the molecular crystal, which also results in a piezochromic red shift.

Following the study on piezochromism, we then applied our methodology to model the polymorphism-dependent PL of the well-known ROY polymorphs and the coformer-dependent PL of the cocrystals of 9-acetylanthracene (9-ACA). Our methodology was able to qualitatively replicate the Red-Orange-Yellow "color-zoning" among the 8 investigated polymorphs of ROY, correctly matching each polymorph with its experimentally observed color regime. Our results confirmed the intramolecular nature of ROY's polymorphism-dependent PL, highlighting the pivoting role of the θ_{thio} intramolecular dihedral angle in determining the colors of the investigated ROY polymorphs. For 9-ACA and its cocrystals, our results successfully replicated the emission-energy ranking among the 4 cocrystals. Good quantitative accuracy of the predicted emission energies was obtained by our calculations, achieving a MAE of 0.31 eV compared to the experimental emission values. Further, the coformer-dependent PL of 9-ACA was found to be predominantly driven by the intermolecular interactions within the crystal lattice, and consideration of the crystalline surroundings of the excited molecular moiety is necessary to recover the experimentally observed trends in the emission energies. This is in clear contrast to the case of ROY polymorph coloration, illustrating the diverse physical origins of different solid-state PL properties. Moreover, analysis of our results confirmed the role of intermolecular CT in determining the coformer-dependent emission of the investigated cocrystals, offering theoretical validation of the experimental design

strategy of exploiting intermolecular CT via cocrystalization.

Through the works hitherto presented, we believe that the thesis goal of establishing of a novel, elegant, and cost-efficient theoretical methodology for calculation of the first singlet excitation energies in molecular crystals has been achieved. The devised methodology proved robust and reliable in its applications. It has also demonstrated excellent transferability, successfully modeling a range of solid-state PL properties, including piezochromism, polymorphism-dependent PL, and coformer-dependent PL, in a diversity of molecular crystal systems. Our methodology strikes a good balance between computational cost and prediction accuracy, allowing for decent semi-quantitative prediction of absorption/emission energies of luminescent molecular crystals. Even more importantly, our methodology achieved excellent prediction of the qualitative energetic trends that give rise to the aforementioned solid-state PL properties. Our results were able to elucidate the underlying mechanisms that drive these diverse solid-state PL properties, thereby contributing to the general theoretical understanding of electronic excitations in molecular crystals.

Potentially, our methodology could be combined with rapidly-developing crystal structure prediction (CSP)[281,282] techniques to achieve fast *in silico* pre-screening of candidate molecular crystals for various industrially desired PL properties. Via successful CSP, a small number of the minimum-energy (co)crystal structures of an organic chromophore can be efficiently generated; our methodology can then be applied to these generated structures to probe if they display any solid-state PL property of interest. Such a combined scheme could lead to dramatic increases in throughput for the discovery, design, and synthesis of novel solid-state luminescent materials. Meanwhile, the incorporation of thermal effects into our crystal geometry optimizations may enable the modeling of thermally activated solid-state PL properties, notably thermochromism,[22,25] where the PL wavelengths of a molecular crystal experience shifts with respect to changing temperature. In such an investigation, thermal-energy correction methods, such as density-functional perturbation theory (DFPT),[283,284] will be employed to obtain accurate crystal structures at varying temperatures. Our methodology can then be applied to obtain the absorption/emission energies of the molecular crystal over a range of

temperatures. The inclusion of thermal-energy corrections could also enhance our methodology's predictive accuracy in potential cases where the crystal-structure changes induced by thermal expansion have a non-negligible impact on the crystal's electronic excitation energies.

Appendix A

Supplementary Material for Computational Modeling of Piezochromism in Molecular Crystals

Figure A.1: Calculated absorption energies (ΔE_{0S}^{abs}) versus applied pressure, decomposed into the triplet-excitation (ΔE_{0T}^{abs}) and the H_{12}^{mol} integral contributions. The triplet excitation energies for the excised molecules (ΔE_{0T}^{mol}) are also shown.

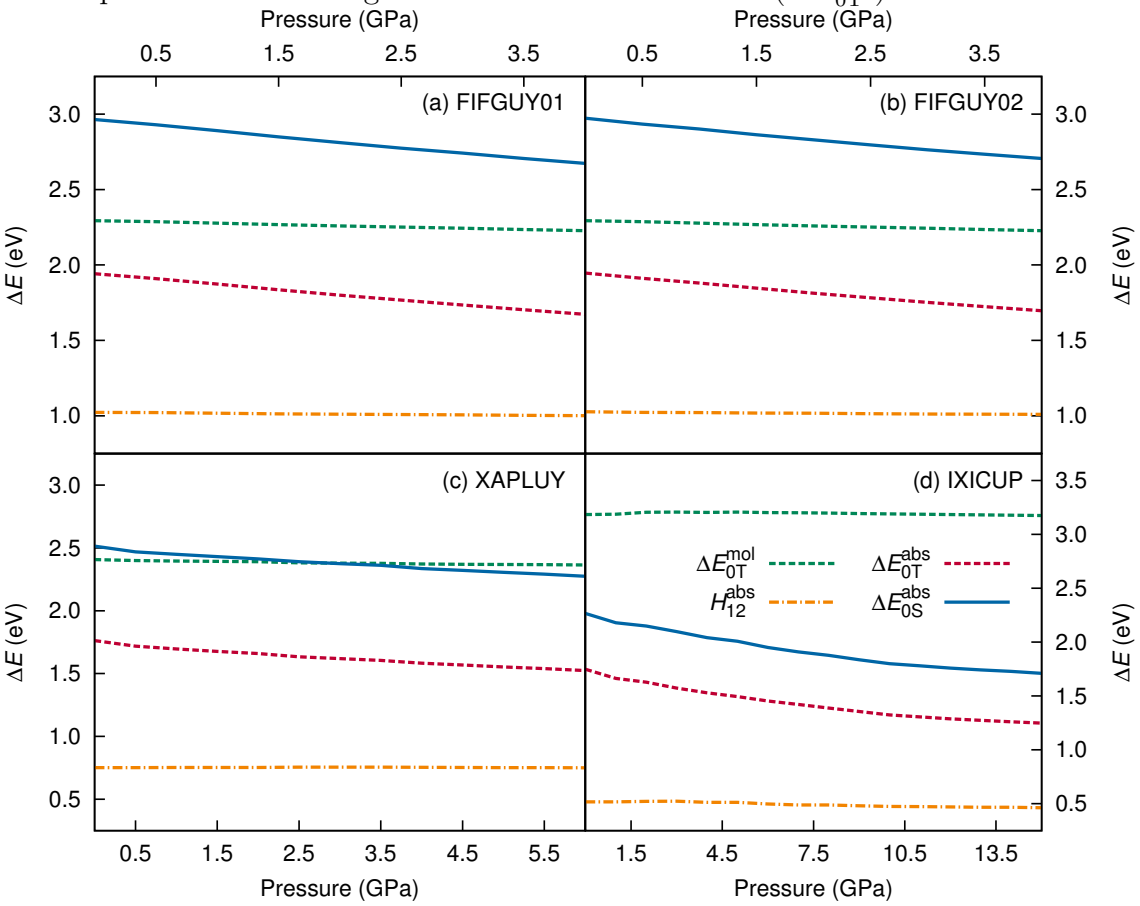

Figure A.2: Calculated polarizabilities of the excised molecules as a function of pressure for the singlet (S_0) and unrestricted triplet (T_1) states, using the solid-state absorption or emission geometries.

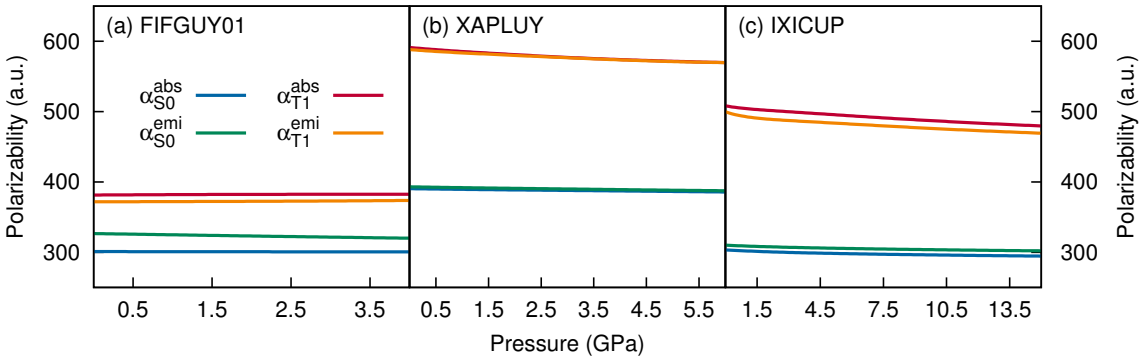

Figure A.3: Valence and conduction band edges, and band gaps, of the molecular crystals as functions of applied pressure using the absorption (S_0) geometries.

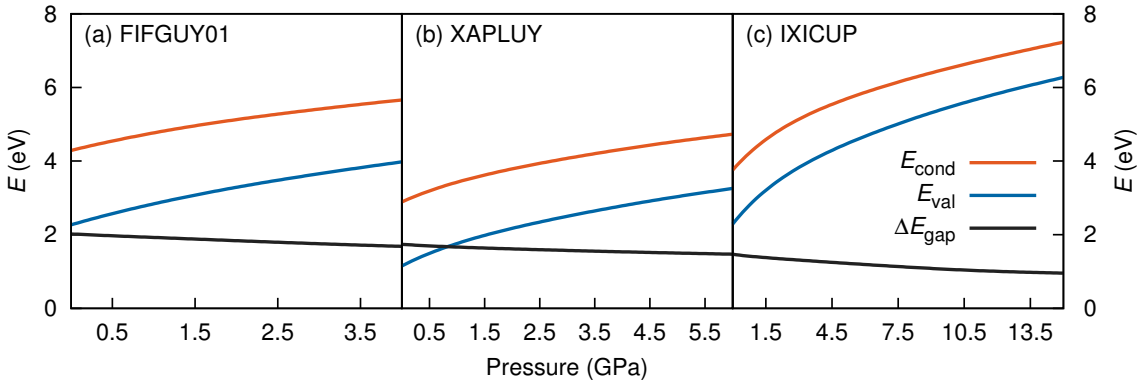

Figure A.4: Representative band structures near the valence-conduction band gap, obtained for the S_0 geometries at zero pressure. Energies are expressed relative to the valence band edge. Top: FIFGUY01; middle: XAPLUY; bottom: IXICUP.

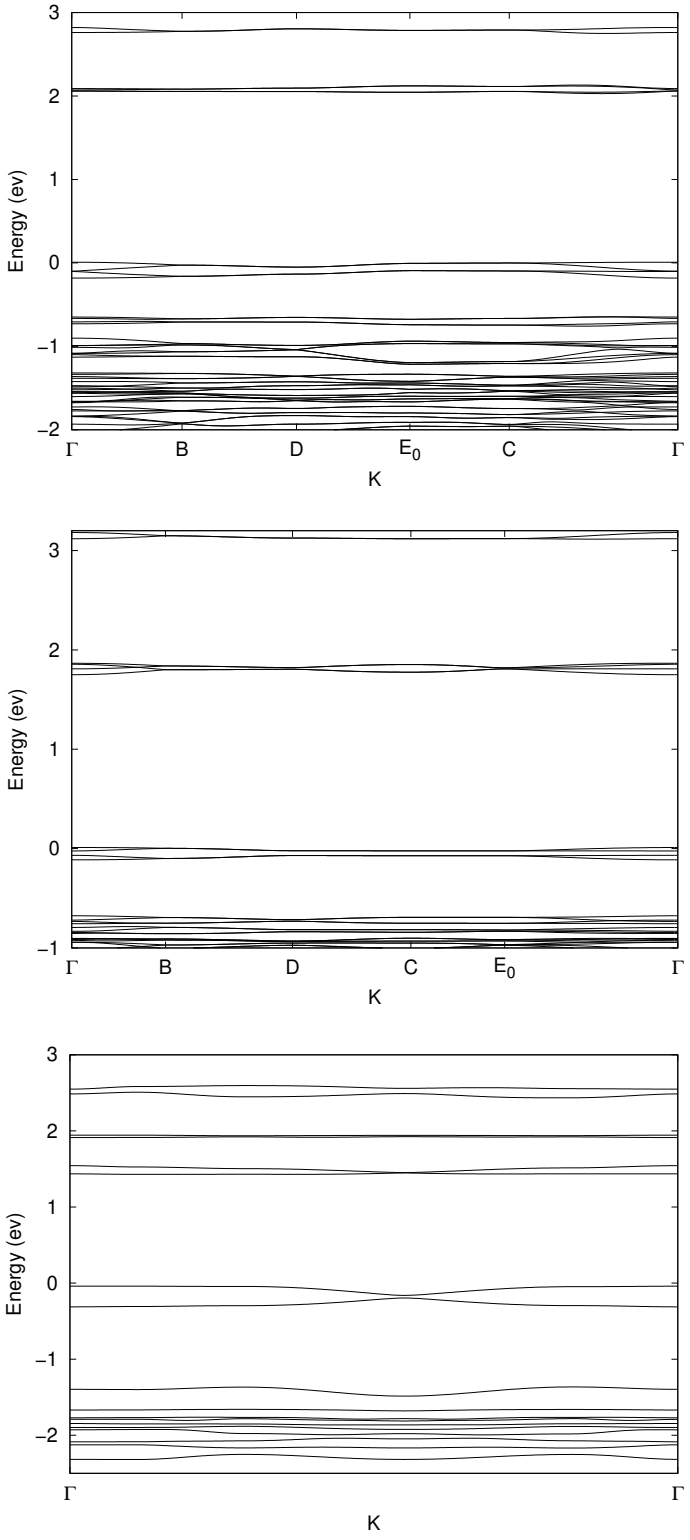

Appendix B

Supplementary Material for Polymorph- and Coformer-Dependent Electronic Excitations in the Solid State: A Theoretical Perspective

Table B.1: Absorption of the 8 ROY polymorphs: calculated triplet-excitation energies for the crystal ($\Delta E_{0\mathrm{T}}^{\mathrm{cryst}}$) and the excised 9-ACA molecule ($\Delta E_{0\mathrm{T}}^{\mathrm{mol}}$), along with the molecular singlet-triplet splittings ($\Delta E_{\mathrm{ST}}^{\mathrm{mol}}$). All values are in eV.

Species	$\Delta E_{0\mathrm{T}}^{\mathrm{cryst}}$	$\Delta E_{0\mathrm{T}}^{\mathrm{mol}}$	$\Delta E_{\mathrm{ST}}^{\mathrm{mol}}$
R	1.52	2.66	0.74
R05	1.40	2.61	0.77
ORP	1.44	2.62	0.76
OP	1.55	2.76	0.81
ON	1.50	2.52	0.78
YN	1.92	2.90	0.99
Y	1.92	2.97	0.96
YT04	1.84	2.93	0.96

Table B.2: Emission of 9-ACA (**A**) and its cocrystals (**A**·**B**–**A**·**E**): calculated triplet-excitation energies for the crystal ($\Delta E_{0\mathrm{T}}^{\mathrm{cryst}}$) and the excised 9-ACA molecule ($\Delta E_{0\mathrm{T}}^{\mathrm{mol}}$), along with the molecular singlet-triplet splittings ($\Delta E_{\mathrm{ST}}^{\mathrm{mol}}$). All values are in eV.

Species	$\Delta E_{0\mathrm{T}}^{\mathrm{cryst}}$	$\Delta E_{0\mathrm{T}}^{\mathrm{mol}}$	$\Delta E_{\mathrm{ST}}^{\mathrm{mol}}$
A	1.47	1.62	1.59
A·**B**	1.38	1.57	1.58
A·**C**	1.39	2.07	1.43
A·**D**	1.48	1.59	1.60
A·**E**	1.01	2.07	1.44

Table B.3: Band structures of the 8 ROY polymorphs: calculated valence band edges (maximum, $E_{\mathrm{val}}^{\mathrm{max}}$) and conduction band edges (minimum, $E_{\mathrm{cond}}^{\mathrm{min}}$), along with the corresponding valence-conduction band gaps (ΔE_{BG}). All values are in eV.

Species	$E_{\mathrm{val}}^{\mathrm{max}}$	$E_{\mathrm{cond}}^{\mathrm{min}}$	ΔE_{BG}
R	2.12	3.24	1.12
R05	0.95	2.21	1.25
ORP	1.92	3.28	1.37
OP	1.96	3.34	1.38
ON	2.02	3.32	1.30
YN	1.68	3.30	1.62
Y	1.73	3.57	1.84
YT04	1.86	3.53	1.67

Table B.4: Band structures of 9-ACA (**A**) and its cocrystals (**A**·**B**–**A**·**E**): calculated valence band edges (maximum, $E_{\mathrm{val}}^{\mathrm{max}}$) and conduction band edges (minimum, $E_{\mathrm{cond}}^{\mathrm{min}}$), along with the corresponding valence-conduction band gaps (ΔE_{BG}). All values are in eV.

Species	$E_{\mathrm{val}}^{\mathrm{max}}$	$E_{\mathrm{cond}}^{\mathrm{min}}$	ΔE_{BG}
A	1.78	3.52	1.74
A·**B**	2.03	3.68	1.65
A·**C**	1.83	3.41	1.58
A·**D**	1.98	3.79	1.81
A·**E**	1.62	2.42	0.80

Table B.5: The ROY molecule: calculated values of molecular triplet-excitation energies ($\Delta E_{0\mathrm{T}}^{\mathrm{mol}}$) and molecular S_1-T_1 splittings (H_{12}), across the 0-180° range of θ_{thio}.

θ_{thio} (°)	$\Delta E_{0\mathrm{T}}^{\mathrm{mol}}$ (eV)	H_{12} (eV)
0	3.69	0.68
10	3.73	0.65
20	3.78	0.68
30	3.85	0.73
40	3.95	0.79
50	4.06	0.85
60	4.17	0.92
70	4.26	0.98
80	4.31	1.01
90	4.33	1.02
100	4.30	1.01
110	4.24	0.97
120	4.16	0.93
130	4.08	0.89
140	4.00	0.84
150	3.93	0.79
160	3.87	0.73
170	3.83	0.68
180	3.80	0.62

Table B.6: ROY polymorphs: internal rotation angle values calculated using fixed-cell optimization ($\theta^{\mathrm{fc}}_{\mathrm{thio}}$) and variable-cell optimization ($\theta^{\mathrm{vc}}_{\mathrm{thio}}$) on ground-state crystal geometries, compared to experiment ($\theta^{\mathrm{exp}}_{\mathrm{thio}}$). The main absolute percentage errors (MAPE's) of $\theta^{\mathrm{fc}}_{\mathrm{thio}}$ and $\theta^{\mathrm{vc}}_{\mathrm{thio}}$ from $\theta^{\mathrm{exp}}_{\mathrm{thio}}$ are also given.

Species	$\theta^{\mathrm{exp}}_{\mathrm{thio}}$ (°)	$\theta^{\mathrm{fc}}_{\mathrm{thio}}$ (°)	$\theta^{\mathrm{vc}}_{\mathrm{thio}}$ (°)
R	21.7	22.1	19.8
R05	34.0/44.9	42.5	23.3
ORP	39.4	36.4	29.0
OP	46.1	43.1	37.7
ON	52.6	50.5	42.2
YN	104.1	106.2	113.0
Y	104.7	106.4	112.0
YT04	112.8	114.4	119.9
MAPE	-	3.8%	15.8%

Table B.7: 9-ACA (**A**) and its cocrystals (**A**·**B**–**A**·**E**): the amounts of absolute charge per 9-ACA molecule (e^-) in S_0 and T_1.

Species	S_0	T_1
A	0.001	0.001
A·**B**	0.05	0.06
A·**C**	0.13	0.12
A·**D**	0.11	0.11
A·**E**	0.08	0.28

Figure B.1: The ROY molecule: calculated molecular singlet-excitation energies ($\Delta E_{0S}^{\mathrm{mol,rel.}}$), molecular S_1-T_1 splitting ($H_{12}^{\mathrm{rel.}}$), and S_0 and T_1 energies ($E_{S_0/T_1}^{\mathrm{rel.}}$), across the 0-180° range of θ_{thio}, all relative to their respective values at $\theta_{\mathrm{thio}} = 0°$.

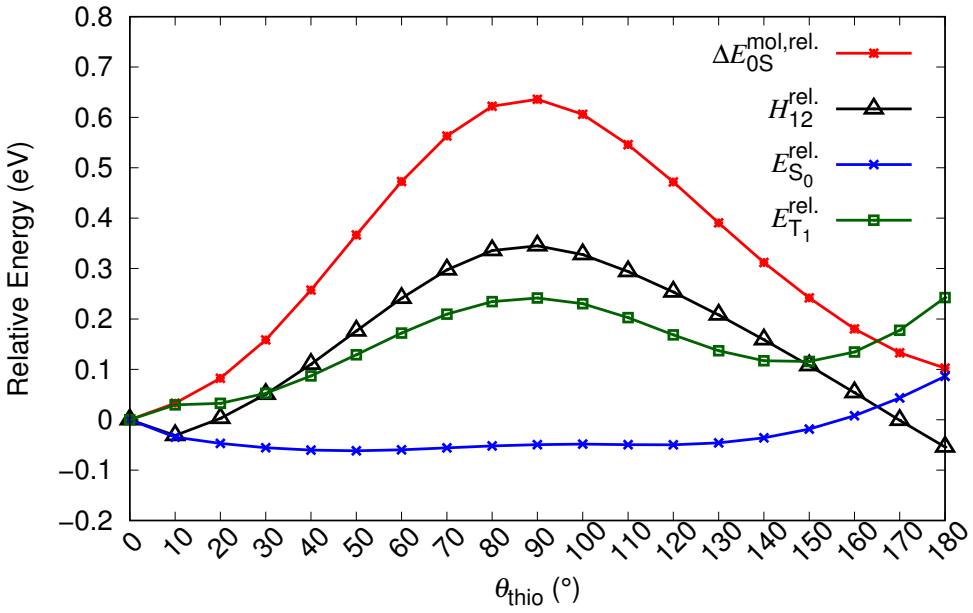

Appendix C

Miscellaneous Records

C.1 Conference Attendances and Presentations

- ACS 2021 Spring Meeting. April 2021, online. Oral presentation titled: "A Novel Approach for Modeling Solid-State Electronic Excitations".
- RSC Poster Twitter Conference 2021 March 2021, online. Poster titled: "Computational Modeling of Piezochromism in Molecular Crystals"
- The 6.5th Crystal Engineering and Emerging Materials Workshop of Ontario and Quebec (CEMWOQ-6.5). June 2020, online. Oral presentation titled: "Piezochromism in Molecular Crystals: A Computational Study".
- The 102nd Canadian Chemistry Conference and Exhibition (CCCE). June 2019, Québec, QC. Poster titled: "Application of Becke's Virial Exciton Model on Charge-Transfer Excitations".
- Photoinduced Processes in Embedded Systems (PPES) 2018. June 2018, Pisa, Italy. Poster titled: "Fully Ab-Initio Modeling of the First Singlet Excitation Energy in Molecular Crystals".
- The 16th International Congress of Quantum Chemistry (ICQC). June 2018, Menton, France. Poster titled: "Fully Ab-Initio Modeling of the First Singlet Excitation Energy in Molecular Crystals".
- Dalhousie Chemistry Research Symposium 2017. September 2017, Halifax, NS. Poster titled: "The Effect of Charge-Transfer Excitations on London

Dispersion: A TDDFT Study".

- Atlantic Theoretical Chemistry Symposium (ATCS) 2017. August 2017, Halifax, NS. Poster titled: "The Effect of Charge-Transfer Excitations on London Dispersion: A TDDFT Study".

- The 100th Canadian Chemistry Conference and Exhibition (CCCE). May 2017, Toronto, ON. Poster titled: "Modeling London Dispersion in Classical Lewis Adducts Using Density-Functional Theory".

C.2 Graduate Coursework

- PHYC 5151: Quantum Physics II
  (Full course by J. Maassen, fall 2016. Final grade: A-)

- CHEM 5301: Theory of Chemical Bonding
  (Full course by E. R. Johnson, winter 2017. Final grade: A)

- CHEM 6353: Density-Functional Theory
  (Graduate module by E. R. Johnson, winter 2018. Final grade: A+)

- CHEM 6363: Electronic Structure Theory of Solids
  (Graduate module by J. W. Zwanziger, winter 2018. Final grade: A-)

- PHYC 6201: Solid State Physics
  (Full course by J. Maassen, spring 2019. Final grade: A+)

C.3 Teaching Assistantship

- Total TA hours: 540 hours completed as of June, 2019. PhD program minimum: 360 hours.

C.4 Awards and Scholarships

- ATCS 2017 Student Poster Second Prize (August, 2017).
- Nova Scotia Graduate Scholarship (NSGS-D) (August, 2018 - August, 2020)
- Gerry Dauphinee Graduate Student Award (September, 2018).
- The 102th CCCE Best Student Poster Prize, Physical and Theoretical Chemistry Section (June, 2019).
- The 6.5th CEMWOQ Dectris Oral Presentation Prize (June, 2020).

C.5 Program Timeline

- September, 2016: Entry into the MSc program (Chemistry).
- September, 2017: Delivery of Graduate Seminar I. Seminar title: "Machine Learning in Chemistry: An Introduction".
- December, 2017: Completion of minimum TA hours at PhD level (360 hours).
- April, 2018: Completion of PhD program qualifying examination.
- September, 2018: Formal transfer into the PhD program.
- April, 2019: Completion of PhD-level coursework requirement.
- November, 2020: Delivery of Graduate Seminar II. Seminar title: "Solid-State Electronic Excitations: Theoretical Insights Through A Novel Approach".
- May, 2021: PhD thesis submission.
- July, 2021: PhD thesis defense.

Bibliography

[1] M. Pope and C. E. Swenberg, *Electronic Processes in Organic Crystals*, Oxford University Press, Oxford, UK, 1999.

[2] J. Mei, N. L. C. Leung, R. T. K. Kwok, J. W. Y. Lam, and B. Z. Tang, Aggregation-induced emission: Together we shine, united we soar!, Chem. Rev. **115**(21), 11718–11940 (2015).

[3] X. Zhao, P. Xue, K. Wang, P. Chen, P. Zhang, and R. Lu, Aggregation-induced emission of triphenylamine substituted cyanostyrene derivatives, NewJ. Chem. **38**, 1045–1051 (2014).

[4] X. Hou, C. Ke, C. J. Bruns, P. R. McGonigal, R. B. Pettman, and J. F. Stoddart, Tunable solid-state fluorescent materials for supramolecular encryption, Nat. Commun. **6**, 6884 (2015).

[5] Y. Che and L. Zang, Enhanced fluorescence sensing of amine vapor based on ultrathin nanofibers, Chem. Commun. **0**, 5106–5108 (2009).

[6] L.-L. Li, K. Li, Y.-H. Liu, H.-R. Xu, and X.-Q. Yu, Red emission fluorescent probes for visualization of monoamine oxidase in living cells, Sci. Rep. **6**, 31217 (2016).

[7] M. Furno, R. Meerheim, S. Hofmann, B. Lüssem, and K. Leo, Efficiency and rate of spontaneous emission in organic electroluminescent devices, Phys. Rev. B **85**, 115205 (2012).

[8] H. Sasabe and J. Kido, Recent progress in phosphorescent organic light-emitting devices, Eur. J. Org. Chem. **34**, 7653–7663 (2013).

[9] H. Kaji, H. Suzuki, T. Fukushima, K. Shizu, K. Suzuki, S. Kubo, T. Komino, H. Oiwa, F. Suzuki, A. Wakamiya, Y. Murate, and C. Adachi, Purely organic electroluminescent material realizing 100% conversion from electricity to light, Nat. Commun. **6**, 8476 (2015).

[10] S. Chénais and Forget, Recent advances in solid-state organic lasers, Polym. Int. **61**, 390–406 (2012).

[11] K. Kundu, S. Knight, N. Willett, S. Lee, W. Taylor, and N. Murthy, Hydrocyanines: a class of fluorescent sensors that can image reactive oxygen species in cell culture, tissue, and in vivo, Angew. Chem. Int. Ed. **48**, 299–303 (2009).

[12] G. R. Desiraju, Crystal engineering: a holistic view, Angew. Chem. Int. Ed. **46**, 8342–8356 (2007).

[13] P. Gao, H. N. Tsao, M. Grätzel, and M. K. Nazeeruddin, Fine-tuning the electronic structure of organic dyes for dye-sensitized solar cells, Org. Lett. **14**(17), 4330–4333 (2012).

[14] S. P. Anthony, Organic solid-state fluorescence: strategies for generating switchable and tunable fluorescent materials, ChemPlusChem **77**, 518–531 (2012).

[15] J. D. Wuest, Co-crystals give light a tune-up, Nat. Chem **4**, 74–75 (2012).

[16] D. Yan, A. Delori, G. O. Lloyd, T. Friščić, G. M. Day, W. Jones, J. Lu, M. Wei, D. G. Evans, and X. Duan, A cocrystal strategy to tune the luminescent properties of stilbene-type organic solid-state materials, Angew. Chem., Int. Ed. **50**, 12483–12486 (2011).

[17] D. Yan, M. Day, X. Duan, et al., Modification of luminescent properties of a coumarin derivative by formation of multi-component crystals, CrystEngComm **14**, 5121–5123 (2012).

[18] D. Yan and D. G. Evans, Molecular crystalline materials with tunable luminescent properties: from polymorphs to multi-component solids, Mater. Horiz. **1**, 46–57 (2014).

[19] S. Li, Y. Lin, and D. Yan, Two-component molecular cocrystals of 9-acetylanthracene with highly tunable one-/two-photon fluorescence and aggregation induced emission, J. Mater. Chem. C **4**, 2527–2534 (2016).

[20] U. Venkataramudu, M. Annadhasan, H. Maddali, and R. Chandrasekar, Polymorphism and microcrystal shape dependent luminescence, optical waveguiding and resonator properties of coumarin-153, J. Mater. Chem. C **5**, 7262–7269 (2017).

[21] C. Botta, S. Benedini, L. Carlucci, A. Forni, D. Marinotto, A. Nitti, D. Pasini, S. Righetto, and E. Cariati, Polymorphism-dependent aggregation induced emission of a push–pull dye and its multi-stimuli responsive behavior, J. Mater. Chem. **4**, 2979–2989 (2016).

[22] R. Wei, P. Song, and A. Tong, Reversible thermochromism of aggregation-induced emission-active benzophenone azine based on polymorph-dependent excited-state intramolecular proton transfer fluorescence, J. Phys. Chem. C **117**, 3467–3474 (2013).

[23] G. Zhang, J. Lu, M. Sabat, and C. L. Fraser, Polymorphism and reversible mechanochromic luminescence for solid-state difluoroboron avobenzone, J. Am. Chem. Soc. **132**, 2160–2162 (2010).

[24] M. Tan, A. G. Shtukenberg, S. Zhu, W. Xu, E. Dooryhee, S. M. Nichols, M. D. Ward, B. Kahr, and Q. Zhu, ROY revisited, again: the eighth solved structure, Faraday Discuss. **211**, 477–491 (2018).

[25] T. Mutai, H. Satou, and K. Araki, Reproducible on–off switching of solid-state luminescence by controlling molecular packing through heat-mode interconversion, Nat. Mat. **4**, 685–687 (2005).

[26] M. Yoshida, F. Nakanishi, T. Seki, K. Sakamoto, and H. Sakurai, Two-dimensional piezochromism and orientational modulations in polysilane monolayer, Macromolecules **30**, 1860 (1997).

[27] C. Dou, L. Han, S. Zhao, H. Zhang, and Y. Wang, Multi-stimuli-responsive fluorescence switching of a donor-acceptor π-conjugated compound, J. Phys. Chem. Lett. **2**, 666–670 (2011).

[28] K. Nagura, S. Saito, H. Yusa, H. Yamawaki, H. Fujihisa, H. Sato, Y. Shimoikeda, and S. Yamaguchi, Distinct responses to mechanical grinding and hydrostatic pressure in luminescent chromism of tetrathiazolylthiophene, J. Am. Chem. Soc. **135**, 10322–10325 (2013).

[29] L. Wang, K. Wang, B. Zou, K. Ye, H. Zhang, and Y. Wang, Luminescent chromism of boron diketonate crystals: distinct responses to different stresses, Adv. Mater. **27**, 2918–2922 (2015).

[30] J. Wu, Y. Cheng, J. Lan, D. Wu, S. Qian, L. Yan, Z. He, X. Li, K. Wang, B. Zou, and J. You, Molecular engineering of mechanochromic materials by Programmed C–H arylation: making a counterpoint in the chromism trend, J. Am. Chem. Soc. **138**, 12803–12812 (2016).

[31] P. Mazumdar, D. Das, G. P. Sahoo, G. Salgado-Mora, and A. Misra, Aggregation induced emission enhancement of 4,4′-bis(diethylamino)benzophenone with an exceptionally large blue shift and its potential use as glucose sensor, Phys. Chem. Chem. Phys. **17**, 3343–3354 (2015).

[32] C. Y. K. Chan, Z. Zhao, J. W. Y. Lam, J. Liu, S. Chen, P. Lu, F. Mahtab, X. Chen, H. H. Y. Sung, H. S. Kwok, Y. Ma, I. D. Williams, K. S. Wong, and B. Z. Tang, Efficient light emitters in the solid state: synthesis, aggregation-induced emission, electroluminescence, and sensory properties of luminogens with benzene cores and multiple triarylvinyl peripherals, Adv. Funct. Mater. **22**, 378–389 (2012).

[33] S. L. Childs, G. P. Stahly, and A. Park, The salt-cocrystal continuum: the influence of crystal structure on ionization state, Mol. Pharm. **4**(3), 323–338 (2007).

[34] L. R. MacGillivray, Organic synthesis in the solid state via hydrogen-bond-driven self-assembly, J. Org. Chem. **73**, 3311–3317 (2008).

[35] G. M. Espallargas, L. Brammer, et al., Rational modification of the hierarchy of intermolecular interactions in molecular crystal structures by using tunable halogen bonds, Chem. Eur. J. **15**, 7554–7568 (2009).

[36] C. Lipinski and A. Hopkins, Navigating chemical space for biology and medicine, Nature **432**, 855–861 (2004).

[37] A. Warshel and M. Levitt, Theoretical studies of enzymic reactions: dielectric, electrostatic and steric stabilization of the carbonium ion in the reaction of lysozyme, J. Mol. Biol. **103**, 227–249 (1976).

[38] U. C. Singh and P. A. Kollman, An approach to computing electrostatic charges for molecules, J. Comp. Chem. **5**, 129–145 (1984).

[39] M. J. Field, P. A. Bash, and M. Karplus, A combined quantum mechanical and molecular mechanical potential for molecular dynamics simulations, J. Comp. Chem. **11**, 700–733 (1990).

[40] R. Salomon-Ferrer, D. A. Case, and R. C. Walker, An overview of the Amber biomolecular simulation package, WIREs Comput. Mol. Sci. **3**, 198–210 (2013).

[41] J. W. Ponder and D. A. Case, Force fields for protein simulations, Adv. Prot. Chem. **66**, 27–85 (2003).

[42] J. Wang, R. M. Wolf, J. W. Caldwell, P. A. Kollman, and D. A. Case, Development and testing of a general amber force field, J. Comp. Chem. **25**, 1157–1174 (2004).

[43] A. K. Rappe, C. J. Casewit, K. S. Coldwell, W. A. Goddard, III, and W. M. Skiff, Force fields for protein simulations, Adv. Prot. Chem. **66**, 27–85 (2003).

[44] B. R. Brooks, R. E. Bruccoleri, B. D. Olafson, D. J. States, S. Swaminathan, and M. Karplus, J. Comp. Chem. **4**, 187–217 (1983).

[45] E. Runge and E. K. U. Gross, Density-functional theory for time-dependent systems, Phys. Rev. Lett. **52**, 997–1000 (1984).

[46] M. Petersilka, U. J. Gossmann, and E. K. U. Gross, Excitation energies from time-dependent density-functional theory, Phys. Rev. Lett. **76**, 1212–1215 (1996).

[47] H. Lin and D. G. Truhlar, QM/MM: what have we learned, where are we, and where do we go from here?, Theor. Chem. Acc. **117**, 185–199 (2007).

[48] I. Antes and W. Thiel, Adjusted connection atoms for combined quantum mechanical and molecular mechanical methods, J. Phys. Chem. A **103**, 9290–9295 (1999).

[49] G. A. DiLabio, Simple one-electron quantum capping potentials for use in hybrid QM/MM studies of biological molecules, J. Chem. Phys. **116**, 9578 (2002).

[50] F. Maseras and K. Morokuma, IMOMM: A new integrated *ab initio* + molecular mechanics geometry optimization scheme of equilibrium structures and transition states, J. Comp. Chem. **16**, 1170–1179 (1995).

[51] M. Svensson, S. Humbel, R. D. J. Froese, T. Matsubara, S. Sieber, and K. Morokuma, ONIOM: a multilayered integrated MO + MM method for geometry optimizations and single point energy predictions. A test for Diels-Alder reactions and $Pt(P(t\text{-}Bu)_3)_2 + H_2$ oxidative addition, J. Phys. Chem. **100**, 19357–19363 (1996).

[52] L. W. Chuang, W. M. C. Sameera, R. Ramozzi, A. J. Page, M. Hatanaka, G. P. Petrova, T. V. Harris, X. Li, Z. Ke, F. Liu, H.-B. Li, L. Ding, and K. Morokuma, The ONIOM method and its applications, Chem. Rev. **115**, 5678–5796 (2015).

[53] H. M. Senn and W. Thiel, in *Atomisitc Approaches in Modern Biology*, edited by M. Reiher, Springer, Heidelberg, DE, 2006.

[54] H. M. Senn and W. Thiel, QM/MM studies of enzymes, Curr. Opin. Chem. Biol. **11**, 182–187 (2007).

[55] Y. Jin, E. R. Johnson, X. Hu, W. Yang, and H. Hu, Contributions of Pauli repulsions to the energetics and physical properties computed in QM/MM methods, J. Comput. Chem. **34**, 2380–2388 (2013).

[56] C. M. Isborn, B. D. Mar, B. F. E. Curchod, I. Tavernelli, and T. Martínez, The charge transfer problem in density functional theory calculations of aqueously solvated molecules, J. Phys. Chem. B **117**, 12189–12201 (2013).

[57] J. Luo, Z. Xie, J. W. Y. Lam, L. Cheng, H. Chen, C. Qiu, H. S. Kwok, X. Zhan, Y. Liu, D. Zhu, and B. Z. Tang, Aggregation-induced emission of 1-methyl-1,2,3,4,5-pentaphenylsilole, Chem. Commun. **18**, 1740–1741 (2001).

[58] J. B. Birks, editor, *Photophysics of Aromatic Molecules*, Wiley-Interscience, London, UK, 1970.

[59] F. J. M. Hoeben, P. Jonkheijm, E. W. Meijer, and A. P. H. J. Schenning, About supramolecular assemblies of π-conjugated systems, Chem. Rev. **105**, 1491–1546 (2005).

[60] J. Chen, C. C. W. Law, J. W. Y. Lam, Y. Dong, S. M. F. Lo, I. D. Williams, D. Zhu, and B. Z. Tang, Synthesis, light emission, nanoaggregation, and restricted intramolecular rotation of 1,1-substituted 2,3,4,5-tetraphenylsiloles, Chem. Mater. **15**, 1535–1546 (2003).

[61] N. L. C. Leung, N. Xie, W. Yuan, Y. Liu, Q. Wu, Q. Peng, Q. Miao, J. W. Y. Lam, and B. Z. Tang, Restriction of intramolecular motions: the general mechanism behind aggregation-induced emission, Chem. Eur. J. **20**, 15349–15353 (2014).

[62] M.-C. Li, M. Hayashi, and S.-H. Lin, Quantum chemistry study on internal conversion of diphenyldibenzofulvene in solid phase, J. Phys. Chem. A **115**, 14531–14538 (2011).

[63] Q. Wu, Q. Peng, Y. Niu, X. Gao, and Z. Shuai, Theoretical insights into the aggregation-induced emission by hydrogen bonding: a QM/MM study, J. Phys. Chem. A **116**, 3881–3888 (2012).

[64] Q. Wu, C. Deng, Q. Peng, Y. Niu, and Z. Shuai, Quantum chemical insights into the aggregation induced emission phenomena: a QM/MM study for pyrazine derivatives, J. Comput. Chem. **33**, 1862–1869 (2012).

[65] Q. Wu, T. Zhang, Q. Peng, D. Wang, and Z. Shuai, Aggregation induced blue-shifted emission – the molecular picture from a QM/MM study, Phys. Chem. Chem. Phys. **16**, 5545–5552 (2014).

[66] T. Zhang, Y. Jiang, Y. Niu, D. Wang, Q. Peng, and Z. Shuai, Aggregation effects on the optical emission of 1,1,2,3,4,5-hexaphenylsilole (HPS): a QM/MM study, J. Phys. Chem. A **118**, 9094–9104 (2014).

[67] F. Bu, R. Duan, Y. Xie, Y. Yi, Q. Peng, R. Hu, A. Qin, Z. Zhao, and B. Z. Tang, Unusual aggregation-induced emission of a coumarin derivative as a result of the restriction of an intramolecular twisting motion, Angew. Chem. Int. Ed. **54**, 14492–14497 (2015).

[68] B. Wang, X. Wang, W. Wang, and F. Liu, Exploring the mechanism of fluorescence quenching and aggregation-induced emission of a phenylethylene derivative by QM (CASSCF and TDDFT) and ONIOM (QM:MM) calculations, J. Phys. Chem. C **120**, 21850–21857 (2016).

[69] X.-L. Peng, S. Ruiz-Barragan, Z.-S. Li, Q.-S. Li, and L. Blancafort, Restricted access to a conical intersection to explain aggregation induced emission in dimethyl tetraphenylsilole, J. Mater. Chem. C **4**, 2802–2810 (2016).

[70] H. Naito, K. Nishino, Y. Morisaki, K. Tanaha, and Y. Chujo, Solid-state emission of the anthracene-*o*-carborane dyad from the twisted-intramolecular charge transfer in the crystalline state, Angew. Chem. Int. Ed. **56**, 254–259 (2017).

[71] D. Presti, L. Wilbram, C. Targa, F. Labat, A. Pedone, M. C. Menziani, I. Ciofini, and C. Adamo, Understanding aggregation-induced emission in molecular crystals: insights from theory, J. Phys. Chem. C **121**, 5747–5752 (2017).

[72] V. S. Padalkar and S. Seki, Excited-state intramolecular proton-transfer (ESIPT)-inspired solid state emitters, Chem. Soc. Rev. **45**, 169–202 (2016).

[73] J. Zhao, S. Ji, H. Guo, and P. Yang, Excited state intramolecular proton transfer (ESIPT): from principal photophysics to the development of new chromophores and applications in fluorescent molecular probes and luminescent materials, Phys. Chem. Chem. Phys. **14**, 8803–8817 (2012).

[74] J. E. Kwon and S. Y. Park, Advanced organic optoelectronic materials: harnessing excited-state intramolecular proton transfer (ESIPT) process, Adv. Mater. **23**, 3615–3642 (2011).

[75] D. Presti, F. Labat, A. Pedone, M. J. Frisch, H. P. Hratchian, I. Ciofini, M. C. Menziani, and C. Adamo, Computational protocol for modeling thermochromic molecular crystals: salicylidene aniline as a case study, J. Chem. Theory Comput. **10**, 5577–5585 (2014).

[76] D. Presti, F. Labat, A. Pedone, M. J. Frisch, H. P. Hratchian, I. Ciofini, M. C. Menziani, and C. Adamo, Modeling emission features of salicylidene aniline molecular crystals: a QM/QM′ approach, J. Comput. Chem. **37**, 861–870 (2016).

[77] B. Civalleri, C. M. Zicovich-Wilson, L. Valenzano, and P. Ugliengo, B3LYP augmented with an empirical dispersion term (B3LYP-D*) as applied to molecular crystals, CrystEngComm **10**, 405–410 (2008).

[78] P. V. Parandekar, H. P. Hratchian, and K. Raghavachari, Applications and assessment of QM: QM electronic embedding using generalized asymmetric Mulliken atomic charges, J. Chem. Phys. **129**, 145101 (2008).

[79] L. Wilbraham, C. Adamo, F. Labat, and I. Ciofini, Electrostatic embedding to model the impact of environment on photophysical properties of molecular crystals: a self-consistent charge adjustment procedure, J. Chem. Theory Comput. **12**, 3316–3324 (2016).

[80] C.-Y. Peng, J.-Y. Shen, Y.-T. Chen, P.-J. Wu, W.-Y. Hung, W.-P. Hu, and P.-T. Chou, Optically triggered stepwise double-proton transfer in an intramolecular proton relay: a case study of 1,8-dihydroxy-2-naphthaldehyde, J. Am. Chem. Soc. **137**, 14349–14357 (2015).

[81] M. Dommett, M. Rivera, and R. Crespo-Otero, How inter- and intramolecular processes dictate aggregation-induced emission in crystals undergoing excited-state proton transfer, J. Phys. Chem. Lett. **8**, 6148–6153 (2017).

[82] B. G. Levine, J. D. Coe, and T. J. Martínez, Optimizing conical intersections without derivative coupling vectors: application to multistate multireference second-order perturbation theory (MS-CASPT2), J. Phys. Chem. B **112**, 405–413 (2008).

[83] M. Arhangelskis, D. B. Jochym, L. Bernasconi, T. Friščić, A. J. Morris, and W. Jones, Time-dependent density-functional theory for modeling solid-state fluorescence emission of organic multicomponent crystals, J. Phys. Chem. A **122**, 7514–7521 (2018).

[84] J. Hutter, Excited state nuclear forces from the Tamm–Dancoff approximation to time-dependent density functional theory within the plane wave basis set framework, J. Chem. Phys. **118**, 3928 (2003).

[85] S. J. Clark, M. D. Segall, C. J. Pickard, P. J. Hasnip, M. J. Probert, K. Refson, and M. C. Payne, First principles methods using CASTEP, Z. Kristallogr. **220(5-6)**, 567–570 (2005).

[86] A. Baldereschi, Mean-value point in the Brillouin zone, Phys. Rev. B **7**, 5212–5215 (1973).

[87] P. K. Misra, *Physics of Condensed Matter*, chapter 1, pages 1–35, Elsevier Inc., New York, NY, USA, 2012.

[88] J. P. Perdew, K. Burke, and M. Ernzerhof, Generalized gradient approximation made simple, Phys. Rev. Lett. **77**, 3865–3868 (1996).

[89] S. Grimme, Semiempirical GGA-type density functional constructed with a long-range dispersion correction, J. Comput. Chem. **27**, 1787–1799 (2006).

[90] A. D. Becke, Density-functional thermochemistry. III. The role of exact exchange, J. Chem. Phys. **98**, 5648–5652 (1993).

[91] M. Arhangelskis, M. D. Eddleston, D. G. Reid, G. M. Day, D. Bučar, A. J. Morris, and W. Jones, Rationalization of the color properties of fluorescein in the solid state: a combined computational and experimental study, Chem. - Eur. J. **22**, 10065–10073 (2016).

[92] D.-K. Bučar, S. Filip, M. Arhangelskis, G. O. Lloyd, and W. Jones, Advantages of mechanochemical cocrystallisation in the solid-state chemistry of pigments: colour-tuned fluorescein cocrystals, CrystEngComm **15**, 6289–6291 (2013).

[93] J. R. G. Sander, D. Bučar, R. F. Henry, J. Baltrusaitis, G. G. Z. Zhang, and L. R. MacGillivray, A red zwitterionic co-crystal of acetaminophen and 2,4-pyridinedicarboxylic acid, J. Pharm. Sci. **99**, 3676–3683 (2010).

[94] For an introduction on density of states of periodic solids, see: `https://ecee.colorado.edu/~bart/book/book/chapter2/ch2_4.htm`.

[95] A. Dreuw and M. Head-Gordon, Failure of time-dependent density functional theory for long-range charge-transfer excited states: the zincbacteriochlorin-bacteriochlorin and bacteriochlorophyll-spheroidene complexes, J. Am. Chem. Soc. **126**, 4007–4016 (2004).

[96] A. Dreuw and M. Head-Gordon, Single-reference ab initio methods for the calculation of excited states of large molecules, Chem. Rev. **105**, 4009–4037 (2005).

[97] M. J. G. Peach, P. Benfield, T. Helgaker, and D. J. Tozer, Excitation energies in density functional theory: an evaluation and a diagnostic test, J. Chem. Phys. **128**, 044118 (2008).

[98] K. A. Nguyen, P. N. Day, and R. Pachter, The performance and relationship among range-separated schemes for density functional theory, J. Chem. Phys. **135**, 074109 (2011).

[99] A. D. Becke, Vertical excitation energies from the adiabatic connection, J. Chem. Phys. **145**, 194107 (2016).

[100] A. D. Becke, Singlet-triplet splittings from the virial theorem and single-particle excitation energies, J. Chem. Phys. **148**, 044112 (2018).

[101] P. Giannozzi, O. Andreussi, T. Brumme, O. Bunau, M. B. Nardelli, M. Calandra, R. Car, C. Cavazzoni, D. Ceresoli, M. Cococcioni, N. Colonna, I. Carnimeo, A. D. Corso, S. de Gironcoli, P. Delugas, R. A. DiStasio, A. Ferretti, Jr., A. Floris, G. Fratesi, G. Fugallo, R. Gebauer, U. Gerstmann, F. Giustino, T. Gorni, J. Jia, M. Kawamura, H. Ko, A. Kokalj, E. Küçükbenli, M. Lazzeri, M. Marsili, N. Marzari, F. Mauri, N. L. Nguyen, H. Nguyen, A. Otero-de-la-Roza, L. Paulatto, S. Poncé, D. Rocca, R. Sabatini, B. Santra, M. Schlipf, A. P. Seitsonen, A. Smogunov, I. Timrov, T. Thonhauser, P. Umari, N. Vast, X. Wu, and S. Baroni, Advanced capabilities for materials modelling with Quantum ESPRESSO, J. Phys.: Condens. Matter **29**, 465901 (2017).

[102] A. D. Becke and E. R. Johnson, A unified density-functional treatment of dynamical, nondynamical, and dispersion correlations, J. Chem. Phys. **127**, 124108 (2007).

[103] A. D. Becke and E. R. Johnson, Exchange-hole dipole moment and the dispersion interaction revisited, J. Chem. Phys. **127**, 154108 (2007).

[104] E. R. Johnson, in *Non-covalent Interactions in Quantum Chemistry and Physics, 1st Ed.*, edited by A. Otero-de-la-Roza and G. DiLabio, Elsevier, Amsterdam, NL, 2017.

[105] P. Hohenberg and W. Kohn, Inhomogeneous electron gas, Phys. Rev. **136**, B 864–B 871 (1964).

[106] W. Kohn and L. J. Sham, Self-consistent equations including exchange and correlation effects, Phys. Rev. **140**, A 1133–A 1138 (1965).

[107] A. D. Becke, On the large-gradient behavior of the density functional exchange energy, J. Chem. Phys. **85**, 7184–7187 (1986).

[108] A. D. Becke, Density-functional exchange-energy approximation with correct asymptotic behavior, Phys. Rev. A **38**, 3098–3100 (1988).

[109] J. P. Perdew, M. Ernzerhof, and K. Burke, Rationale for mixing exact exchange with density functional approximations, J. Chem. Phys. **105**, 9982–9985 (1996).

[110] C. J. Cramer, *Essentials of Computational Chemistry: Theories and Models*, Wiley, Chichester, UK, 2nd edition, 2004.

[111] A list of built-in basis sets for the Gaussian package be be found at `http://gaussian.com/basissets/`.

[112] A. D. Becke, Perspective: fifty years of density-functional theory in chemical physics, J. Chem. Phys. **140**, 18A301 (2014).

[113] A. D. Becke, Density functional calculations of molecular bond energies, J. Chem. Phys. **84**, 4524–4529 (1986).

[114] C. Lee, W. Yang, and R. G. Parr, Development of the Colle-Salvetti correlation-energy formula into a functional of the electron density, Phys. Rev. B **37**, 785–789 (1988).

[115] A. Zangwill and P. Soven, Density-functional approach to local-field effects in finite systems: photoabsorption in the rare gases, Phys. Rev. A **21**, 1561–1572 (1980).

[116] N. T. Maitra, F. Zhang, R. J. Cave, and K. Burke, Double excitations within time-dependent density functional theory linear response, J. Chem. Phys. **120**, 5932–5937 (2004).

[117] M. E. Casida, in *Recent Developments and Applications of Modern Density Functional Theory*, edited by J. Seminario, Elsevier, Amsterdam, NL, 1996.

[118] R. Bauernschmitt and R. Ahlrichs, Treatment of electronic excitations withinthe adiabatic approximation of time dependent density functional theory, Chem. Phys. Lett. **265**, 454–464 (1996).

[119] A. Dreuw, J. L. Weisman, and M. Head-Gordon, Long-range charge-transfer excited states in time-dependent density functional theory require non-local exchange, J. Chem. Phys. **119**, 2943–2946 (2003).

[120] T. Yanai, D. P. Tew, and N. C. Handy, A new hybrid exchange–correlation functional using the Coulomb-attenuating method (CAM-B3LYP), Chem. Phys. Lett. **393**, 51–57 (2004).

[121] D. C. Langreth and J. P. Perdew, Exchange-correlation energy of a metallic surface: wave-vector analysis, Phys. Rev. B **15**, 2884–2901 (1977).

[122] J. Harris, Adiabatic-connection approach to Kohn-Sham theory, Phys. Rev. A **29**, 1648–1659 (1984).

[123] A. Görling, Density-functional theory beyond the Hohenberg-Kohn theorem, Phys. Rev. A **59**, 3359–3374 (1999).

[124] M. R. Silva-Junior, M. Schreiber, S. P. A. Sauer, and W. Thiel, Benchmarks of electronically excited states: Basis set effects on CASPT2 results, J. Chem. Phys. **133**, 174318 (2010).

[125] I. N. Levine, *Quantum Chemistry*, Prentice-Hall, Englewood Cliffs, NJ, USA, 4th edition, 1991.

[126] J. R. Hook and H. E. Hall, *Solid State Physics*, Wiley, Hoboken, NJ, USA, 2nd edition, 1991.

[127] H. J. Monkhorst and J. D. Pack, Special points for Brillouin-zone integrations, Phys. Rev. B **13**, 5188 (1976).

[128] N. Troullier and J. L. Martins, Efficient pseudopotentials for plane-wave calculations, Phys. Rev. B **43**, 1993–2006 (1991).

[129] P. Schwerdtfeger, The pseudopotential approximation in electronic structure theory, ChemPhysChem **12**, 3143–3155 (2011).

[130] K. Hummer, A. Grüneis, and G. Kresse, Structural and electronic properties of lead chalcogenides from first principles, Phys. Rev. B **75**, 195211 (2007).

[131] J. Enkovaara, C. Rostgaard, K. W. Jacobsen, et al., Electronic structure calculations with GPAW: a real-space implementation of the projector augmented-wave method, J. Phys.: Condens. Matter **22**, 253202 (2010).

[132] P. E. Blöchl, Projector augmented-wave method, Phys. Rev. B **50**, 17953–17979 (1994).

[133] C. Rostgaard, The projector augmented-wave method, arXiv e-prints , arXiv:0910.1921 (Oct. 2009).

[134] M. Torrent, F. Jollet, F. Bottin, G. Zérah, and X. Gonze, Implementation of the projector augmented-wave method in the ABINIT code: application to the study of iron under pressure, Comput. Mater. Sci. **42**, 337–351 (2008).

[135] For an example of such an oline PAW dataset repository, see: `http://www.pseudo-dojo.org/`.

[136] For another online PAW dataset repository, see: `http://users.wfu.edu/natalie/papers/pwpaw/PAWDatasets.html`.

[137] For QuantumEspresso keywords listing and descriptions, see: https://www.quantum-espresso.org/Doc/INPUT_PW.html#idm385.

[138] A. Szabo and N. S. Ostlund, *Modern Quantum Chemistry*, chapter 3, pages 205–229, Dover Publications, Inc., Mineola, NY, USA, 1982.

[139] A. Szabo and N. S. Ostlund, *Modern Quantum Chemistry*, chapter 3, pages 111–149, Dover Publications, Inc., Mineola, NY, USA, 1982.

[140] R. M. Martin, *Electronic Structure: Basic Theory and Practical Methods*, Cambridge University Press, Cambridge, UK, 2004.

[141] W. Setyawan and S. Curtarolo, High-throughput electronic band structure calculations: challenges and tools, Comput. Mater. Sci. **49**, 299–312 (2010).

[142] J. F. Dobson, K. McLennan, B. P. Dinte, et al., Prediction of dispersion forces: is there a problem?, Aust. J. Chem. **54**, 513–527 (2001).

[143] F. O. Kannemann and A. D. Becke, van der Waals interactions in density-functional theory: intermolecular complexes, J. Chem. Theory Comput. **6**, 1081–1088 (2010).

[144] P. Jurečka, J. Šponer, J. Černý, and P. Hobza, Benchmark database of accurate (MP2 and CCSD(T) complete basis set limit) interaction energies of small model complexes, DNA base pairs, and amino acid pairs, Phys. Chem. Phys. **8**, 1985–1993 (2006).

[145] G. Bistoni, A. A. Auer, and F. Neese, Understanding the role of dispersion in frustrated Lewis pairs and classical Lewis adducts: a domain-based local pair natural orbital coupled cluster study, Chem. Eur. J. **23**, 865–873 (2017).

[146] J. Antony, S. Grimme, D. G. Liakos, and F. Neese, Protein–ligand interaction energies with dispersion corrected density functional theory and high-level wave function based methods, J. Phys. Chem. A **115**, 11210–11220 (2011).

[147] N. Marom, R. A. DiStasio, A. Tkatchenko, et al., Many-body dispersion interactions in molecular crystal polymorphism, Angew. Chem. Int. Ed. **52**, 6629–6632 (2013).

[148] D. C. Sorescu and B. M. Rice, Theoretical predictions of energetic molecular crystals at ambient and hydrostatic compression conditions using dispersion corrections to conventional density functionals (DFT-D), J. Phys. Chem. C **114**, 6734–6748 (2010).

[149] A short treatise on the perturbation theory of dispersion can be found in the notes by C.-K. Skylaris: https://www.southampton.ac.uk/assets/centresresearch/documents/compchem/perturbation_theory.pdf.

[150] A. van der Avoird, *Perturbation Theory for Intermolecular Forces: Application to Some Adsorption Models*, chapter 2, pages 13–30, Technische Hogeschool Eindhoven, Eindhoven, NL, 1968.

[151] F. L. Hirshfeld, Bonded-atom fragments for describing molecular charge densities, Theo. Chim. Acta **5**, 129–138 (1977).

[152] A. Becke and M. Roussel, Exchange holes in inhomogeneous systems: a coordinate-space model, Phys. Rev. A **39**, 3761–3767 (1989).

[153] S. Grimme, S. Ehrlich, and L. Goerigk, Effect of the damping function in dispersion corrected density functional theory, J. Comput. Chem. **32**, 1456–1465 (2011).

[154] A. Otero-de-la-Roza and E. R. Johnson, Van der Waals interactions in solids using the exchange-hole dipole moment model, J. Chem. Phys. **136**, 174109 (2012).

[155] J. F. Dobson and J. Wang, Successful test of a seamless van der Waals density functional, Phys. Rev. Lett. **82**, 2123–2126 (1999).

[156] J. Harl and G. Kresse, Cohesive energy curves for noble gas solids calculated by adiabatic connection fluctuation-dissipation theory, Phys. Rev. B **77**, 045136 (2008).

[157] S. Grimme, J. Antony, S. Ehrlich, and H. Krieg, A consistent and accurate *ab initio* parametrization of density functional dispersion correction (DFT-D) for the 94 elements H-Pu, J. Chem. Phys. **132**, 154104 (2010).

[158] J. Moellmann and S. Grimme, DFT-D3 study of some molecular crystals, J. Phys. Chem. C **118**, 7615–7621 (2014).

[159] A. Tkatchenko and M. Scheffler, Accurate molecular van der Waals interactions from ground-state electron density and free-atom reference data, Phys. Rev. Lett. **102**, 073005 (2009).

[160] A. Tkatchenko, R. A. DiStasio, Jr., R. Car, and M. Scheffler, Accurate and efficient method for many-body van der Waals interactions, Phys. Rev. Lett. **108**, 236402 (2012).

[161] L. Kronik and A. Tkatchenko, Understanding molecular crystals with dispersion-inclusive density functional theory: pairwise corrections and beyond, Acc. Chem. Res. **47**, 3208–3216 (2014).

[162] Y. Yang, B. Rice, X. Shi, J. R. Brandt, R. Correa da Costa, G. J. Hedley, D.-M. Smilgies, J. M. Frost, I. D. W. Samuel, A. Otero-de-la-Roza, E. R. Johnson, K. E. Jelfs, J. Nelson, A. J. Campbell, and M. J. Fuchter, Emergent properties of an organic semiconductor driven by its molecular chirality, ACS Nano **11**, 8329–8338 (2017).

[163] A. Otero-de-la-Roza and G. A. DiLabio, in *Noncovalent Interactions in Organic Electronic Materials*, edited by M. K. Ravva, A. Risko, and J.-L. Brédas, chapter 9, pages 277–302, Elsevier, 2017.

[164] W. Barford, N. Paiboonvorachat, and D. Yaron, Second-order dispersion interactions in π-conjugated polymers, J. Chem. Phys. **134**, 234101 (2011).

[165] C. Amovilli and F. M. Floris, Study of dispersion forces with quantum Monte Carlo: toward a continuum model for solvation, J. Phys. Chem. A **119**, 5327–5334 (2015).

[166] Y. Ikabata and H. Nakai, Extension of local response dispersion method to excited-state calculation based on time-dependent density functional theory, J. Chem. Phys. **137**, 124106 (2012).

[167] A. D. Laurent, C. Adamo, and D. Jacquemin, Dye chemistry with time-dependent density functional theory, Phys. Chem. Chem. Phys **16**, 14334–14356 (2014).

[168] S. Grimme, Accurate description of van der Waals complexes by density functional theory including empirical corrections, J. Comput. Chem. **25**, 1463–1473 (2004).

[169] A. Otero-de-la-Roza and E. R. Johnson, J. Chem. Phys. **138**, 204109 (2013).

[170] E. R. Johnson, in *Non-covalent Interactions in Quantum Chemistry and Physics: Theory and Applications*, edited by A. Otero-de-la-Roza and G. A. DiLabio, chapter 5, pages 169–194, Elsevier, 2017.

[171] A. Otero-de-la-Roza and E. R. Johnson, Many-body dispersion interactions from the exchange-hole dipole moment model, J. Chem. Phys. **138**, 054103 (2013).

[172] E. R. Johnson, Dependence of dispersion coefficients on atomic environment, J. Chem. Phys. **135**, 234109 (2011).

[173] M. S. Christian, A. Otero-de-la-Roza, and E. R. Johnson, Surface adsorption from the exchange-hole dipole moment dispersion model, J. Chem. Theory. Comput. **12**, 3305–3315 (2016).

[174] M. Mohebifar, E. R. Johnson, and C. N. Rowley, Evaluating force-field London dispersion coefficients using the exchange-hole dipole moment model, J. Chem. Theory Comput. **13**, 6146–6157 (2017).

[175] M. J. Frisch, G. W. Trucks, H. B. Schlegel, G. E. Scuseria, M. A. Robb, J. R. Cheeseman, G. Scalmani, V. Barone, B. Mennucci, G. A. Petersson, H. Nakatsuji, M. Caricato, X. Li, H. P. Hratchian, A. F. Izmaylov, J. Bloino, G. Zheng, J. L. Sonnenberg, M. Hada, M. Ehara, K. Toyota, R. Fukuda,

J. Hasegawa, M. Ishida, T. Nakajima, Y. Honda, O. Kitao, H. Nakai, T. Vreven, J. A. Montgomery, Jr., J. E. Peralta, F. Ogliaro, M. Bearpark, J. J. Heyd, E. Brothers, K. N. Kudin, V. N. Staroverov, R. Kobayashi, J. Normand, K. Raghavachari, A. Rendell, J. C. Burant, S. S. Iyengar, J. Tomasi, M. Cossi, N. Rega, J. M. Millam, M. Klene, J. E. Knox, J. B. Cross, V. Bakken, C. Adamo, J. Jaramillo, R. Gomperts, R. E. Stratmann, O. Yazyev, A. J. Austin, R. Cammi, C. Pomelli, J. W. Ochterski, R. L. Martin, K. Morokuma, V. G. Zakrzewski, G. A. Voth, P. Salvador, J. J. Dannenberg, S. Dapprich, A. D. Daniels, O. Farkas, J. B. Foresman, J. V. Ortiz, J. Cioslowski, and D. J. Fox, Gaussian 09 Revision E.01, 2009, Gaussian, Inc., Wallingford CT.

[176] M. E. Casida, in *Recent Advances in Computational Chemistry*, edited by D. P. Chong, chapter 5, pages 155–192, World Scientific, Singapore, 1995.

[177] R. E. Stratmann, G. E. Scuseria, and M. J. Frisch, An efficient implementation of time-dependent density-functional theory for the calculation of excitation energies of large molecules, J. Chem. Phys. **109**, 8218 (1998).

[178] C. Adamo and D. Jacquemin, The calculations of excited-state properties with time-dependent density functional theory, Chem. Soc. Rev. **42**, 845–856 (2013).

[179] D. J. Tozer, R. D. Amos, N. C. Handy, B. O. Roos, and L. Serrano-Andrès, Does density functional theory contribute to the understanding of excited states of unsaturated organic compounds?, Mol. Phys. **97**, 859–868 (1999).

[180] Z.-L. Cai, K. Sendt, and J. R. Reimers, Failure of density-functional theory and time-dependent density-functional theory for large extended π systems, J. Chem. Phys. **117**, 5543 (2002).

[181] D. J. Tozer, Relationship between long-range charge-transfer excitation energy error and integer discontinuity in Kohn–Sham theory, J. Chem. Phys. **119**, 12697 (2003).

[182] O. Gritsenko and E. J. Baerends, Asymptotic correction of the exchange–correlation kernel of time-dependent density functional theory for long-range charge-transfer excitations, J. Chem. Phys. **121**, 655–660 (2004).

[183] G. Sini, J. S. Sears, and J. L. Brédas, Evaluating the performance of DFT functionals in assessing the interaction energy and ground-state charge transfer of donor/acceptor complexes: tetrathiafulvalene-tetracyanoquinodimethane (TTF-TCNQ) as a model case, J. Chem. Theory Comput. **7**, 602–609 (2011).

[184] S. N. Steinmann, C. Piemontesi, A. Delacht, and C. Corminboeuf, Why are the interaction energies of charge-transfer complexes challenging for DFT?, J. Chem. Theory Comput. **8**, 1629–1640 (2012).

[185] E. Ruiz, D. R. Salahub, and A. Vela, Charge-transfer complexes: stringent tests for widely used density functionals, J. Chem. Phys. **100**, 12265–12276 (1996).

[186] A. Ruzsinszky, J. P. Perdew, G. I. Csonka, O. A. Vydrov, and G. E. Scuseria, Spurious fractional charge on dissociated atoms: pervasive and resilient self-interaction error of common density functionals, J. Chem. Phys. **125**, 194112 (2006).

[187] A. J. Cohen, P. Mori-Sánchez, and W. Yang, Insights into current limitations of density functional theory, Science **321**, 792–794 (2008).

[188] M.-C. Kim, E. Sim, and K. Burke, Understanding and reducing errors in density functional calculations, Phys. Rev. Lett. **111**, 073003 (2013).

[189] E. R. Johnson, A. Otero de la Roza, and S. G. Dale, Extreme density-driven delocalization error for a model solvated-electron system, J. Chem. Phys. **139**, 184116 (2013).

[190] H. Iikura, T. Tsuneda, T. Yanai, and K. Hirao, A long-range correction scheme for generalized-gradient-approximation exchange functionals, J. Chem. Phys. **115**, 3540–3544 (2001).

[191] E. I. Sánchez-Flores, R. Chávez-Calvillo, T. A. Keith, G. Cuevas, T. Rocha-Rinza, and F. Cortés-Guzmán, Properties of atoms in electronically excited molecules within the formalism of TDDFT, J. Comp. Chem. **35**, 820–828 (2014).

[192] M. E. Casida and T. A. Wesołowski, Generalization of the Kohn–Sham equations with constrained electron density formalism and its time-dependent response theory formulation, Int. J. Quantum Chem. **96**, 577–588 (2004).

[193] A. D. Becke and E. R. Johnson, A density-functional model of the dispersion interaction, J. Chem. Phys. **123**, 154101 (2005).

[194] The postg program is available from http://schooner.chem.dal.ca.

[195] T. Han, Y. Hong, N. Xie, S. Chen, N. Zhao, E. Zhao, J. W. Y. Lam, H. H. Y. Sung, Y. Dong, B. Tong, and B. Z. Tang, Defect-sensitive crystals based on diaminomaleonitrile-functionalized Schiff base with aggregation-enhanced emission, J. Mater. Chem. C **1**, 7314–7320 (2013).

[196] C. R. Groom, I. J. Bruno, M. P. Lightfoot, and S. C. Ward, The Cambridge Structural Database, Acta Cryst. **B72**, 171–179 (2016).

[197] A. Otero-de-la-Roza, E. R. Johnson, and V. Luaña, Critic2: A program for real-space analysis of quantum chemical interactions in solids, Comput. Phys. Commun. **185**, 1007–1018 (2014).

[198] K. A. Nguyen, R. R. Pachter, and P. N. Day, Density functional theory based generalized effective fragment potential method, J. Chem. Phys. **140**, 244101 (2014).

[199] A. D. Laurent and D. Jacquemin, TD-DFT benchmarks: a review, Int. J. Quantum Chem. **113**, 2019–2039 (2013).

[200] T. Koerzdoerfer, J. S. Sears, C. Sutton, and J. L. Bredas, Long-range corrected hybrid functionals for π-conjugated systems: dependence of the range-separation parameter on conjugation length, J. Chem. Phys. **135**, 204107 (2011).

[201] S. R. Whittleton, X. A. S. Vazquez, C. M. Isborn, and E. R. Johnson, Density-functional errors in ionization potential with increasing system size, J. Chem. Phys. **142**(18), 184106 (2015).

[202] K. Garrett, X. A. Sosa Vazquez, S. B. Egri, J. Wilmer, L. E. Johnson, B. H. Robinson, and C. M. Isborn, Optimum exchange for calculation of excitation energies and hyperpolarizabilities of organic electro-optic chromophores, J. Chem. Theory Comput **10**, 3821–3831 (2014).

[203] N. Murata, Control of excitation transfer in photosynthesis I. Light-induced change of chlorophyll a fluoresence in *Porphyridium cruentum*, Biochim. Biophys. Acta **172**(2), 242–251 (1969).

[204] K. Palczewski, Chemistry and biology of vision, J. Biol. Chem. **287**(3), 1612–1619 (2012).

[205] I. Navizet, Y.-J. Liu, N. Ferré, D. Roca-Sanjuán, and R. Lindh, The chemistry of bioluminescence: an analysis of chemical functionalities, ChemPhysChem **12**, 3064–3076 (2011).

[206] Y. Jiang, Z. Da, F. Qiu, Y. Guan, and G. Cao, Fabrication of chromophore molecule-linked azo polymer as waveguide material of polymeric thermo-optic digital optical switch, J. Nonlinear Opt. Phys. Mater. **26**(3), 1750032 (2017).

[207] M. E. Casida, Time-dependent density-functional theory for molecules and molecular solids, J. Mol. Struct. (Theochem) **914**, 3–18 (2009).

[208] L. Kronik, T. Stein, S. Refaely-Abramson, and R. Baer, Excitation gaps of finite-sized systems from optimally tuned range-separated hybrid functionals, J. Chem. Theory Comput. **8**, 1515–1531 (2012).

[209] D. Hait, T. Zhu, D. P. McMahon, and T. Van Voorhis, Prediction of excited-state energies and singlet–triplet gaps of charge-transfer states using a restricted open-shell Kohn–Sham approach, J. Chem. Theory Comput. **12**, 3353–3359 (2016).

[210] N. Ferré, M. Filatov, and M. Huix-Rotllant, editors, *Density-Functional Methods for Excited States*, volume 368, Springer International Publishing, Cham, Switzerland, 2016.

[211] I. N. Levine, Pearson Education, Inc., Upper Saddle River, NJ, USA, 2014.

[212] S. Grimme and M. Parac, Substantial errors from time-dependent density functional theory for the calculation of excited states of large π systems, ChemPhysChem **4**, 292–295 (2003).

[213] T. Stein, L. Kronik, and R. Baer, Reliable prediction of charge transfer excitations in molecular complexes using time-dependent density functional theory, J. Am. Chem. Soc. **131**, 2818–2820 (2009).

[214] I. Hanazaki, Vapor-phase electron donor-acceptor complexes of tetracyanoethylene and of sulfur dioxide, J. Phys. Chem. **76**(14), 1982–1989 (1972).

[215] H. Sun and J. Autschbach, Influence of the delocalization error and applicability of optimal functional tuning in density functional calculations of nonlinear optical properties of organic donor-acceptor chromophores, ChemPhysChem **14**, 2450–2461 (2013).

[216] M. Barry, II, H. Sun, N. Govind, K. Kowalski, and J. Autschbach, Charge-transfer versus charge-transfer-like excitations revisited, J. Chem. Theory Comput. **11**, 3305–3320 (2015).

[217] J. B. Foresman, M. Head-Gordon, J. A. Pople, and M. J. Frisch, Toward a systematic molecular orbital theory for excited states, J. Phys. Chem. **96**, 135–149 (1992).

[218] A. D. Becke and R. M. Dickson, Numerical solution of Poisson's equation in polyatomic molecules, J. Chem. Phys. **89**, 2993–2997 (1988).

[219] A. D. Becke, Communication: optical gap in polyacetylene from a simple quantum chemistry exciton model, J. Chem. Phys. **149**, 081102 (2018).

[220] S. G. Dale and E. R. Johnson, The explicit examination of the magnetic states of electrides, Phys. Chem. Chem. Phys. **18**, 27326–27335 (2016).

[221] A. Otero-de-la-Roza, M. A. Blanco, A. M. Pendás, and V. Luaña, Critic: a new program for the topological analysis of solid-state electron densities, Comput. Phys. Commun. **180**, 157–166 (2009).

[222] R. W. F. Bader, M. E. Stephens, and R. A. Gangi, Theoretical studies of the chemistry of singlet and triplet species. 11. Cycloaddition reaction, Can. J. Chem. **55**, 2755–2772 (1977).

[223] S. Horn, F. Plasser, T. Müller, F. Libisch, J. Burgdörfer, and H. Lischka, A comparison of singlet and triplet states for one- and two-dimensional graphene nanoribbons using multireference theory, Theor Chem Acc **133**, 1511 (2014).

[224] T. Chen, L. Zheng, J. Yuan, Z. An, R. Chen, Y. Tao, H. Li, X. Xie, and W. Huang, Understanding the control of singlet-triplet splitting for organic exciton manipulating: a combined theoretical and experimental approach, Sci. Rep. **5**, 10923 (2015).

[225] S. Gražulis, A. Dasškevič, A. Merkys, D. Chateigner, L. Lutterotti, M. Quirós, N. R. Serebryanaya, P. Moeck, R. T. Downs, and A. LeBail, Crystallography Open Database (COD): an open-access collection of crystal structures and platform for world-wide collaboration, Nucleic Acids Res. **40**, D420–D427 (2012).

[226] F. H. Allen, The Cambridge Structural Database: a quarter of a million crystal structures and rising, Acta Cryst. B **58**, 380–388 (2002), Crystal structures can be obtained free of charge via `http://www.ccdc.cam.ac.uk/data_request/cif`.

[227] T. H. Dunning, Jr., Gaussian basis sets for use in correlated molecular calculations. I. The atoms boron through neon and hydrogen, J. Chem. Phys. **90**, 1007–1023 (1989).

[228] W. Humphrey, A. Dalke, and K. Schulten, VMD: visual molecular dynamics, J. Molec. Graphics **14**, 33–38 (1996).

[229] E. R. Johnson, M. Salamone, M. Bietti, and G. A. DiLabio, Modeling noncovalent radical-molecule interactions using conventional density-functional theory: beware erroneous charge transfer, J. Phys. Chem. A **117**, 947–952 (2013).

[230] Y. Kim, S. Song, E. Sim, and K. Burke, Halogen and chalcogen binding dominated by density-driven errors, J. Phys. Chem. Lett. **10**, 295–301 (2019).

[231] Y. Sagara and T. Kato, Mechanically induced luminescence changes in molecular assemblies, Nature Chemistry **1**, 605–610 (2009).

[232] Z. Ning, Z. Chen, Q. Zhang, Y. Yan, S. Qian, Y. Cao, and H. Tian, Aggregation-Induced Emission (AIE)-active Starburst triarylamine fluorophores as potential non-doped red emitters for organic light-emitting diodes and Cl_2 gas chemodosimeter, Adv. Funct. Mater. **17**, 3799–3807 (2007).

[233] Y. Sagara, S. Yamane, M. Mitani, C. Weder, and T. Kato, Mechanoresponsive luminescent molecular assemblies: an emerging class of materials, Adv. Mater. **28**, 1073–1095 (2016).

[234] Z. Chi, X. Zhang, B. Xu, X. Zhou, C. Ma, Y. Zhang, S. Liu, and J. Xu, Recent advances in organic mechanofluorochromic materials, Chem. Soc. Rev. **41**, 3878–3896 (2012).

[235] S. Hirata and T. Watanabe, Reversible thermoresponsive recording of fluorescent images (TRF), Adv. Mater. **18**, 2725–2729 (2006).

[236] Y. Ooyama, T. Okamoto, T. Yamaguchi, T. Suzuki, A. Hayashi, and K. Yoshida, Heterocyclic quinol-type fluorophores: synthesis, X-ray crystal structures, and solid-state photophysical properties of novel 5-hydroxy-5-substituent-benzo[*b*]naphtho[1,2-*d*]furan-6-one and 3-hydroxy-3-substituent-benzo[*kl*]xanthen-2-one derivatives, Chem. Eur. J. **12**, 7827–7838 (2006).

[237] W. C. H. Choy, W. K. Chan, and Y. Yuan, Recent advances in transition metal complexes and light-management engineering in organic optoelectronic devices, Adv. Mater. **26**, 5368–5399 (2014).

[238] M. Sase, S. Yamaguchi, Y. Sagara, I. Yoshikawa, T. Mutai, and K. Araki, Piezochromic luminescence of amide and ester derivatives of tetraphenylpyrene—role of amide hydrogen bonds in sensitive piezochromic response, J. Mater. Chem. **21**, 8347–8354 (2011).

[239] Y. Dong, J. Zhang, X. Tan, L. Wang, J. Chen, B. Li, L. Ye, B. Xu, B. Zou, and W. Tian, Multi-stimuli responsive fluorescence switching: the reversible piezochromism and protonation effect of a divinylanthracene derivative, J. Mater. Chem. C **1**, 7554–7559 (2013).

[240] C. Feng, K. Wang, Y. Xu, L. Liu, B. Zou, and P. Lu, Unique piezochromic fluorescence behavior of organic crystal of carbazole-substituted CNDSB, Chem. Commun. **52**, 3836–3839 (2016).

[241] E. L. Harty, A. R. Ha, M. R. Warren, A. L. Thompson, D. R. Allan, A. L. Goodwin, and N. P. Funnell, Reversible piezochromism in a molecular wine-rack, Chem. Commun. **51**, 10608–10611 (2015).

[242] Q. Qi, J. Qian, X. Tan, J. Zhang, L. Wang, B. Xu, B. Zou, and W. Tian, Remarkable turn-on and color-tuned piezochromic luminescence: mechanically switching intramolecular charge transfer in molecular crystals, Adv. Funct. Mater. **25**, 4005–4010 (2015).

[243] Y. Liu, Q. Zeng, B. Zou, Y. Liu, B. Xu, and W. Tian, Piezochromic luminescence of donor-acceptor cocrystals: distinct responses to anisotropic grinding and isotropic compression, Angew. Chem. Int. Ed. **57**, 15670–15674 (2018).

[244] T. Zhang, W. Shi, D. Wang, S. Zhuo, Q. Peng, and Z. Shuai, Pressure-induced emission enhancement in hexaphenylsilole: a computational study, J. Mater. Chem. C **7**, 1388–1398 (2019).

[245] X. Feng, A. D. Becke, and E. R. Johnson, Communication: Becke's virial exciton model gives accurate charge-transfer excitation energies, J. Chem. Phys. **149**, 231101 (2018).

[246] X. Feng, A. Otero-de-la-Roza, and E. R. Johnson, The effect of electronic excitation on London dispersion, Can. J. Chem. **96**, 730–737 (2018).

[247] A. Dal Corso, Pseudopotentials periodic table: from H to Pu, Comput. Mater. Sci. **95**, 337–350 (2014).

[248] A. D. Becke, A new mixing of Hartree–Fock and local density-functional theories, J. Chem. Phys. **98**, 1372–1377 (1993).

[249] A. Seidl, A. Görling, P. Vogl, J. Majewski, and M. Levy, Generalized Kohn-Sham schemes and the band-gap problem, Phys. Rev. B **53**, 3764–3774 (1996).

[250] P. Mori-Sánchez, A. J. Cohen, and W. Yang, Localization and delocalization errors in density functional theory and implications for band-gap prediction, Phys. Rev. Lett. **100**, 146401 (2008).

[251] S. Refaely-Abramson, R. Baer, and L. Kronik, Fundamental and excitation gaps in molecules of relevance for organic photovoltaics from an optimally tuned range-separated hybrid functional, Phys. Rev. B **84**, 075144 (2011).

[252] E. Kraisler and L. Kronik, Fundamental gaps with approximate density functionals: the derivative discontinuity revealed from ensemble considerations, J. Chem. Phys. **140**, 18A540 (2014).

[253] D.-Y. Chen, Y.-Y. Hsu, H.-C. Hsu, B.-S. Chen, Y.-T. Lee, H. Fu, M.-W. Chung, S.-H. Liu, H.-C. Chen, Y. Chi, and P.-T. Chou, Organic dyes with remarkably high absorptivity; all solid-state dye sensitized solar cell and role of fluorine substitution, Chem. Commun. **46**, 5256–5258 (2010).

[254] I. Chung, B. Lee, R. P. H. Chang, and M. G. Kanatzidis, All-solid-state dye-sensitized solar cells with high efficiency, Nature **485**, 486–489 (2012).

[255] P. Gayathri, M. Pannipara, A. G. Al-Sehemi, and S. P. Anthony, Triphenylamine-based stimuli-responsive solid state fluorescent materials, New J. Chem. **44**, 8680–8696 (2020).

[256] R. Pode, Organic light emitting diode devices: an energy efficient solid state lighting for applications, Renew. Sustain. Energy Rev. **133**, 110043 (2020).

[257] M. Shimizu, R. Kaki, Y. Takeda, T. Hiyama, N. Nagai, H. Yamagishi, and H. Furutani, 1,4-Bis(diarylamino)-2,5-bis(4-cyanophenylethenyl)benzenes: fluorophores exhibiting efficient red and near-infrared emissions in solid state, Angew. Chem. **124**, 4171–4175 (2012).

[258] V. Trannoy, A. Léaustic, S. Gadan, R. Guillot, C. Allain, G. Clavier, S. Mazerat, B. Geffroy, and P. Yu, A highly efficient solution and solid state ESIPT fluorophore and its OLED application, New J. Chem. **45**, 3014–3021 (2021).

[259] L. Yu, Polymorphism in molecular solids: an extraordinary system of red, orange, and yellow crystals, Acc. Chem. Res. **43**, 1257–1266 (2010).

[260] B. A. Nogueira, C. Castiglioni, and R. Fausto, Color polymorphism in organic crystals, Commun. Chem. **3**, 34 (2020).

[261] Y. Chen, X. Zhang, M. Wang, J. Peng, Y. Zhou, X. Huang, W. Gao, M. Liu, and H. Wu, Mechanofluorochromism, polymorphism and thermochromism of novel D–π–A piperidin-1-yl-substitued isoquinoline derivatives, J. Mater. Chem. C **7**, 12580–12587 (2019).

[262] Q. Feng, M. Wang, B. Dong, C. Xu, J. Zhao, and H. Zhang, Tuning solid-state fluorescence of pyrene derivatives via a cocrystal strategy, CrystEngComm **15**, 3629–3632 (2013).

[263] L. Sun, W. Hua, Y. Liu, G. Tian, M. Chen, M. Chen, F. Yang, S. Wang, X. Zhang, Y. Luo, and W. Hu, Thermally activated delayed fluorescence in an organic cocrystal: narrowing the singlet–triplet energy gap via charge transfer, Angew. Chem. Int. Ed. **58**, 11311–11316 (2019).

[264] X. Feng, A. D. Becke, and E. R. Johnson, Computational modeling of piezochromism in molecular crystals, J. Chem. Phys. **152**, 234106 (2020).

[265] L. Yu, Color changes caused by conformational polymorphism: optical-crystallography, single-crystal spectroscopy, and computational chemistry, J. Phys. Chem. A **106**, 544–550 (2002).

[266] O. A. Vydrov, G. E. Scuseria, and J. P. Perdew, Tests of functionals for systems with fractional electron number, J. Chem. Phys. **126**, 154109 (2007).

[267] D. Hait and M. Head-Gordon, Delocalization errors in density functional theory are essentially quadratic in fractional occupation number, J. Phys. Chem. Lett. **9**, 6280–6288 (2018).

[268] H. L. Woodcock, H. F. Schaefer, and P. R. Schreiner, Problematic energy differences between cumulenes and poly-ynes: does this point to a systematic improvement of density functional theory?, J. Phys. Chem. A **106**, 11923–11931 (2002).

[269] D. Jacquemin, A. Femenias, H. Chermette, I. Ciofini, C. Adamo, J.-M. André, and E. A. Perpète, Assessment of several hybrid DFT functionals for the evaluation of bond length alternation of increasingly long oligomers, J. Phys. Chem. A **110**, 5952–5959 (2006).

[270] T. Heaton-Burgess and W. Yang, Structural manifestation of the delocalization error of density functional approximations: C_{4N+2} rings and C_{20} bowl, cage, and ring isomers, J. Chem. Phys. **132**, 234113 (2010).

[271] M. A. White, S. Kahwaji, V. L. S. Freitas, R. Siewert, J. A. Weatherby, M. D. M. C. Ribeiro da Silva, S. P. Verevkin, E. R. Johnson, and J. W. Zwanziger, Relative thermodynamic stability of diamond and graphite, Angew. Chem. Int. Ed. **60**, 1546–1549 (2021).

[272] S. R. Whittleton, A. Otero-de-la-Roza, and E. R. Johnson, Exchange-hole dipole dispersion model for accurate energy ranking in molecular crystal structure prediction II: nonplanar molecules, J. Chem. Theory Comput. **13**, 5332–5342 (2017).

[273] C. Greenwell, J. L. McKinley, P. Zhang, Q. Zeng, G. Sun, B. Li, S. Wen, and G. J. O. Beran, Overcoming the difficulties of predicting conformational polymorph energetics in molecular crystals via correlated wavefunction methods, Chem. Sci. **11**, 2200–2214 (2020).

[274] C. Greenwell and G. J. O. Beran, Inaccurate conformational energies still hinder crystal structure prediction in flexible organic molecules, Cryst. Growth Des. **20**, 4875–2881 (2020).

[275] J. P. Perdew, Density functional theory and the band gap problem, Int. J. Quantum Chem. **28**, 497–523 (1985).

[276] L. J. Sham and M. Schlüter, Density-functional theory of the band gap, Phys. Rev. B **32**, 3883–3889 (1985).

[277] J. P. Perdew, W. Yang, K. Burke, Z. Yang, E. K. U. Gross, M. Scheffler, G. E. Scuseria, T. M. Henderson, I. Y. Zhang, A. Ruzsinszky, H. Peng, J. Sun, E. Trushin, and A. Görling, Understanding band gaps of solids in generalized Kohn–Sham theory, Proc. Nat. Acad. Sci. **114**, 2801–2806 (2017).

[278] J.-L. Bredas, Mind the gap!, Mater. Horiz. **1**, 17–19 (2014).

[279] R. F. W. Bader, A quantum-theory of molecular-structure and its applications, Chem. Rev. **91**, 893–928 (1991).

[280] P. J. Stephens, F. J. Devlin, C. F. Chabalowski, and M. J. Frisch, Ab initio calculation of vibrational absorption and circular dichroism spectra using density functional force fields, J. Phys. Chem. **98**, 11623–11627 (1994).

[281] S. M. Woodley and R. Catlow, Crystal structure prediction from first principles, Nat. Mater. **7**, 937–946 (2008).

[282] D. H. Bowskill, I. J. Sugden, S. Konstantinopoulos, C. S. Adjiman, and C. C. Pantelides, Crystal structure prediction methods for organic molecules: state of the art, Annu. Rev. Chem. Biomol. Eng. **12**, 8 (2021).

[283] P. Giannozzi and S. Baroni, *Handbook of Materials Modeling*, chapter 1, pages 195–214, Springer, New York, NY, USA, 2005.

[284] S. Baroni, S. de Gironcoli, A. Dal Corso, and P. Giannozzi, Phonons and related crystal properties from density-functional perturbation theory, Rev. Mod. Phys. **73**, 515–562 (2001).